Manipulating Light in Organic Thin-film Devices

by

Michael Slootsky

A dissertation submitted in partial fulfillment
of the requirements for the degree of
Doctor of Philosophy
(Physics)
in The University of Michigan
2014

Doctoral Committee:

Professor Stephen R. Forrest, Chair
Assistant Professor Hui Deng
Professor L. Jay Guo
Professor Çagliyan Kurdak
Associate Professor Max Shtein

To my family

ACKNOWLEDGEMENTS

The work presented in this dissertation could not have been accomplished without the mentorship and support of numerous people. Firstly, I owe a great deal to my advisor, Stephen Forrest: I sincerely could not ask for a better teacher and mentor. Throughout my time in OCM, he has challenged me to go after hard problems and has guided me with unparalleled patience and understanding. I have come away from every interaction appreciating his insight, candor and humor.

Likewise, I am grateful for the help and contribution of my collaborators. Vinod Menon and Xiaoze Liu at CUNY helped conceive and execute the hybrid polariton project. Yue Qu was an invaluable second set of hands and eyes on the sub-ITO grid project. Jaesang Lee took the OLED concentrator idea from concept to reality. I was also fortunate to share and pursue many ideas on excitons and polaritons with Yifan Zhang. Xiaoran Tong and Quinn Burlingame graciously let me distract myself by working with them on OPV. Julie Brown and Mike Hack at Universal Display provided motivation, materials and financial support for much of the OLED work.

I am also thankful to the many OCM mentors from whom I had the privilege of learning. In particular, I greatly appreciate Yiru Sun and Cindy Xu, who introduced me to nanofabrication; Sean Zhang, who got me started with COMSOL; Fei Qi, who taught me how to grow and test devices; Chris Giebink, who showed me SEM and AFM, generously shared ideas, and served as an exemplar of an organized researcher; Stéphane Kéna-Cohen, who introduced me to polaritons and motivated the anthracene work; "Johnny" Lunt, who was an endless source of fun discussions, useful advice and "heated debates;" and Jeramy Zimmerman, who was always there to share his knowledge

and listen to my problems.

Aside from being excellent researchers, so many of my OCM labmates were also truly fun people: Xiaoran, Fei, Johnny, Stéphane, Chris, Jeramy, Kyle, Brian, Mike Arnold, Yifan, Greg, Cedric, Christine, Nana, Kyusang, Jaesang, Anurag, Quinn, Xin, Xiao, Yue and Dejiu. Thank you all for creating such an enjoyable social atmosphere in our group. In that vein, I have to especially thank Eva Ruff for not only making administrative matters a breeze, but also being such a cheerful, supportive and awesome person.

Outside of the lab (it does exist!), I have been fortunate to have really great friends. Buzz, Brooke, Marq and Misha, have been a constant source of support and often much needed distraction. John and Val Schaibley, whom I was lucky to meet in Ann Arbor, have too become my closest friends. The countless hours I spent discussing life, working out and riding motorcycles with John were surely instrumental in keeping me sane. Chief among numerous others who made my grad school experience better are Lide, Seow Yuen, Nanjun, Darian, Rachel, Jason, Adam, Jill, and Ali. Of course, I must admit that some friends who have brought me the greatest joy were not even human: Zeus and Molly Schaibley, Bridger and Austin Zimmerman, and my own pup Athos with whom I sadly didn't get to spend nearly enough time.

Finally, Xiaoran has not only been my colleague in OCM (teaching me nearly everything I know about OPV), but is also my partner and best friend. Without grad school, I would not have met you, but without your presence in my life, I could have never come this far. You make me strive to be better than I imagined possible, and for that, I love you.

Above all, I am forever indebted to my family whose constant love and support made this journey possible.

Michael Slootsky

Ann Arbor, MI

September, 2014

TABLE OF CONTENTS

LIST OF TABLES

Table

LIST OF FIGURES

Figure

LIST OF ABBREVIATIONS

Acronyms

2D	two-dimensional
3D	three-dimensional
AFM	atomic force microscopy
ALD	atomic layer deposition
ARPL	angle-resolved photoluminescence
ASE	amplified spontaneous emission
bcc	body-centered cubic
BE	Bose-Einstein
BEC	Bose-Einstein condensation
CCD	charge-coupled device
CT	charge transfer
CIE	Commission Internationale de l'Éclairage
CRI	color rendering index
CMF	color matching function
CVD	chemical vapor deposition
DBR	distributed Bragg reflector
DFB	distributed feedback
EML	emissive layer
ETL	electron transport layer
EQE	external quantum efficiency

FP	Fabry-Pérot
FWHM	full-width half-maximum
FWM	Frenkel-Wannier-Mott
GLAD	glancing-angle deposition
HOMO	highest occupied molecular orbital
HTL	hole transport layer
IC	internal conversion
ISC	inter-system crossing
IQE	internal quantum efficiency
ITO	indium-tin oxide
IML	index-matching liquid
J-V	current-density–voltage
J-V-L	current-density–voltage–luminance
LCD	liquid-crystal display
LED	light-emitting diode
LIG	low-index grid
LOR	lift-off resist
LUMO	lowest unoccupied molecular orbital
MOCVD	metalorganic chemical vapor deposition
NIR	near-infrared
NP	nano-particle
OTFT	organic thin-film transistor
OLED	organic light-emitting diode
OPV	organic photovoltaic cell
OPD	organic photodetector
OSL	organic semiconductor laser
OVJP	organic vapor jet printing

OVPD	organic vapor-phase deposition
PE	power efficiency
PECVD	plasma-enhanced chemical vapor deposition
PID	proportional-integral-derivative
PL	photoluminescence
PR	photoresist
QW	quantum well
RIE	reactive ion etching
SC	simple cubic
SEM	scanning electron microscope
SP	surface plasmon
SQE	substrate quantum efficiency
TE	transverse electric
TIR	total internal reflection
TM	transverse magnetic
UV	ultraviolet
VASE	variable-angle spectroscopic ellipsometry
VTE	vacuum thermal evaporation
WM	Wannier-Mott

Chemical Names

4TBPPZn	tetra-(2,6-t-butyl)phenol-porphyrin zinc
Alq_3	tris-(8-hydroxyquinoline)aluminum
BCP	bathocuproine, or 2,9-dimethyl-4,7-diphenyl-1,10-phenanthroline
CBP	4,4'-N,N'-dicarbazole-biphenyl
DCM	4-dicyanmethylene-2-methyl-6-(p-dimethylaminostyryl)-4H-pyran
DCM2	4-(dicyanomethylene)-2-methyl-6-julolidyl-9-enyl-4H-pyran

FIr6	bis-(4',6'-difluorophenylpyridinato)tetrakis(1-pyrazolyl)borate iridium(III)
$Ir(ppy)_3$	fac-tris(2-phenylpyridine) iridium
MFMPB	5-methyl-2-furanmethanamonium lead bromide
NMP	N-Methyl-2-pyrrolidone
NPD	4,4'-bis[N-(1-naphthyl)-N-phenyl-amino]-biphenyl
NTCDA	3,4,7,8-napthalene tetracarboxylic dianhydride
PEATBP	$(C_6H_5C_2H_4NH_3)_2PbBr_4$
PEDOT:PSS	poly(3,4-ethylenedioxythiophene) Polystyrene sulfonate
PQIr	(2,4-Pentanedionato)bis[2-(2-quinolinyl)phenyl]iridium(III)
TDAF	2,7-bis[9,9-di(4-methylphenyl)-fluoren-2-yl]-9,9-di(4-methylphenyl)fluorene
TPBI	1,3,5-tris(N-phenylbenzimidazol-2-yl)benzene
TPP	tetraphenylporphyrin
ZnTPP	zinc tetraphenylporphyrin

ABSTRACT

Manipulating Light in Organic Thin-film Devices

by

Michael Slootsky

Chair: Stephen R. Forrest

Optoelectronic devices based on organic semiconductors have been an active topic of research for more than two decades. While organic photovoltaic cells (OPVs), organic semiconductor lasers (OSLs), photodetectors and other organic electronics are still working to transition from the laboratory to commercialized products, organic light-emitting diodes (OLEDs) have found wide acceptance in small and medium, high-resolution displays, with signs of near-future adoption in TV panels and large-area lighting. The fundamentally different properties of the materials and principles of device operation offer great new possibilities in terms of energy-savings, color gamut, ease and cost of manufacturing, and novel form factors.

In the first part of this thesis, we review the operation and optics of OLEDs, focusing on the problem of extracting light trapped in the high refractive index regions of the device. Since nearly 80 % of generated light is lost before exiting in the forward viewing direction, detailed understanding of the underlying effects and methods to remedy the issue are necessary. We use 3D finite-element modeling to investigate techniques to outcouple light in a typical OLED. Furthermore, we demonstrate a method of fabricating an embedded dielectric grid with an ultra-low refractive index as an effective means of

enhancing outcoupling. Lastly, we present progress in fabricating planarized scattering structures for light extraction.

The second half of this thesis deals with the physics and applications of the strong-coupling regime in organic semiconductor microcavities, where a new quasiparticle (the polariton) emerges due to the strong interaction of light and matter. We review the progress of organic polaritonic lasers and present experimental evidence of Bose-Einstein statistics underlying their principle of operation. We show that the polariton lasing threshold in anthracene can be reduced by an order of magnitude as the temperature is decreased, in contrast to the behavior of conventional organic lasers. Additionally, we exploit the strong-coupling regime to engineer a hybrid organic-inorganic excited state at room temperature. Such photon-mediated hybridization of disparate Frenkel and Wannier-Mott excited states may allow new devices with tailored optical properties.

PART I

Light extraction in organic light-emitting diodes

CHAPTER I

Introduction

Unlike traditional semiconductors (e.g. Si, GaAs) which are grown epitaxially on brittle high-purity crystalline wafers, organic materials tend to be amorphous and can be deposited on a variety of substrates offering the promise of thin, light-weight and flexible devices that could be mass-produced using inexpensive roll-to-roll manufacturing. For over two decades, this has spurred research into a great range of solid-state devices including organic light-emitting diodes (OLEDs), organic thin-film transistors (OTFTs), organic photovoltaic cells (OPVs), organic photodetectors (OPDs) and organic semiconductor lasers (OSLs).

Of these, OLEDs have achieved the greatest commercial success since their introduction in 1987 by Tang and VanSlyke [1]. As of this writing, OLEDs are prevalent in mobile displays (e.g. Samsung Galaxy series phones) and have begun to appear in high resolution television displays made by Samsung, LG and others (Fig. 1.1(a)). In contrast to liquid-crystal displays (LCDs), the dominant technology of the previous decade, an OLED display consists of self-emissive pixels (with nearly 100% internal emission efficiency [2]) requiring neither a back-light nor color filters to produce light. This can be advantageous in terms of display contrast, color gamut and energy consumption.

(a) (b)

Figure 1.1: Examples of OLED devices: (a) Curved 55” OLED TV by Samsung, (b) flexible white OLED on plastic for lighting applications by LG Chem.

Moreover, OLED displays can be made nearly as thin as the substrate (the organic films are a fraction of a micron thick), transparent and flexible (Fig. 1.1(b)).

The color of the light produced by OLEDs can be tailored via molecular engineering, allowing both saturated pure hues as well as broad-spectrum white light. The latter quality in particular makes OLEDs an attractive candidate for solid state lighting. Through molecular, device and optical design, high-quality white light OLED sources with efficiencies exceeding 100 lm/W have been demonstrated compared to only 20 lm/W and 60 lm/W for typical fluorescent bulbs and tubes, respectively (and far exceeding incandescent lights). Since lighting makes up a significant fraction of power consumption in the U.S. and the world, this fact alone makes the advantage of OLED lighting clear. However, the previously mentioned properties of OLED displays carry over to lighting as well, opening the door for large-area sources and novel form factors.

In light of this, we begin this chapter with a review of display and lighting fundamentals. We then briefly cover the basics of small-molecular semiconductors and operation of organic light emitting devices. We conclude with a brief summary of characterization

and processing techniques used in organics and nanofabrication fields.

1.1 The nature of light

When discussing light, it is helpful to first understand how we define and measure its various properties. In the following sections, we divide our discussion into radiometry - the measurement of optical power, photometry - the measurement of light as perceived by human vision, and colorimetry - the study of color perception and rendering.

1.1.1 Radiometry

The most fundamental quantum of electromagnetic radiation is the photon, a massless particle that moves with a fixed velocity in vacuum ($c = 299\,792\,458\,\mathrm{m/s}$) and whose energy is related to its wavelength, λ, or frequency, f, by $E = \frac{hc}{\lambda} = hf$, where $h = 6.63 \times 10^{-34}\,\mathrm{J\,s}$ is the Planck constant. Thus, shorter-wavelength blue light is more energetic than long-wavelength red, and a single photon with $\lambda = 550\,\mathrm{nm}$ carries roughly $3.6 \times 10^{-19}\,\mathrm{J}$ of energy, or expressed in a more convenient unit – about 2.25 eV. As we will see later, the energies of light with ultraviolet (UV), visible, and near-infrared (NIR) wavelengths (i.e. $\lambda < 400\,\mathrm{nm}$, 400–780 nm, and $> 780\,\mathrm{nm}$, respectively) correspond well to electronic transitions of many organic molecules.

Along with energy, or more precisely *radiant energy*, we define *radiant flux* – radiant energy per unit time measured in watts (also called radiant power), *fluence* – energy per unit area ($\mathrm{J/m^2}$), *radiant intensity* – power per unit solid angle (W/sr), and *irradiance* – power incident on a surface ($\mathrm{W/m^2}$). These, among others, are radiometric units which quantify absolute physical power and are useful, for example, when considering the energy delivered by sunlight to the earth's surface (an irradiance of over $1000\,\mathrm{W/m^2}$), or that of a pump laser to a target material. Humans do not, however, perceive light in terms of absolute power due to the complex sensitivity of our eyes to different wavelengths and intensities of visible light.

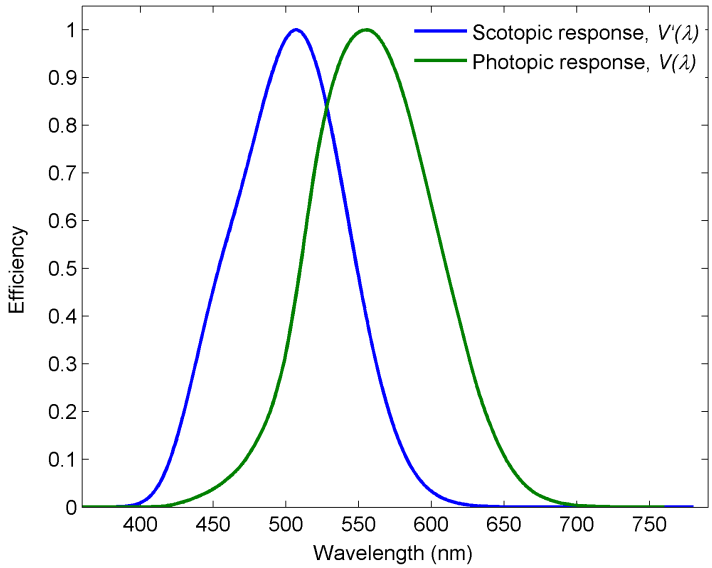

Figure 1.2: CIE 1924 photopic, $v(\lambda)$, and CIE 1951 scotopic, $v'(\lambda)$, luminosity functions normalized to their respective peak values.

1.1.2 Photometry

The human eye has two main types of photosensitive cells: the sensitive rods which handle low-light vision (scotopic response), and cones which operate in bright light (photopic response). At the beginning of the 20th century, the Commission Internationale de l'Éclairage (CIE) was established with a purpose to standardize the science of light and color perception. In 1924, CIE defined the standard photopic observer given by the *luminosity function*, $v(\lambda)$. In 1951, the standard scotopic response, $v'(\lambda)$, was introduced. The different photoreceptors' average response to light represented by $v(\lambda)$ and $v'(\lambda)$ is shown in Fig. 1.2. In both light and dark conditions, humans are most sensitive to green light, although the dark response is slightly blue-shifted. These response functions are used when converting radiometric physical quantities into photometric measures that account for human perception.

The radiant flux of a light source evaluated in terms of the photopic eye response,

for example, is defined as the *luminous flux*:

$$\Phi_{\mathrm{v}} = \phi_0 \int \Phi_\lambda v(\lambda) d\lambda. \tag{1.1}$$

Here $\phi_0 = 683\,\mathrm{lm/W}$ is the maximum spectral luminous efficacy for photopic vision, Φ_λ is the spectral power in W/nm, and Φ_{v} is in units of lumens.

By analogy to radiant intensity, we can define the *luminous intensity* as the luminous flux per unit solid angle ($I_{\mathrm{v}} = d\Phi_{\mathrm{v}}/d\Omega$) measured in candelas ($\mathrm{cd} = \mathrm{lm/sr}$). One candela is defined as the luminous intensity of a monochromatic source emitting radiation with a frequency $f = 540\,\mathrm{THz}$ ($\lambda = 555\,\mathrm{nm}$) with a radiant intensity of $1/683\,\mathrm{W\,sr^{-1}}$ which is roughly that of an average candle. (The arbitrary $1/683$ factor was chosen for historical reasons.) Lastly, the *luminance*, the psychophysical analog of radiance, of a source is an indication of how much luminous flux passes through an area, in a specified direction and falls within a given solid angle. It is measured in $\mathrm{cd/m^2}$ and defined by the derivative:

$$L = \frac{d^2\Phi_{\mathrm{v}}}{dA\, d\Omega \cos\theta} = \frac{dI_{\mathrm{v}}}{dA}\cos\theta, \tag{1.2}$$

where θ is the angle between the surface normal and the given direction, A is the surface area, and Ω is the enclosed solid angle. Luminance is a metric that is frequently used to qualify how bright a light-emitting surface will appear: a typical modern LCD screen might have $L = 300\,\mathrm{cd/m^2}$ while a TV display is closer to $1000\,\mathrm{cd/m^2}$.

An important metric for illumination sources is how much power they consume to produce a given luminous flux – the *luminous efficacy*. In the OLED field, it is frequently referred to as the *power efficiency* (PE) and is measured in lm/W. As mentioned previously, the maximum luminous efficacy for photopic vision (for monochromatic light at $\lambda = 555\,\mathrm{nm}$) is 683 lm/W, while that for scotopic vision (at $\lambda = 507\,\mathrm{nm}$) is 1700 lm/W. The typical PE values of some commercial light sources are listed in Table 1.1.

Table 1.1: Luminous efficacy (power efficiency) of commercial light sources. Adapted from Ref. [3].

Type	PE(lm/W)
Incandescent bulb	15
Halogen	20
Compact fluorescent lamp	73
Fluorescent tube	108
LED bulb	$78-119$
High-intensity discharge	$104-115$
OLED luminaire	52

1.1.3 Colorimetry

In 1801, Thomas Young first proposed that the sensation of color is due to a the mixed response of three "particles" within the retina primarily sensitive to three principal colors [4]. This idea was further developed by Helmholtz [5] using color matching experiments and forms the basis of the trichromatic color vision theory. Indeed, our ability to distinguish color arises from three different cone photoreceptor cells [6] referred to as short-, middle- and long-wavelength–sensitive (S, M and L) due to their relative spectral sensitivity (probability of absorbing a photon of a given wavelength) shown in Fig. 1.3. Although these sensitivities have not been measured directly, they have been estimated through a variety physiological and psychophysical experiments [7, 8]. It should be noted that unlike the three different cone varieties, there is only one type of rod cell in the eye which makes colors appear as shades of gray in very low light.

A consequence of our trichromatic vision is that any color light perceived by the eye can be matched using a combination of three primary colors. Although these could be chosen to match the fundamental spectral response of the cones themselves, the most common set of (imaginary) primary colors used to define the chromaticity of a light source is the one proposed by the CIE in 1931. These so-called spectral tristimulus values or color matching functions (CMFs) are shown in Fig. 1.4. The $\overline{y}(\lambda)$ is chosen to be exactly the normalized photopic response in Fig. 1.2. The composition of a given

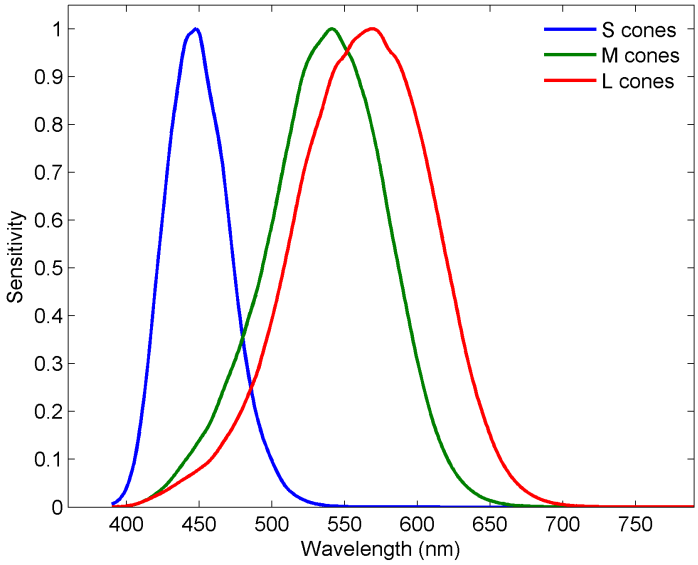

Figure 1.3: Normalized spectral sensitivity of short-, medium- and long-wavelength–sensitive cone cells (S, M, L) from Refs. [7, 8].

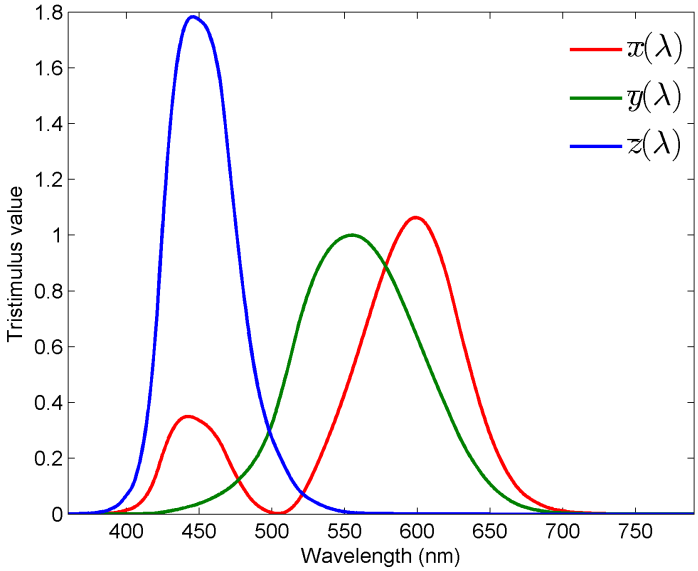

Figure 1.4: CIE 1931 tristimulus values. These color matching functions (CMFs) are used to match the spectrum of a light source, defining its color coordinates.

light source is calculated by integrating its spectral irradiance, $I(\lambda)$, against each CMF:

$$\begin{aligned} X &= \int I(\lambda)\overline{x}(\lambda)d\lambda \\ Y &= \int I(\lambda)\overline{y}(\lambda)d\lambda \\ Z &= \int I(\lambda)\overline{z}(\lambda)d\lambda, \end{aligned} \tag{1.3}$$

where $\overline{x}(\lambda)$, $\overline{y}(\lambda)$, $\overline{z}(\lambda)$ are the CMFs, and X, Y, Z are the amounts of each primary color needed to match the color of the source. This defines the CIE XYZ colorspace; other choices of CMFs result in different colorspace representations. From these, CIE defines *chromaticity coordinates* (x, y, z):

$$\begin{aligned} x &= \frac{X}{X+Y+Z} \\ y &= \frac{Y}{X+Y+Z} \\ z &= \frac{Z}{X+Y+Z}. \end{aligned} \tag{1.4}$$

Clearly, $x+y+z=1$ and only two of the values are independent, therefore it is sufficient to specify only the (x, y) coordinates to uniquely identify any color. This specification is customarily displayed on a chromaticity diagram as in Fig. 1.5. It is worthwhile to note that although most humans can see all the colors on the chromaticity diagram, neither displays nor printers can reproduce the entire range. For displays, red, green and blue (RGB) sub-pixels are used forming the vertices of a triangle within the chromaticity diagram. A display can only render hues inside this triangle which is its color gamut (CIE RGB, sRGB and Apple RGB are common examples). Similarly, printers use cyan, yellow, magenta and black (CMYK) inks to produce different colors with a generally narrower available gamut than displays. With the advent of digital processing for media, it is increasingly important to produce pure color sub-pixels and color calibrated displays in order to accurately represent images prior to printing.

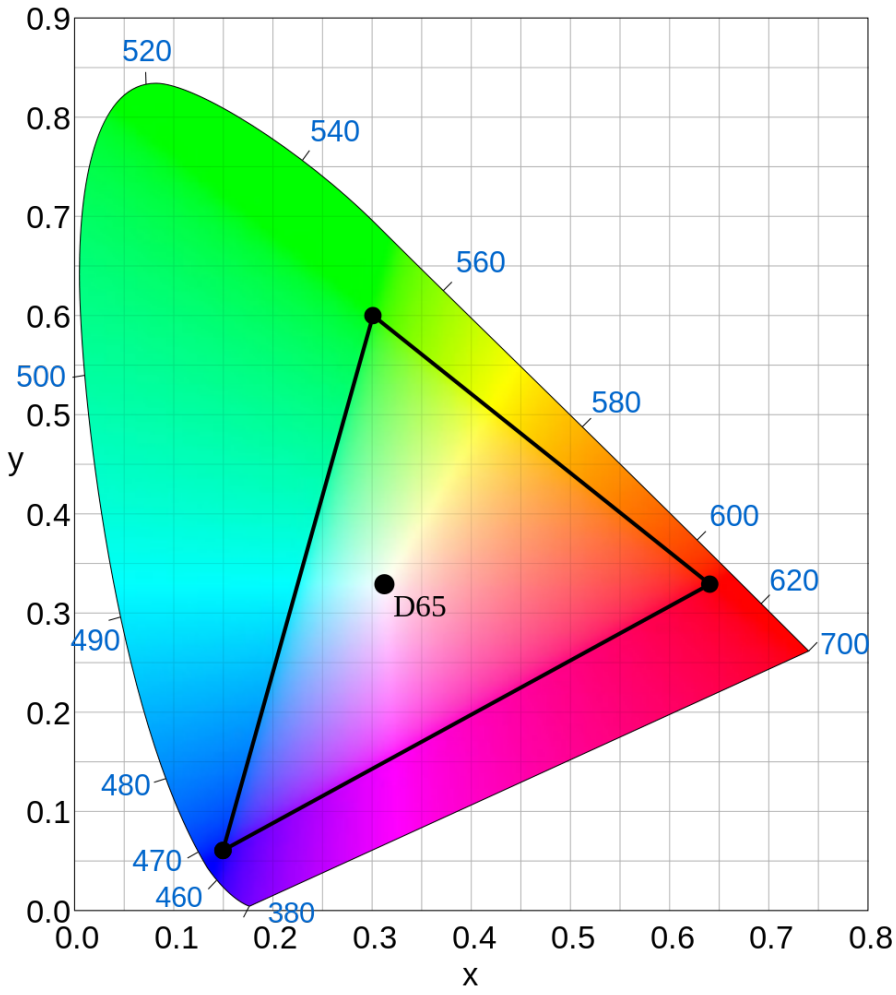

Figure 1.5: CIE 1931 chromaticity diagram showing the full range of colors perceived by humans. Pure monochromatic colors fall on the horseshoe boundary with wavelengths indicated in blue. The triangle depicts the gamut of the BT.709 HDTV color space standard. D65 is a daylight white color standard. Image from Ref. [9].

1.1.4 White light

For most of human history, illumination has been provided by thermal sources of radiation. Examples such as the sun and filaments of incandescent bulbs are well described by Planck's law for the spectral energy density of black body radiation:

$$u_\omega(T) = \frac{\hbar}{\pi^2 c^3} \frac{\omega^3}{\exp(\hbar\omega/k_B T) - 1}. \tag{1.5}$$

Here $\hbar = \frac{h}{2\pi}$ is the reduced Planck constant, $k_B = 8.62 \times 10^{-5}$ eV/K is the Boltzmann constant, and $\omega = 2\pi f$ is the angular frequency of radiation. This result follows directly from the fact that the energy of an electromagnetic mode with frequency ω_n is quantized: $E_n = s\hbar\omega_n$ where s is the integer number of photons in the mode. In thermal equillibrium, the average number of photons in a mode n is given by the Planck distribution function (a special case of the Bose-Einstein distribution):

$$\langle s \rangle = \frac{1}{\exp(\hbar\omega_n/k_B T) - 1}, \tag{1.6}$$

and the average energy is given by

$$\langle E_n \rangle = \langle s \rangle \hbar\omega_n. \tag{1.7}$$

Integrating Eq. 1.7 over all modes yields the expression in Eq. 1.5.

In order for a light source to be perceived as pleasant, not only must its own color appear white, but the spectral content must be such that hues illuminated by the source look the same as under a Planckian source. Mixing any two pure color sources which are connected by a line going through the D65 point in Fig. 1.5, for example blue (460 nm) and yellow (570 nm), will create ostensibly white light; however, colors lying away from the connecting line will appear bleak and unsaturated when placed under this light. Quantitatively this property is measured by the color rendering index (CRI), a 0–100

scale that ascertains how close the light is to a black-body spectrum by calculating the color shift of a standardized test palette for any given white light. OLEDs are particularly well suited to emulate the spectrum of thermal radiation due to their broad and tunable emission [10].

1.2 Overview of small-molecule organic semiconductors

Organic materials are most generally defined as compounds consisting mainly of carbon and hydrogen, and often incorporating other atoms. The subset of organic materials that consists of small-molecular solids with highly conjugated π-electrons is of particular interest for semiconductor devices such as OLEDs, OPVs and organic lasers. In the field of organic optoelectronics, the term "small molecule" is used to contrast materials with a well defined molecular structure and weight from polymeric materials which consist of varying-length chains of repeating monomers. Each molecule can consist of dozens of covalently bonded atoms and in fact can be, relatively speaking, quite large. Unlike well established inorganic semiconductors (e.g. Si, GaAs, InGaN) which are covalently bonded solids (bond energies on the order of eV), the molecules in organic solids are held by van der Waals bonds. Many of the interesting features of organic solids can be traced to this relatively weak (on the order of meV) intermolecular bonding. For example, organic films can be deposited without regard for matching the lattice of the substrate allowing use of cheap glass, plastic or foil substrates and low temperature deposition [11].

1.2.1 Intermolecular interaction

Broadly speaking, the van der Waals interaction is an electrostatic force between permanent or induced dipoles. In molecular solids, it arises from instantaneous random fluctuations in charge density. Thus, the momentary fluctuation on one molecule appears as a dipole to its neighbors producing a counter-polarized dipole on them. This leads to

an attraction between the two instantaneously induced dipoles – the London dispersion force, which falls off as r^{-6}, where r is the distance between the molecular dipoles. The attractive force is counteracted by a "hard shell" repulsion of the electronic orbitals due to Pauli exclusion which becomes strong at short distances. The system can be approximated by a Lennard-Jones potential:

$$V_{LJ} = 4\epsilon\left[\left(\frac{\sigma}{r}\right)^{12} - \left(\frac{\sigma}{r}\right)^{6}\right], \tag{1.8}$$

where ϵ corresponds to the strength of attraction and σ is the inter-particle distance at which the potential is zero.

Because of the weak van der Waals bonding, the sharing of electrons between molecules in organic solids is quite limited. Unlike band conduction in inorganic covalently-bonded materials, charge in organic semiconductors is highly localized on each molecule. As a result, carrier transport generally occurs by thermally assisted hopping between sites and strongly depends on the molecular configuration [12]. For the same reason, the optical properties of molecular solids largely retain the character of the individual molecules, rather than possessing collective excitations of conventional semiconductors.

1.2.2 Intramolecular bonding

Within a molecule, the bonding is quite different: atoms form strong covalent bonds through the overlap of their unpaired valence electron clouds. The close proximity of interacting atomic levels causes an energy splitting in the resulting levels of the system, creating the so-called bonding (lower-energy) and antibonding (higher-energy) molecular orbitals. Figure 1.6(a) depicts a schematic of this interaction. The number of molecular orbitals equals that of the participating atomic orbitals, with the spacing between levels within the bonding and anti-bonding manifolds decreasing as the number

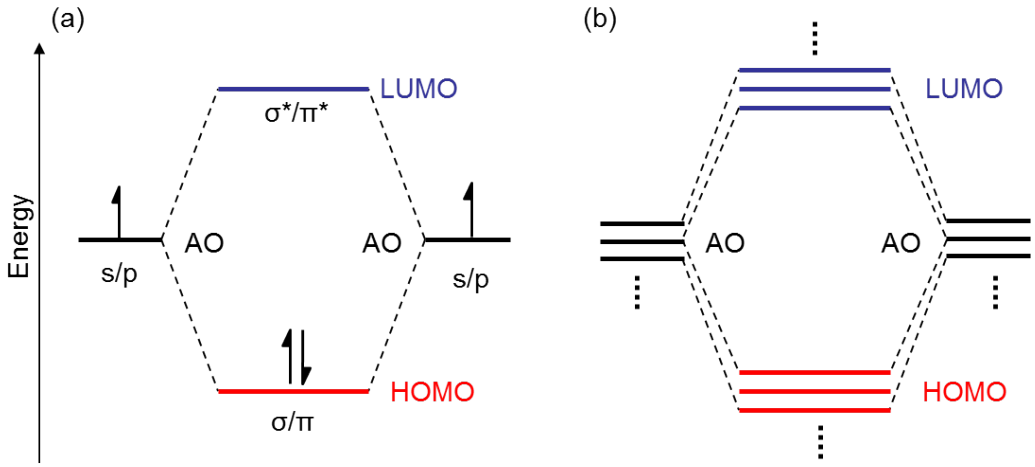

Figure 1.6: (a) Bonding (σ, π) and anti-bonding (σ*,π*) molecular orbitals are formed when atomic orbitals overlap to form a covalent bond. The unpaired valence electrons of the atoms fill the molecular orbitals according to the Aufbau and Pauli exclusion principles resulting in a HOMO and LUMO. (b) Many nearly-degenerate atomic orbitals combine within a molecule to create closely spaced molecular orbitals.

of atoms increases (Fig. 1.6(b)). In the ground state configuration of a stable closed-shell molecule, the bonding orbitals are filled with two electrons of anti-parallel spin per orbital (in accordance with the Aufbau and Pauli exclusion principles) while the anti-bonding orbitals remain empty. In inorganic semiconductors, this same process leads to formation of conduction and valence bands due to the covalent bonding of the entire lattice.

Two types of covalent bonds can form: the axisymmetric σ-bond typically consisting of a combination of *s* or *sp*-hybridized atomic orbitals, and the π-bond consisting of two overlapping out-of-plane *p* atomic orbitals. In conjugated molecules, single (σ) and double (or triple) bonds are conceptually depicted as alternating throughout the molecule, the second (and third) bonds of the latter being π-bonds. In reality, π-bonding provides a delocalized electron cloud shared by the conjugated group of atoms *within* the molecule, illustrated in Fig. 1.7 for a benzene molecule. Since the π bonding orbital is typically higher in energy than the σ, it is the HOMO of the molecule, while the anti-bonding π* is the LUMO. The energy gap between the HOMO and LUMO is typically

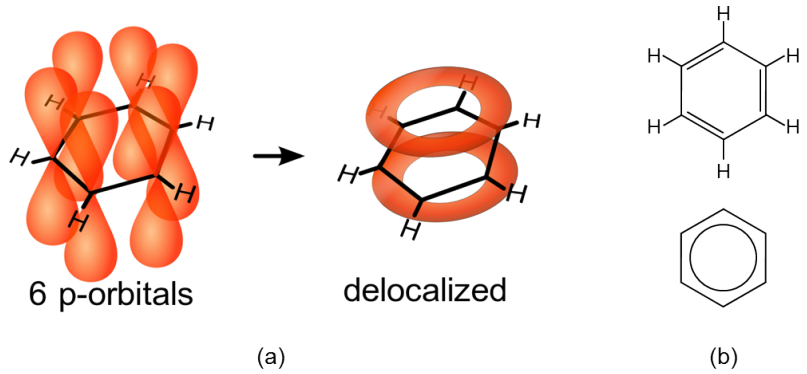

Figure 1.7: (a) In benzene, one s and two p orbitals of carbon combine to form three sp^2-hybridized planar trigonal orbitals that result in σ C-C and C-H bonds (black lines). The remaining six out-of-plane p orbitals form π-bonds producing a delocalized electron density above and below the plane of the molecule. (b) The structure can be represented showing single and double bonds (top) or the delocalized nature of the pi-bonds (bottom). Figure adapted from Ref. [13].

0.5–5 eV which is well overlapped with the visible spectrum.

1.2.3 Vibrational structure

In discussing, the (simplified) molecular orbital picture so far, we have relied on the Born-Oppenheimer approximation which allows us to treat the electrons as essentially independent from the nuclei of the system. This is a reasonable approximation since the electron motion occurs on a much faster scale due to their small mass relative to that of the atoms. However, the nuclear configuration plays a significant role in the moleculear interactions with light and so we highlight some key features here.

The potential energy of a polyatomic molecule as a function of nuclear coordinates creates a complex multidimensional potential surface [14]. A qualitative understanding can, nonetheless, be gleaned from a simplified model such as the anharmonic Morse potential of a diatomic molecule [15, 16] shown in Fig. 1.8 and given by

$$E(q) = D_e \left(1 - e^{\alpha(q-q_0)}\right)^2. \tag{1.9}$$

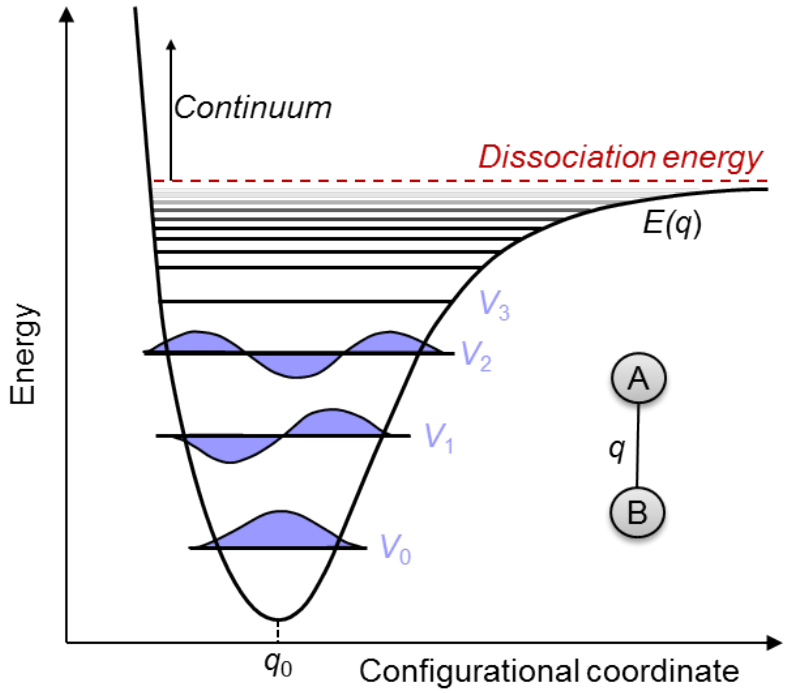

Figure 1.8: The anharmonic potential of a diatomic molecule as a function of interatomic distance. The equilibrium atomic nuclear separation is indicated by q_0. At this distance, the Coulombic repulsion of the positively charged nuclei exactly balances the bonding attraction between nuclei and electrons. The bond can be broken if enough energy is provided to escape the well. Near the minimum, the potential is approximately harmonic, resulting in a series of nearly equally-spaced vibrational energy levels, V_n. The harmonic oscillator wavefunctions are shown for the first three vibronic sublevels.

Here, D_e is the depth of the potential well relative to the dissociation energy, q is the interatomic distance, q_0 is the equilibrium separation, and α is related to the stiffness of the bond. In a polyatomic molecule, a group of nuclei can be considered in the center of mass frame, and the complex potential surface can be simplified to this two-dimensional (2D) treatment using a generalized configurational coordinate. For separations $q < q_0$, the positively charged nuclei feel a repulsive Coulomb force, while for $q > q_0$, the attraction to the negatively charged bonding electrons is a restoring force. If enough energy is provided to "escape" the well, the chemical bond will be broken and the molecule dissociates. Near the minimum, the potential is approximately harmonic, resulting in a series of quantized vibrational energy states similar to those of a harmonic oscillator as shown in Fig. 1.8. Close to the dissociation energy, the states become essentially continuous. For the potential in Eq. 1.9, the Schrödinger equation can be solved exactly to give the vibrational sublevels [16]:

$$V_n = \left(n + \frac{1}{2}\right)\hbar\omega_0 - \left(n - \frac{1}{2}\right)^2 \frac{(\hbar\omega_0)^2}{4D_e}, \tag{1.10}$$

where $\omega_0 = \alpha\sqrt{2D_e/m_N}$. Thus, the vibrational spacing depends on the strength of the bonds (α) and the mass of the nuclei (m_N). When the molecule transitions from one vibrational level to another, energy is exchanged with the environment in the form of a quantum of vibration – the phonon – or an infrared photon ($\approx 100\,\text{meV}$). Because the vibrational energy spacing is large compared to $k_B T$, only the lowest vibrational level is populated at room temperature. Rotational sublevels are even lower in energy ($\approx 1\,\text{meV}$) and do not appear as distinct features in absorption or emission spectra [12].

1.2.4 Spin

Electrons are *fermions* with spin angular momentum $s = \frac{1}{2}$. The spin projection along an arbitrary z-axis is then $s_z = m_s\hbar$ where $m_s = \pm\frac{1}{2}$ is called the spin quantum

number, and $\phi = |s, m_s\rangle$ defines a spin wavefunction. For convenience, we denote the individual electron spin states as 'up' and 'down':

$$\begin{aligned} \left|\frac{1}{2}, +\frac{1}{2}\right\rangle &\equiv |\uparrow\rangle \\ \left|\frac{1}{2}, -\frac{1}{2}\right\rangle &\equiv |\downarrow\rangle \end{aligned} \tag{1.11}$$

In this basis, there are four two-electron combinations: $|\uparrow\uparrow\rangle, |\uparrow\downarrow\rangle, |\downarrow\uparrow\rangle, |\downarrow\downarrow\rangle$; however, these are not eigenstates of the total system spin operator $\mathbf{s}^2 = \mathbf{s}_1^2 + \mathbf{s}_2^2$, where $\mathbf{s}^2 |s, m_s\rangle = s(s+1)|s, m_s\rangle$ and the subscript indicates which electron is operated on. Following the rules of angular momentum addition [17], we know a two electron state can have $s = \{0, 1\}$ and $m_s = \{0, \pm 1\} \in |m_s| \leq s$. We can construct a new set of basis states for the two-electron system that satisfies these conditions yielding an antisymmetric *singlet* state,

$$|0, 0\rangle = \frac{1}{\sqrt{2}}\big[\, |\uparrow\downarrow\rangle - |\downarrow\uparrow\rangle \,\big], \tag{1.12}$$

and three symmetric *triplet* states:

$$\begin{aligned} |1, -1\rangle &= |\downarrow\downarrow\rangle, \\ |1, 0\rangle \;\; &= \frac{1}{\sqrt{2}}\big[\, |\uparrow\downarrow\rangle + |\downarrow\uparrow\rangle \,\big], \\ |1, +1\rangle &= |\uparrow\uparrow\rangle. \end{aligned} \tag{1.13}$$

Here the terms symmetric and antisymmetric denote whether the sign of the wavefunction is switched under the exchange of the two particles. For indistinguishable fermions, the total electronic wavefunction (consisting of the spatial and spin parts: $\psi'_{1,2} = \psi_{1,2}\phi_{1,2}$) must be antisymmetric i.e. $\psi'_{1,2} = -\psi'_{2,1}$. Since an exchange of two electrons with opposite spin in the same orbital does not affect the spatial part, the ground state spin function of a closed-shell molecule must be the antisymmetric singlet in Eq. 1.12. When one of the paired electrons is promoted into the LUMO, the spatial

wavefunction $\psi_{1,2}$ can now be either symmetric or antisymmetric allowing for both singlet and triplet excited states.

If we assume the two-electron spatial wavefunction can be approximated as a product of single-electron functions with appropriate symmetry, i.e.

$$\begin{aligned}\psi_{1,2}^{singlet} &= \frac{1}{\sqrt{2}}\left(\psi_1(1)\psi_2(2)+\psi_1(2)\psi_2(1)\right)\\ \psi_{1,2}^{triplet} &= \frac{1}{\sqrt{2}}\left(\psi_1(1)\psi_2(2)-\psi_1(2)\psi_2(1)\right),\end{aligned} \tag{1.14}$$

the energy of the two states can be calculated by evaluating:

$$\begin{aligned}E_{singlet} &= \frac{e^2}{8\pi\varepsilon_0}\left\langle \psi_1(1)\psi_2(2)+\psi_1(2)\psi_2(1)\left|\frac{1}{r_{12}}\right|\psi_1(1)\psi_2(2)+\psi_1(2)\psi_2(1)\right\rangle\\ E_{triplet} &= \frac{e^2}{8\pi\varepsilon_0}\left\langle \psi_1(1)\psi_2(2)-\psi_1(2)\psi_2(1)\left|\frac{1}{r_{12}}\right|\psi_1(1)\psi_2(2)-\psi_1(2)\psi_2(1)\right\rangle.\end{aligned} \tag{1.15}$$

We can collect the resulting direct and cross terms into

$$\begin{aligned}J &= \frac{e^2}{4\pi\varepsilon_0}\left\langle \psi_1(1)\psi_2(2)\left|\frac{1}{r_{12}}\right|\psi_1(1)\psi_2(2)\right\rangle\\ &\text{and}\\ K &= \frac{e^2}{4\pi\varepsilon_0}\left\langle \psi_1(1)\psi_2(2)\left|\frac{1}{r_{12}}\right|\psi_1(2)\psi_2(1)\right\rangle,\end{aligned} \tag{1.16}$$

respectively. Here, J is the Coulomb repulsive energy and K is the exchange energy, which are both positive. Thus, Eq. 1.15 becomes:

$$\begin{aligned}E_{singlet} &= J+K\\ E_{triplet} &= J-K.\end{aligned} \tag{1.17}$$

Evidently, the triplet state is lower in energy than the singlet by twice the exchange energy. Because of this, open-shell molecules with an unpaired electron in the HOMO (e.g. O_2) tend to have a triplet ground configuration.

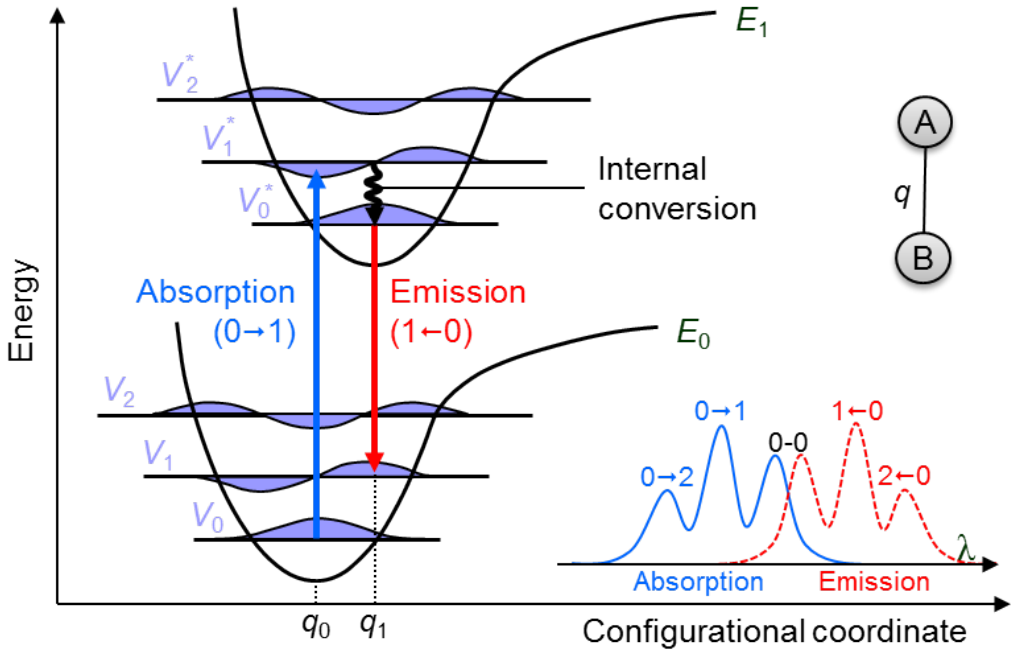

Figure 1.9: Energy diagram of the ground E_0 and first excited E_1 electronic states of a diatomic molecule. The vibrational sub-levels of both states are indicated by V_n. The equilibrium interatomic separation q increases for the excited state due to the anti-bonding nature of the LUMO. Vertical transitions between E_0 and E_1 occur by absorption and emission of light, while slower relaxation in the vibronic sub-levels within the state (internal conversion) occurs by emission of intramolecular phonons. Electronic transition probability is proportional to the overlap of the vibrational wavefunctions. Absorption occurs primarily from the lowest vibronic of the ground state, while emission occurs from the lowest vibronic of the excited state (Kasha's rule). This causes a red-shift in the emission relative to the absorption. The inset shows the resulting emission and absorption spectra.

1.2.5 Radiative transitions

A molecule can be neutrally excited by absorbing a photon of appropriate energy to promote an electron to a higher energy molecular orbital, leaving a positively charged vacancy in the HOMO called the hole. In fact, organic materials tend to have very strong absorption leading to their popularity as dyes. After a finite lifetime (τ), the excitation returns to the ground state releasing the excess energy by luminescence or heat. This process is shown schematically in Fig. 1.9 for a diatomic molecule. Both

the ground electronic state E_0 and the excited state E_1 potentials are characterized by minima at equilibrium inter-atomic distances q_0 and q_1, respectively. Due to the higher energy configuration of the anti-bonding LUMO, the excited state equilibrium separation is greater than that of the ground state ($q_1 > q_0$). In other words, in equilibrium the excited molecule is deformed due to the new electronic configuration, but the nuclear rearrangement occurs much slower than the electronic transitions which occur 'vertically.'

As discussed in §1.2.3, only the lowest vibronic is occupied at room temperature, and so absorption occurs primarily from this state to the vibronic sublevels of the excited state at a rate exceeding $10^{15}\,\mathrm{s}^{-1}$. The nuclear configuration then shifts as the molecule relaxes into the lowest vibronic of the ground state non-radiatively (internal conversion) at a slower rate of $10^{13}\,\mathrm{s}^{-1}$. Emission then occurs from V_0^* to the vibronic sublevels of the ground state, in principle, resulting in a red-shifted mirror-image of the absorption spectrum (Fig. 1.9 inset). Finally, the molecule relaxes non-radiatively to the lowest vibrational energy of the ground state.

The probability of a transition between the intial and final states can be estimated using Fermi's Golden Rule:

$$\Gamma_{fi} \simeq \frac{2\pi}{\hbar} \left| \left\langle \Psi_f \left| H' \right| \Psi_i \right\rangle \right|^2 \rho_f, \tag{1.18}$$

where Ψ are the eigenstates of the system, ρ_f is the density of final states, and H' is the perturbation that drives the transition. In the instance of absorption or emission of light, $H' = -\mathbf{d} \cdot \mathbf{E}$ where $\mathbf{d}$ is the dipole moment of the molecule and $\mathbf{E}$ is the electric field. Invoking the Born-Oppenheimer approximation, we can write the total wavefunction as the product of vibrational (nuclear), electronic spatial and electronic spin terms:

$$\Psi = \chi_v \psi_e \phi_s. \tag{1.19}$$

Inserting Eq. 1.19 into Eq. 1.18 gives:

$$\begin{aligned}\Gamma_{fi} &= \frac{2\pi}{\hbar}\left|\left\langle \chi_f \psi_f \phi_f \right| -\mathbf{d}\cdot\mathbf{E} \left| \chi_i \psi_i \phi_i \right\rangle\right|^2 \rho_f \\ &\propto E^2 \rho_f \left|\left\langle \chi_f \mid \chi_i \right\rangle\right|^2 \left|\left\langle \psi_f \left| \hat{d} \right| \psi_i \right\rangle\right|^2 \left|\left\langle \phi_f \mid \phi_i \right\rangle\right|^2 .\end{aligned} \tag{1.20}$$

The perturbation does not act on the nuclei (because their response to the electric field is too slow) or the spin (in the absence of strong spin-orbit interaction). The probability is proportional to the intensity of the electric field (E^2) and the density of final states. It is clear that if any of the terms of Eq. 1.20 are zero, the transition will not occur; this leads to several transition selection rules.

First, the $\left|\left\langle \chi_f \mid \chi_i \right\rangle\right|^2$ term, called the Franck-Condon factor, implies that the transition is more probable when the overlap integral of the vibrational wavefunctions is large, i.e. the electronic transition prefers minimal change in the positions of the nuclei. This results in transitions to the higher sublevels of the manifolds to be favored over direct 0-0 absorption/emission due to the shift in equilibrium configurational coordinate of the excited state (Fig. 1.9). The peak emission wavelength is then usually significantly shifted from the peak absorption, referred to as the Stokes shift, which is a characteristic feature of organic semiconductors.

The next term is the transition dipole moment, $d_{fi} = \left\langle \psi_f \left| \hat{d} \right| \psi_i \right\rangle$, which provides the orbital selection rule. Transitions which result in $d_{fi} = 0$ are called dipole-forbidden. We can relate the transition dipole moment to the molar absorption coefficient of a material via the oscillator strength, f, which is defined as:

$$\begin{aligned} f &= \frac{2m_e}{3e^2\hbar^2}\left|d_{fi}\right|^2 (E_f - E_i) \\ &= \frac{20\varepsilon_r \varepsilon_0 m_e c \ln 10}{e^2 N_A \pi \hbar}\int k(E)dE, \end{aligned} \tag{1.21}$$

where m_e is the electron mass, e is the electron charge, ε_r is the relative dielectric constant of the material, ε_0 is the permittivity of free space, and N_A is Avogadro's number.

Thus, the square of the transition dipole moment is directly proportional to the strength of the absorption. It can be shown [12] that this also leads to strong spontaneous and stimulated emission.

Finally, the last term of Eq. 1.20 provides the spin selection rule ensuring that the initial and final spin states must have the same parity. This term vanishes for transitions interconnecting singlet and triplet states. Since the ground state of most molecules is a singlet, emission that accompanies a transition from the singlet excited state (fluorescence) is allowed, while that from the triplet excited state (phosphorescence) is spin-forbidden. In reality, this rule is somewhat relaxed since spin-orbit coupling produces singlet-triplet mixing. Thus phosphorescence can occur in many molecules but with an extremely low rate, k_r, or equivalently very long radiative lifetime τ_r ranging from milliseconds to seconds; fluorescent lifetimes by comparison are on the order of nanoseconds. Therefore, the emission is predominantly from the singlet states. However, when a heavy atom is inserted into the molecule, the spin-orbit coupling is increased (heavy atom effect) making phosphorescence significantly more efficient. Based on this effect, the introduction of the phosphorescent OLED by Baldo et al. [18] led to a major leap in device efficiency compared to early fluorescent systems.

1.2.6 Non-radiative transitions

It should be noted that one can use Eq. 1.18 to analyze non-radiative transitions that couple electronic and vibrational motion [14], but in this case one must include terms neglected in the Born-Oppenheimer approximation and the wavefunction is no longer easily separable as in Eq. 1.19. Qualitatively, the non-radiative transition probability is reduced as the energy difference between the initial and final states is increased. The transition matrix element also includes the spin term which imparts the same spin selection rules as for radiative transitions. In general, non-radiative transitions convert electronic energy into phonons, de-exciting the molecule. Since vibrational energy of a

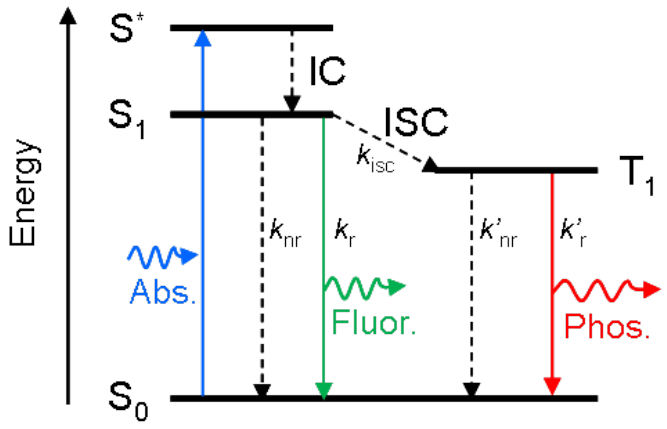

Figure 1.10: Schematic of radiative and non-radiative transitions. Absorption occurs from the ground state to a 'hot' singlet state. Fast non-radiative relaxation then occurs via internal conversion (IC) to the first excited singlet state. The molecule can be further de-excited non-radiatively (with a rate k_{nr}), radiatively by fluorescence (k_r), or the singlet may become a triplet through inter-system crossing (ISC). In molecules with strong spin-orbit coupling, the rate of ISC can dominate that of fluorescence, and emission (phosphorescence) or non-radiative relaxation proceed from the triplet state with rates k'_r and k'_{nr}, respectively.

molecule is relatively small, non-radiative electronic excitation generally does not occur [14].

Figure 1.10 illustrates the most common radiative and nonradiative processes. We already briefly saw the spin-allowed non-radiative de-excitation (internal conversion) in §1.2.5 as vibronic relaxation within an electronic state. Due to the small separation of the vibronic sub-levels, this process occurs on the order of picoseconds – much faster than fluorescence – leading to Kasha's rule. On the other hand, given the typical separation of the singlet ground and first excited states, the rate of internal conversion between them (k_{nr}) can be competitive with that of fluorescence (k_r) [14]. This leads to the definition of luminescence quantum yield:

$$\Phi = \frac{k_r}{k_r + k_{nr}}. \tag{1.22}$$

When the radiative and non-radiative processes occur at similar rates, the yield is reduced. From these considerations, it is also clear how an impurity or a defect that provides a 'mid-gap' state between the electronic ground and excited states can quench luminescence by increasing the rate of non-radiative relaxation.

The spin-disallowed non-radiative transition between singlet and triplet states is called inter-system crossing (ISC). This transition occurs in both fluorescent and phosphorescent systems and is the main source of triplet build-up under optical excitation. Under electrical excitation, the ratio of singlets and triplets formed is 1:3 [19]. In a fluorescent system, the ISC is slow and does not significantly impact the singlet emission (at low exciton densities). On the other hand, the ISC rate can be increased as spin-orbit coupling is enhanced within the molecule, mixing the triplet-singlet character of the excited states. Thus, efficient ISC in phosphorescent systems can quickly convert the singlets to triplets prior to emission and lead to luminescence entirely from triplet excitons. Given a low rate of non-radiative recombination, nearly 100 % of the triplet excitons can be converted to light [2].

1.2.7 Excitons

Due to the low intermolecular interaction, the excitation in organic materials is largely localized on a single molecule. Another view of such an excitation is a Coulombically-bound correlated electron-hole pair: the exciton. Specifically, organics most commonly have Frenkel excitons which have a high binding energy (0.1–1 eV) and small radius (<5 Å). Excitons are subject to the spin selection rules as discussed in §1.2.4. Thus optical excitation creates singlet excitons, while under electrical injection singlet and triplet excitons are formed with a 1:3 ratio [19].

In contrast, inorganic semiconductors possess Wannier-Mott (WM) excitons which have a radius that is large compared to the lattice constant. WM excitons usually only exist at low temperature or in special nanostructures such as quantum wells due to the

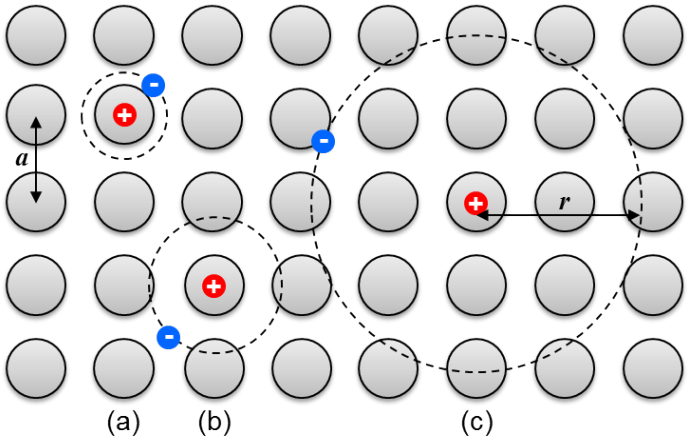

Figure 1.11: Schematic representation of the three types of excitons: (a) localized Frenkel exciton, (b) intermediate charge-transfer exciton, and (c) extended Wannier-Mott exciton. As the exciton radius, r, increases compared to the lattice constant, a, the exciton binding energy is decreased.

binding energy being below $1k_BT = 26\,\text{meV}$. A notable exception is ZnO with a WM exciton binding energy of around 60 meV in the bulk. An intermediate or charge transfer (CT) exciton, where the hole and electron reside on nearby molecules or lattice sites can also occur when the coupling between nearest neighbors is sufficient. Figure 1.11 shows a schematic of the three different types of excitons. Unlike the CT and Frenkel excitons which are relatively localized, the WM is an extended state of the lattice. Due to this, WM excitons have a relatively low saturation density above which the exciton picture starts to break down as non-linear exciton-exciton interactions eventually lead to an uncorrelated electron-hole plasma.

1.3 Principles of organic light-emitting diodes

In 1987, Tang and VanSlyke introduced the first modern multilayer OLED [1]. By using thermally evaporated thin films, this OLED could be operated at a relatively low voltage of 10 V despite the low conductivity of the organic materials – a major advance for an organic electroluminescent device. This bi-layer device used two neat layers: one for hole conduction, and the other for both electron conduction and exciton recombina-

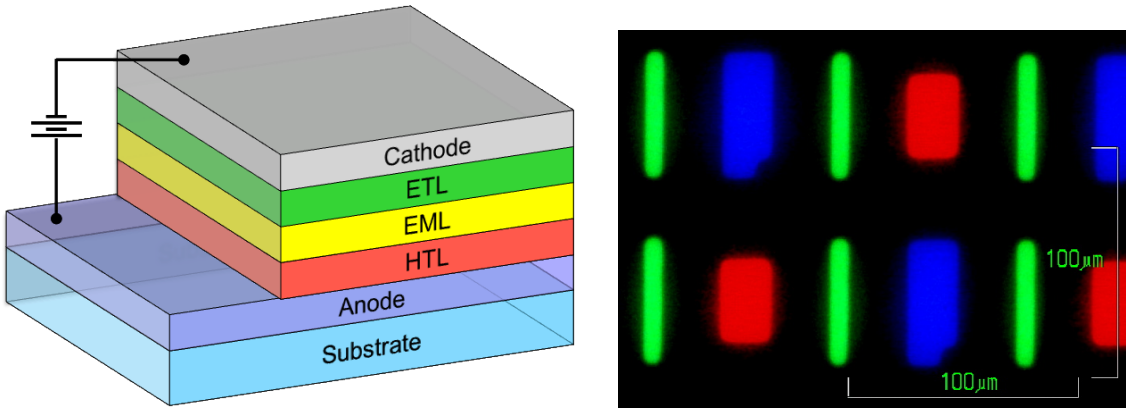

(a) (b)

Figure 1.12: (a) Structure of a three-layer OLED. Under bias, carriers injected from the electrodes are conducted through the hole- and electron-transporting layers (HTL and ETL) towards the emissive layer (EML) where excitons form. Radiative recombination produces light that is emitted through a transparent electrode. (b) Micrograph of OLED pixels in a Samsung Galaxy Nexus display (316 ppi).

tion/emission. Soon after, a tri-layer OLED was demonstrated consisting of separate hole transport layer (HTL), emissive layer (EML) and electron transport layer (ETL) [20] as in Fig. 1.13. In 1989, Tang et al. shifted the emission spectrum of their original device by doping different fluorescent emitters into a thin region of the ETL [21]. Due to spin statistics, the internal quantum efficiency (IQE) of subsequent fluorescent OLEDs remained quite low for the next decade until the introduction of phosphorescent dopants by Baldo et al. [18, 22]. As mentioned in §1.2.5, when a heavy metal atom (e.g. Pt, Ir) is inserted into the molecule, the singlet and triplet states are significantly mixed through spin-orbit coupling, increasing both the ISC and phosphorescence rates. Thus, both singlet (25 %) and triplet excitons (75 %) can contribute to the device efficiency. In fact, nearly 100 % internally efficient OLEDs have been demonstrated [2]. In the following sections, we briefly describe the basic structure, operation, optics and characterization of OLEDs.

1.3.1 Structure and operation

Modern OLEDs typically consist of at least the three organic regions indicated in Fig. 1.12(a) between two electrodes (at least one of which is transparent). The transparent electrode is usually indium-tin oxide (ITO) or a very thin metal, and, depending on its placement in the stack (bottom or top), the device is called bottom- or top-emitting, respectively. Transparent OLEDs employing two such electrodes are also possible [23, 24]. The relatively low conductivity of organic materials means that devices can be laterally defined entirely by patterning one or both conductive electrodes. Typical display pixel dimensions are 10–50 μm limited only by the patterning method (an example is shown in Fig. 1.12(b)). At the other extreme, large-area devices are only limited by the added resistive losses of the thin-film electrodes and limitations of the deposition tools. The organic layer thicknesses of a typical OLED are in the 10–100 nm range. This allows for relatively low-voltage device operation despite the low conductivity [1].

A functional diagram of a simple tri-layer OLED is presented in Fig. 1.13. To facilitate the injection of electrons into the LUMO, a low workfunction material (Φ_C) is employed for the cathode, while a high workfunction (Φ_A) anode helps extract electrons from (inject holes into) the HOMO of the adjacent organic layer. Under bias, the injected carriers travel through the HTL and ETL towards the EML. The transport layer(s) can be doped to increase conductivity and reduce device driving voltage [25]. In the EML, excitons are formed and eventually recombine producing light (or heat). For efficient operation, it is important that carriers do not "leak" through the device without forming excitons. An energy barrier on the opposite side of the EML provided either by the transport layer (as in Fig. 1.13) or by dedicated blocking layers can be used to accomplish this. Similarly, placing materials with larger exciton energies around the EML prevents exciton diffusion out of the emission zone and confines radiative recombination to the highly emissive molecules.

Most often, the EML is comprised of a host-guest system where the host provides ef-

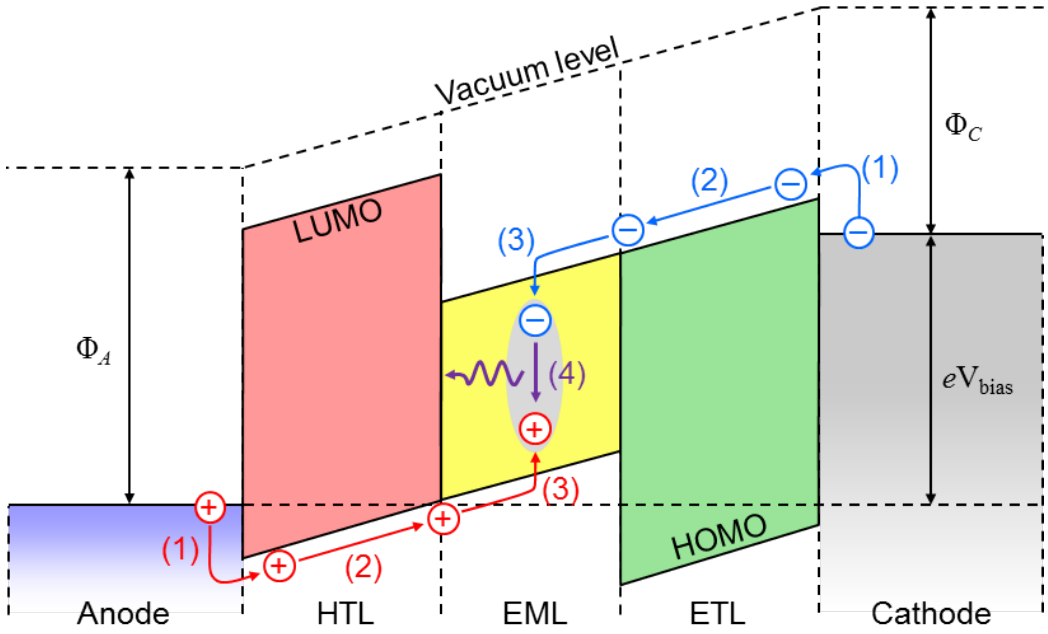

Figure 1.13: Operation of a three-layer OLED: (1) Holes and electrons are injected from the anode and cathode, respectively. The workfunction of the electrodes ($\Phi_{A/C}$) needs to be well matched with the HOMO/LUMO of the organic for efficient injection. (2) The hole- and electron-transporting layers (HTL and ETL) conduct carriers towards the emissive layer. (3) Excitons form in the emissive layer and (4) subsequently recombine to produce light. In this picture, the transport layers are also chosen such that they block the complimentary carrier from advancing beyond the EML. Note that the energy levels in organics are not perfectly sharp and are only drawn as such for clarity.

ficient charge transport while the guest is a high-quantum-yield phosphor or fluorophor with a corresponding exciton energy below that of the host. The guest doping concentration is typically a few percent by volume, sufficient to facilitate efficient energy transfer from the host, but low enough to prevent formation of aggregates which can quench emission. In fluorescent systems, the energy transfer is of the relatively long-ranged Förster type which allows for a lower dopant concentration compared to phosphorescent systems where excitons use the short-range Dexter energy transfer. Since these energy transfer processes can occur at a very high rate compared to the rate of non-radiative recombination in the host, excitons bypass quenching processes of the host in favor of the efficient guest [19].

1.3.2 Characterization of device efficiency

As a light generating device, an OLED's objective is to provide high efficiency, desired spectral and angular characteristics. In this section, we will briefly discuss experimental techniques for measuring OLED performance relevant to the subsequent chapters. A full overview of standards for OLED metrology is available in Ref. [26].

The primary metric we will rely on is *external quantum efficiency (EQE)*, defined as the ratio of photons finally emitted in the forward viewing direction to the number of injected charges. In order to measure *EQE*, one must carefully account for every charge injected and photon emitted. The former is done trivially using an ammeter to measure the current ($N_e = I_{OLED}/e$), while the latter depends on the responsivity of the photodetector, the emission spectrum of the OLED and the measurement geometry. The incremental detector responsivity is defined as the ratio of incremental current generated (I_{det}) to the incident spectral power (Φ_{OLED}) between wavelengths λ and $\lambda + d\lambda$:

$$R(\lambda) = \frac{I_{det}(\lambda)}{f\,\Phi_{OLED}(\lambda)} \tag{1.23}$$

where f is the fraction of emitted light that reaches the detector. A typical responsivity

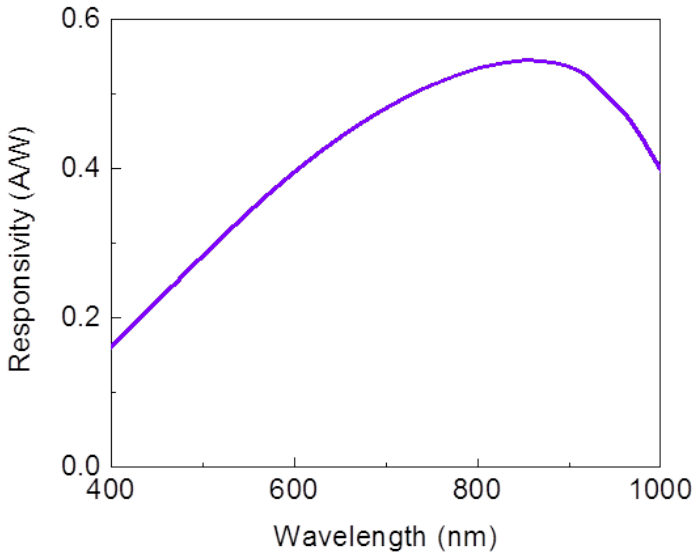

Figure 1.14: Spectral responsivity of a Si photodetector used for OLED testing.

curve for a calibrated Si detector used for measurements in this work is shown in Fig. 1.14. The number of emitted photons can then be expressed as:

$$N_p = \int \frac{\Phi_{OLED}(\lambda)}{hc/\lambda} d\lambda = \int \frac{\lambda I_{det}(\lambda)}{f hc R(\lambda)} d\lambda, \tag{1.24}$$

and the *EQE* is given by:

$$\eta_{EQE} = \frac{N_p}{N_e} = \frac{e}{f hc I_{OLED}} \int \frac{\lambda I_{det}(\lambda)}{R(\lambda)} d\lambda. \tag{1.25}$$

In practice, a Si detector is used giving a total integrated photocurrent but not the wavelength-resolved incremental photocurrent $I_{det}(\lambda)$. Therefore, spectrum-weighted average values (denoted by bars here) are used:

$$\eta_{EQE} = \frac{e\bar{\lambda} I_{det}}{f hc I_{OLED} \bar{R}}. \tag{1.26}$$

Within the device, the conversion of current to light occurs via several sequential

steps each with its own associated efficiency: (1) carriers are injected from the contacts and transported to the emissive layer while maintaining a charge balance (CB) between holes and electrons; (2) the carriers form excitons; (3) light is emitted as the excitons radiatively recombine; and (4) the produced photons escape the device. Thus the EQE can be represented as a product of four efficiencies, the first three of which can be grouped into the so-called *internal quantum efficiency (IQE)*:

$$\eta_{EQE} = \eta_{CB}\eta_{FORM}\eta_{R}\eta_{OUT} = \eta_{IQE}\eta_{OUT}. \tag{1.27}$$

Clearly, the IQE is dependent on the choice of contacts, materials and device structure, and encompasses all the electronic processes. Due to absorption within the device, a direct measurement of IQE is not generally possible, but can be derived from the measurement of EQE by assuming or modeling the outcoupling efficiency which includes all optical losses within the device as will be discussed in Chapter II. The radiative efficiency (η_R) is related to the luminescence quantum yield (Eq. 1.22), but also includes weak microcavity-induced effects [27] and other sources of non-radiative quenching e.g. exciton-exciton and exciton-charge interactions that noticeably reduce efficiency at high-current operation [28, 29].

For both display and lighting applications, it is important not only to maximize the EQE, but also to minimize the energy expended in generating the light. The standard metric, introduced in §1.1.2, is the power efficiency (PE) which relates the luminous power output of the device to the electrical power used to drive the OLED. Thus we use Eq. 1.1, the photopic response, $v(\lambda)$, shown in Fig. 1.2, and the spectrally resolved terms in Eq. 1.24 to express the PE as:

$$\eta_{PE} = \frac{\phi_0 \int v(\lambda) I_{det}(\lambda)/R(\lambda) d\lambda}{f I_{OLED} V_{OLED}}, \tag{1.28}$$

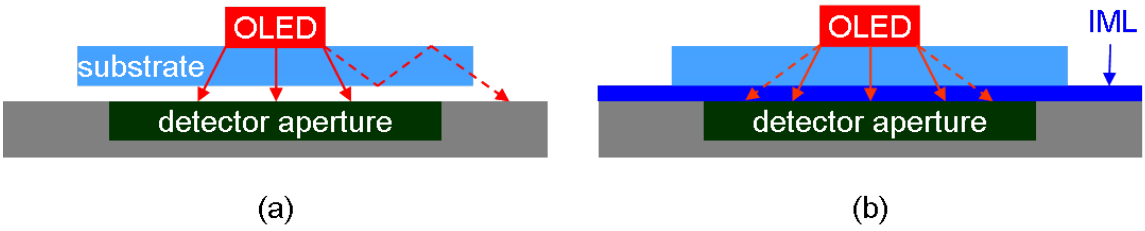

Figure 1.15: (a) A large-aperture detector placed directly in front of an OLED is used to measure light in the forward direction. Care must be taken to prevent edge-emitted light (dashed) from being detected. (b) An index-matching liquid (IML) can be used to couple nearly all substrate guided light to the detector.

or in terms of spectrum-weighted average values:

$$\eta_{PE} = \frac{\phi_0 \overline{\nu} I_{det} / \overline{R}}{f I_{OLED} V_{OLED}}. \tag{1.29}$$

It is evident that increasing EQE can concomitantly increase the PE if the I-V characteristics remain the same. Moreover, reducing the voltage necessary to drive a given current through the device (by increasing layer conductivity or removing injection barriers) will result in power savings.

The coupling factor f is present in expressions for both EQE and PE and highlights the importance of proper measurement geometry. Ideally, every useful photon generated by the device is captured by the detector, yielding $f = 1$. By using a large-aperture photodetector placed in close proximity to the device as in Fig. 1.15(a), this can be accomplished. However, care must be taken to block the significant fraction of light exiting the edge of the substrate from being detected and artificially boosting efficiency. On the other hand, when characterizing methods of improving outcoupling efficiency (η_{OUT}), it is often useful to directly measure this substrate guided light (see §2.1) by placing the device in an integrating sphere, or by applying an index-matching liquid (IML) between the substrate and the detector as in Fig. 1.15(b) and thus removing the air interface. The resulting measurements then give the maximum quantum and

power efficiencies of the combined device substrate and air modes. This can be used to gauge the percentage of light outcoupled from the substrate by external structures, or directly determine relative improvement in outcoupling of waveguided light by internal structures. In this work, we will refer to the quantum efficiency measured using the IML as the *substrate quantum efficiency* (*SQE*).

1.4 Processing methods

Fabrication of semiconductor devices generally involves deposition of material by a combination of techniques from solid, liquid and/or gas sources. Because the molecules that make up organic semiconductors tend to decompose at lower temperatures compared to their inorganic counterparts, only a subset of these deposition techniques are available for organic devices. Moreover, the methods of patterning device layers (normally accomplished with lithography and etching) are restricted for organics due to their high solubility. This section is not meant to be exhaustive, but rather give a quick primer to some of the most commonly used tools in fabricating organic devices as well as micro-scale structures, particularly ones used in subsequent chapters of this thesis. Much more in-depth detail can be found in resources such as Ref. [30].

1.4.1 Vacuum thermal evaporation

Many metals, dielectrics and small-molecule organic semiconductors readily sublime in moderate vacuum. As such, one of the most common methods of deposition of organic films is by vacuum thermal evaporation (VTE), wherein the material to be deposited is placed in a (sometimes ceramic-coated) metal source which is subsequently resistively heated by passing high-power current through it. The flux of ejected material is monitored by a quartz crystal microbalance whose resonant frequency shifts characteristically when material accumulates on the surface. Typical deposition rates are in the range of 0.1–10 Å/s in vacuum below 10^{-6} Torr. The mean free path for a particle

is inversely proportional to the pressure,

$$\lambda_{mfp} \propto \frac{T}{P}, \tag{1.30}$$

and is on the order of meters (i.e. exceeding the chamber dimensions), resulting in ballistic transport and highly directional deposition. To mitigate the unwanted effects of this directionality (e.g. shadowing), the substrate is generally rotated about its perpendicular axis during deposition. All layers of conventional OLEDs (except the transparent anode) are usually deposited entirely using such resistive sublimation.

For materials that have high sublimation temperatures (e.g. SiO_2, MgF_2, Ti, Pt, etc.), resistive source heating is impractical as the container would start to melt before the deposition material. A widely used option is to directly heat the material placed in a crucible using a high-energy beam of electrons (e-beam). This allows much higher source temperatures to be reached; however, care must be taken when depositing materials with low thermal conductivity due to the point-like heat source. In most other respects, e-beam evaporation is no different from resistive sublimation, producing highly-directional material flux and relatively high deposition rates. This directionality will play a key role in Chapter IV.

The morphology of the resultant films is usually amorphous or polycrystalline since atoms and molecules have little ability to find the lowest energy configuration as they impinge on the substrate. This may be influenced by the deposition rate, substrate temperature, ad-atom surface mobility, and underlying (templating) layers; although, the biggest effect is from the specific molecular structure's tendency to crystallize. Organic materials may slowly crystallize after deposition (usually an undesirable effect). Both organic and inorganic materials may be annealed after deposition to promote reorganization of the film toward a crystalline state.

1.4.2 Sputtering and plasma etching

Another common method of depositing material from a solid source is by sputtering. During sputtering, high-energy particles from an ionized gas bombard the surface of the target ejecting particles which subsequently travel through the plasma to reach and condense on the substrate. Typical gases used are Ar, O_2 and N_2 at pressures of 1-100 mTorr. Because sputter-ejected atoms undergo collisions with the gas, the resulting films have better coverage of any features compared to the directional flux from VTE. Metals and dielectrics can be sputter deposited with particular advantage for controlling the stoichiometry of compound materials such as TiO_2 or ITO due to the ease of adding a secondary gas to the plasma. The harsh environment of the plasma makes this method incompatible with depositing organic materials, though with some care, low energy plasmas can be used to deposit material directly onto organic films [31].

In physical plasma etching, the same general process is used to remove material by replacing the source target with the substrate to be etched and using an inert gas such as Ar or He_2. Many gases can be chosen to accelerate the etching process by additionally reacting chemically with the material to be removed, termed reactive ion etching (RIE). Specifically, an O_2 plasma is very effective at removing organic materials such as polymers and is frequently used as a cleaning step in both organic and inorganic device fabrication.

1.4.3 Gas-phase deposition

Gas-phase deposition is widely used in inorganic semiconductor fabrication primarily in the form of chemical vapor deposition (CVD), a family of processes that include metalorganic chemical vapor deposition (MOCVD), plasma-enhanced chemical vapor deposition (PECVD) and atomic layer deposition (ALD). In CVD, films are produced by a chemical reaction of source gases (precursors) on or near the surface of the substrate. Carefully controlling the gas flow rate, chamber pressure and substrate temperature

allows precise control over the stoichiometry, morphology and other properties of the resulting films. MOCVD employs organometalic molecules as precursors that are injected into the reactor and decompose ('crack') on the hot surface of the substrate leaving the heavier metal atom while the organic part remains in the gas or attached to the surface awaiting reaction with a second constituent gas. This process is widely used industrially for deposition of III-V semiconductor devices. PECVD additionally uses a confined plasma (kept away from the substrate to prevent etching as in §1.4.2) to promote the chemical reaction. ALD is a case of CVD where two precursor gases are used sequentially, each producing a self-limiting reaction at the film surface, and thus allowing monolayer precision during film deposition. Because these processes occur in an equilibrium (compared to far-from-equilibrium VTE and sputtering), the control over film properties is greatly improved, and the resulting films can be highly uniform and pinhole free.

Related techniques for depositing organic materials are the so-called organic vapor-phase deposition (OVPD) and organic vapor jet printing (OVJP). Rather than produce a film by chemical reaction of precursor gases, here, the organic is evaporated by injecting the source material into a hot-walled reactor (kept at a high enough temperature to prevent condensation on the walls) with a directed inert gas flow from the source to the cooled substrate where the film condenses. By controlling the carrier gas flow rate, chamber pressure, source and substrate temperatures, great control of the film morphology can be exercised as deposition transitions between ballistic and equilibrium transport. Extending this idea, OVJP flows the carrier gas through a narrow nozzle closely positioned to the substrate, allowing direct writing of finely resolved features without the use of shadow masks, solvents, or other pre- or post-patterning steps.

1.4.4 Solution processing

Although many solution-based deposition methods of materials exist such as liquid-phase epitaxy, ink-jet and screen-printing, as well as dip-, blade-, spray- and spin-coating, only the latter will be employed in subsequent chapters. Spin-coating is accomplished by dissolving (or suspending) the source material in a liquid, disposing the solution on the substrate, and rapidly spinning the substrate to spread and coat it with the material as the solvent evaporates. Layer thickness can be controlled by the spin speed and solution concentration. Post-annealing can be used to further dry the film or alter its morphology. This technique is frequently used for materials that cannot be evaporated without decomposing, but that readily dissolve in organic solvents or water (semiconducting polymers, photoresist, some small molecules and inorganic compounds). Due to the solvents, this places an inherent limitation on the number of layers that can be deposited.

1.5 Thesis organization

The work presented in this dissertation follows two major themes: light-extraction in OLEDs (detailed in Part I) and polaritonic phenomena in the strong-coupling regime (Part II). In Chapter II, we review the optics of bottom-emitting OLEDs, optical loss pathways and various light extraction techniques. In Chapter III, we model and optimize a low-index grid (LIG) embedded into the active region of the OLED to enhance outcoupling from waveguide modes of the device. Next, in Chapter IV, we demonstrate an improved LIG with reduced refractive index achieved by glancing-angle deposition (GLAD) of the grid material. In Chapter V, we use full-wave simulations to analyze a proposed outcoupling technique based on nanoparticle scattering films located between the OLED and the substrate. Lastly, in Chapter VI, we propose, model and present current experimental progress of an outcoupling technique based on a planarized grid directly outside

of the high-index regions of the OLED.

We introduce the basic principles of the strong-coupling regime and review prior work in Part II, Chapter VII. We investigate the physics of the recently demonstrated organic polariton laser in Chapter VIII. In Chapter IX, we utilize the strong-coupling regime to simultaneously couple organic and inorganic semiconductors to the same microcavity photon mode and demonstrate the first (to our knowledge) room-temperature Frenkel-Wannier-Mott hybrid state. Finally, we conclude with a discussion of potential extensions to the works presented in this dissertation in Chapter X.

CHAPTER I

Bibliography

[1] C. W. Tang and S. A. VanSlyke, *Appl. Phys. Lett.* **51**, 913 (1987).

[2] C. Adachi, M. A. Baldo, M. E. Thompson, and S. R. Forrest, *J. Appl. Phys.* **90**, 5048 (2001).

[3] N. Bardsley, S. Bland, L. Pattison, M. Pattison, et al., *Solid-State Lighting Research and Development Multi-Year Program Plan*, Technical Report (U.S. Department of Energy, May 2014).

[4] T. Young, *Phil. Trans. R. Soc. Lond.* **92**, 12 (1802).

[5] H. v. Helmholtz, *Treatise on Physiological Optics*, Vol. 2 (Dover, 2005), 479 pp.

[6] K. R. Gegenfurtner and L. T. Sharpe, *Color Vision: From Genes to Perception* (Cambridge University Press, 2001), 460 pp.

[7] A. Stockman, L. T. Sharpe, and C. Fach, *Vision Research* **39**, 2901 (1999).

[8] A. Stockman and L. T. Sharpe, *Vision Research* **40**, 1711 (2000).

[9] GrandDrake, *Diagram of the CIE 1931 color space*, (2012) http://commons.wikimedia.org/wiki/File:CIExy1931_Rec_709.svg.

[10] B. W. D'Andrade and S. R. Forrest, *Adv. Mater.* **16**, 1585 (2004).

[11] S. R. Forrest, *Chem. Rev.* **97**, 1793 (1997).

[12] M. Pope, *Electronic Processes in Organic Crystals and Polymers*, in collab. with C. E. Swenberg and M. Pope, 2nd ed (Oxford University Press, New York, 1999), 1328 pp.

[13] Vladsinger, *Orbital hybridization in benzene rings.* (2009) http://commons.wikimedia.org/wiki/File:Benzene_Orbitals.svg.

[14] M. Montalti, A. Credi, L. Prodi, and T. Gandolfi, *Handbook of Photochemistry* (Taylor & Francis, 2006), 633 pp.

[15] M. Mueller, *Fundamentals of Quantum Chemistry: Molecular Spectroscopy and Modern Electronic Structure Computations* (Springer, 2001).

[16] P. Atkins, *Quanta: A Handbook of Concepts* (Oxford University Press, 1991).

[17] E. Abers, *Quantum Mechanics* (Pearson Education, 2004), 528 pp.

[18] M. A. Baldo, D. F. O'Brien, Y. You, A. Shoustikov, et al., *Nature* **395**, 151 (1998).

[19] M. Baldo, D. O'Brien, M. Thompson, and S. Forrest, *Phys. Rev. B* **60**, 14422 (1999).

[20] C. Adachi, S. Tokito, T. Tsutsui, and S. Saito, *Jpn. J. Appl. Phys.* **27**, L713 (1988).

[21] C. W. Tang, S. A. VanSlyke, and C. H. Chen, *J. Appl. Phys.* **65**, 3610 (1989).

[22] M. A. Baldo, S. Lamansky, P. E. Burrows, M. E. Thompson, and S. R. Forrest, *Appl. Phys. Lett.* **75**, 4 (1999).

[23] G. Gu, V. Bulović, P. Burrows, S. Forrest, and M. Thompson, *Appl. Phys. Lett.* **68**, 2606 (1996).

[24] G. Gu, G. Parthasarathy, P. E. Burrows, P. Tian, et al., *J. Appl. Phys.* **86**, 4067 (1999).

[25] K. Walzer, B. Maennig, M. Pfeiffer, and K. Leo, *Chem. Rev.* **107**, 1233 (2007).

[26] S. R. Forrest, D. D. Bradley, and M. E. Thompson, *Adv. Mater.* **15**, 1043 (2003).

[27] D. S. Setz, T. D. Schmidt, M. Flämmich, S. Nowy, et al., *J. Photon. Energy* **1**, 011006 (2011).

[28] N. C. Giebink and S. R. Forrest, *Phys. Rev. B* **77**, 235215 (2008).

[29] Y. Zhang, M. Slootsky, and S. R. Forrest, *Appl. Phys. Lett.* **99**, 223303 (2011).

[30] P. Martin, *Handbook of Deposition Technologies for Films and Coatings: Science, Applications and Technology* (Elsevier Science, 2009).

[31] X. Tong, B. E. Lassiter, and S. R. Forrest, *Org. Electron.* **11**, 705 (2010).

CHAPTER II

Optical losses in OLEDs

A large fraction of light generated in an OLED does not escape the device in the forward viewing direction to provide useful illumination. The majority of this light is trapped in the substrate, the thin-film and metal regions and is eventually absorbed or edge-emitted. In this chapter, we briefly outline the three dominant optical loss pathways and their relative contribution to the outcoupling efficiency.

2.1 Substrate modes

In bottom-emitting OLEDs, light that is generated in the thin-film organic layers must travel through the substrate (typically glass or plastic) before being emitted into the forward viewing direction. At the substrate/air interface, the refractive index contrast causes total internal reflection (TIR). As illustrated in Fig. 2.1(a), this traps light incident beyond the critical angle, θ_c, in so-called *substrate* or *glass* modes. The critical angle can be calculated from Snell's law and is given by:

$$\sin(\theta_c) = n_{air}/n_{sub} \tag{2.1}$$

The refractive index of air is $n_{air} = 1$ while that for conventional glass is $n_{sub} = 1.5$, which yields a light escape cone with a half-angle of $\theta_c \approx 42°$. If we assume an isotropic emitter and no reflection or absorption losses, the fraction of outcoupled power can be estimated by the ratio of the area of the spherical dome inside the escape cone, as

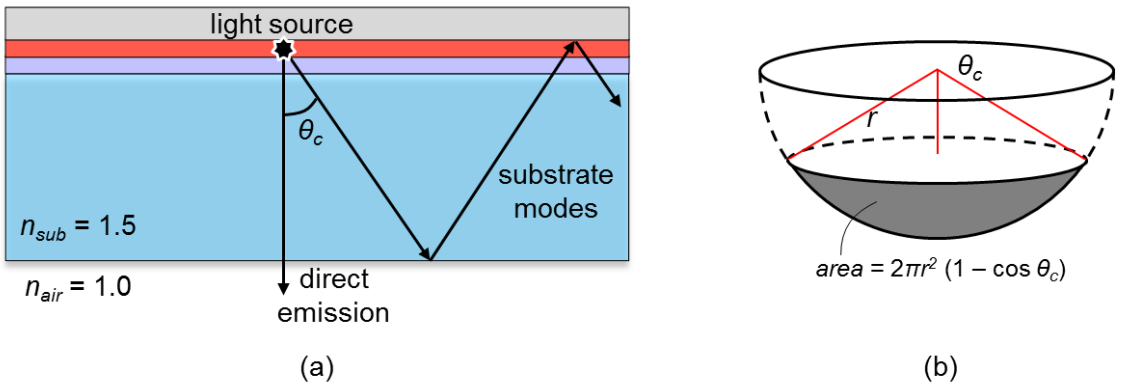

Figure 2.1: (a) Schematic of total internal reflection at the OLED substrate/air interface. Light emitted beyond the critical angle θ_c is trapped in substrate modes and is eventually lost to absorption or edge emission. (b) Area of the spherical dome defined by the escape cone in terms of radius r and angle θ_c.

shown in Fig. 2.1(b), to that of the forward hemisphere:

$$\eta_{out} \approx \frac{A_{out}}{A_{tot}} = \frac{2\pi r^2(1-\cos\theta_c)}{4\pi r^2/2} = 1-\cos\theta_c \tag{2.2}$$

More accurately, we need to account for angle-dependent Fresnel transmittance at the interface for light inside the escape cone (the transmittance is zero beyond the critical angle):

$$\begin{aligned} T_s &= 1-\left|\frac{n_{sub}\cos\theta-\sqrt{1-n_{sub}^2\sin^2\theta}}{n_{sub}\cos\theta+\sqrt{1-n_{sub}^2\sin^2\theta}}\right|^2 \\ T_p &= 1-\left|\frac{n_{sub}\sqrt{1-n_{sub}^2\sin^2\theta}-\cos\theta}{n_{sub}\sqrt{1-n_{sub}^2\sin^2\theta}+\cos\theta}\right|^2, \end{aligned} \tag{2.3}$$

where θ is the internal incidence angle, and the subscripts p and s specify the polarization of light. The total fraction of power that makes it to the outside world is obtained by integrating expressions in Eq. 2.3 over the forward hemisphere and averaging for

Table 2.1: Critical angle and outcoupling efficiency calculated for various materials using Eqs. 2.1–2.4. Refractive indices are approximate.

Material	n	θ_c	A_{out}/A_{tot}	η_{out}
GaAs	3.4	17.1°	4.4 %	3.0 %
GaN	2.5	23.6°	8.4 %	6.5 %
Flint glass	1.8	33.7°	16.8 %	14.5 %
Crown glass	1.5	41.8°	25.4 %	23.0 %

unpolarized light:

$$\eta_{out} = \int_0^{\pi/2} \frac{T_s(\theta) + T_p(\theta)}{2} \sin\theta \, d\theta \tag{2.4}$$

Light trapping due to TIR is not unique to OLEDs and is even more severe in conventional light-emitting diodes (LEDs) which are made from materials with higher refractive indices. Table 2.1 compares the critical angles and extraction efficiency of several different light-emitting devices. In inorganic LEDs where the emission occurs in a relatively thick bulk layer, the assumption of isotropic emission profile is reasonable. In OLEDs, however, the active layers are thin and have higher refractive indices than that of the glass substrate producing non-isotropic emission due to microcavity effects [1]. Moreover, light within the escape cone that undergoes Fresnel reflection may be returned to the glass/air interface after reflection from the metal, increasing the odds of outcoupling (if it is not lost to edge-emission or absorption). All these factors must be taken into account in a rigorous calculation.

In general, glass modes can be effectively outcoupled by modifying the external interface to prevent TIR e.g. by roughening the surface [2], attaching microlenses [3, 4], or using nanoporous or microparticle scattering films [5–8]. As discussed in §1.3.2, an index-matching liquid can be used to directly measure nearly all the light trapped in the substrate, giving an upper limit for extraction efficiency with glass mode outcoupling of only 40–50 %. The reason for this limitation, as detailed in the following sections, is the non-negligible coupling to waveguide modes in the organic and ITO layers, and surface

plasmon modes in the metal cathode, which together prevent nearly half the light from even entering the substrate.

2.2 Waveguide modes

The thin-films of an OLED form an asymmetric metal-dielectric slab waveguide. As shown in Fig. 2.2, the core of this waveguide consists of the high-index regions formed by the organics ($n \approx 1.7-1.8$) and ITO ($n = 1.8-2.0$). The guide is bound by the glass substrate and the reflective metal. Assuming the fields are harmonically oscillating ($\mathbf{F} \sim e^{-i\omega t}$) at a frequency ω, the modes of such a structure must satisfy the wave equation [9]:

$$\nabla^2\mathbf{F} + \omega^2\varepsilon\mu\mathbf{F} = 0. \tag{2.5}$$

Here, $\mathbf{F} = (F_x, F_y, F_z)$ can be either the $\mathbf{E}$ or $\mathbf{H}$ field. Choosing the y-axis as normal to the plane formed by the interfaces and the x-axis as the direction of propagation, the solutions take the form:

$$\mathbf{F}(\mathbf{r}, t) = \mathbf{F}(y)e^{i(\beta x - \omega t)} \tag{2.6}$$

where $\beta = k_{\|}$ is the in-plane momentum of the wave (also called the propagation constant in waveguide terminology). In a general multilayer dielectric stack, $k_{\|}$ is conserved across all the layers. Combining this with Eq. 2.5 we get

$$\frac{\partial^2}{\partial y^2}\mathbf{F}_i(z) + (n_i^2 k_0^2 - \beta^2)\mathbf{F}_i(z) = 0, \qquad i = (1,2,3) \tag{2.7}$$

where we have employed $\omega^2\varepsilon\mu = n^2k_0^2$ and i corresponds to the three regions of our waveguide as indicated in Fig. 2.2.

The fields of Eq. 2.6 must also satisfy the (pleasantly symmetric) Maxwell's equations

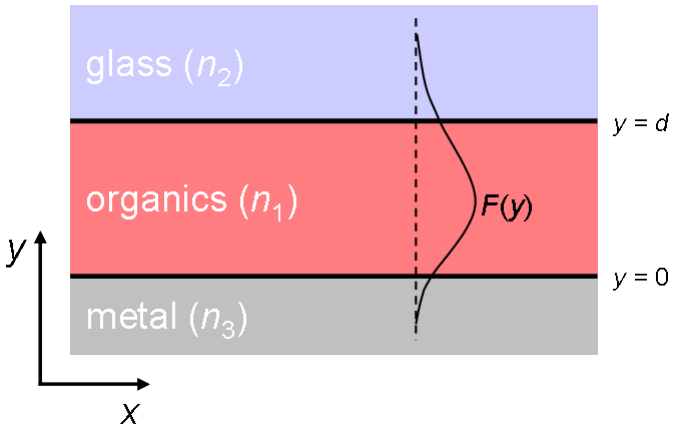

Figure 2.2: Structure of an asymmetric metal-dielectric slab waveguide formed by a typical bottom-emitting OLED. The transparent anode and various device layers have been simplified into a single "organics" layer since their optical constants are generally not very different. Here, d is the thickness of the core, and $n_1 > n_2, n_3$ is a necessary (but not sufficient) condition for existence of guided modes. A transverse field profile, $F(y)$, of one such mode is shown.

for harmonic fields [9]:

$$\begin{aligned} \nabla \times \mathbf{E} &= -i\omega\mu\mathbf{H} \\ \nabla \times \mathbf{H} &= \ i\omega\varepsilon\mathbf{E}. \end{aligned} \tag{2.8}$$

Making appropriate substitutions, we can write down the field components [10]:

$$\begin{aligned} \frac{\partial}{\partial y}E_z = -i\omega\mu H_x \qquad & \frac{\partial}{\partial y}H_z = i\omega\varepsilon E_x \\ \beta E_z = -\omega\mu H_y \qquad & \beta H_z = \omega\varepsilon E_y \\ i\beta H_y + \frac{\partial}{\partial y}H_x = -i\omega\varepsilon E_z \qquad & i\beta E_y + \frac{\partial}{\partial y}E_x = i\omega\mu H_z \end{aligned} \tag{2.9}$$

We have grouped these such that the three equations on the left-hand side contain only E_z, H_x and H_y, while the right-hand side consists of H_z, E_x and E_y. In the first set, the electric field is entirely perpendicular to the direction of propagation (x), and these equations describe so-called transverse electric (TE) modes. Likewise, the second set, where the magnetic field is normal, describes transverse magnetic (TM) modes of the

guide.

In the three regions of the waveguide, the transverse field, $E_z(y)$ or $H_z(y)$, of Eq. 2.6 is of the form:

$$\begin{aligned} F_z^{(2)}(y) &= F_2 e^{ik_\perp^{(2)}(y-d)} && y \geq d \\ F_z^{(1)}(y) &= F_1^e \cos(k_\perp^{(1)} y) + F_1^o \sin(k_\perp^{(1)} y) && 0 \geq y \geq d \\ F_z^{(3)}(y) &= F_3 e^{-ik_\perp^{(3)} y} && y \leq 0 \end{aligned} \tag{2.10}$$

where F_i are arbitrary constants used to match the field boundary conditions and $k_\perp^2 = n^2 k_0^2 - \beta^2$ is the normal component of the wavevector which we have explicitly assumed to be real in the core (region 1) to achieve a standing-wave solution. In general, this may not be the case: for example, surface plasmons (SPs) bound to the metal-dielectric interface are entirely evanescent in all regions, as will be discussed in the next section. In all cases, the field can only penetrate into a good metal (region 3) up to a skin depth $\delta = \sqrt{\frac{2\varepsilon_0 c^2}{\sigma\omega}}$ where σ is the conductivity. To create this evanescent field, $k_\perp^{(3)}$ must be purely imaginary i.e. $\beta > n_3 k_0$. Similarly, if $\beta > n_2 k_0$ in the low-index dielectric cladding, the field again decays exponentially and we have a fully confined waveguide mode like the one shown in Fig. 2.2. However, if $0 < \beta < n_2 k_0$, the fields are oscillatory in the cladding and the mode propagates away from the core; such modes are alternately called radiative, weakly guided or leaky. These result in the roughly 50 % of the light that makes it into the substrate.

Using Eq. 2.10 and the field relationships in Eq. 2.9 one can fully write down the fields in all three regions for both TE and TM modes. Enforcing continuity of tangential fields across interfaces leads to a set of equations from which the following dispersion relations can be derived [10] (here k is actually $k_\perp$, but we have dropped the subscript in favor of readability):

$$\text{TE:} \quad \tan(k_1 d) = -ik_1 \left(\frac{k_2 + k_3}{k_1^2 + k_2 k_3} \right) \tag{2.11}$$

$$\text{TM:} \quad \tan(k_1 d) = -i\varepsilon_1 k_1 \left(\frac{\varepsilon_3 k_2 + \varepsilon_2 k_3}{\varepsilon_2 \varepsilon_3 k_1^2 + \varepsilon_1^2 k_2 k_3} \right) \tag{2.12}$$

Generally, these transcendental equations must be solved numerically. However, we can get a qualitative understanding by looking at a simplified system with a perfect metal. In this case, $\varepsilon_3 \to -\infty$ and the tangential electric fields go strictly to 0 at the metal-dielectric interface. Equations 2.11 and 2.12 reduce to [10]:

$$\text{TE:} \quad \tan(k_\perp^{(1)} d) = -i \frac{k_\perp^{(1)}}{k_\perp^{(2)}} \tag{2.13}$$

$$\text{TM:} \quad \tan(k_\perp^{(1)} d) = -i \frac{\varepsilon_1 k_\perp^{(2)}}{\varepsilon_2 k_\perp^{(1)}} \tag{2.14}$$

As before, the transition between radiative and guided modes (sometimes called the cutoff) occurs when $k_\perp^{(2)} = 0$ (i.e. $\beta = n_2 k_0$). For TE modes at cutoff, this means the tangent in Eq. 2.13 approaches negative infinity, while for TM modes in Eq. 2.14 it goes to 0. This is satisfied when:

$$\begin{aligned} \text{TE:} \quad & k_\perp^{(1)} = (2m+1)\frac{\pi}{2d} \\ \text{TM:} \quad & k_\perp^{(1)} = \frac{m\pi}{d} \end{aligned} \tag{2.15}$$

where m is an integer that specifies the order of the mode. Thus, the guided modes are quantized and depend on the thickness of the core, the wavelength of light and the refractive indices of the layers. For a given thickness and free-space wavelength λ_0, there is a limited number of allowed modes given by the condition:

$$\begin{aligned} \text{TE:} \quad & d \geq \frac{2m+1}{\sqrt{n_1^2 - n_2^2}} \frac{\lambda_0}{4} \\ \text{TM:} \quad & d \geq \frac{m}{\sqrt{n_1^2 - n_2^2}} \frac{\lambda_0}{2} \end{aligned} \tag{2.16}$$

Evidently, a minimum thickness is required for at least one TE mode to exist; however,

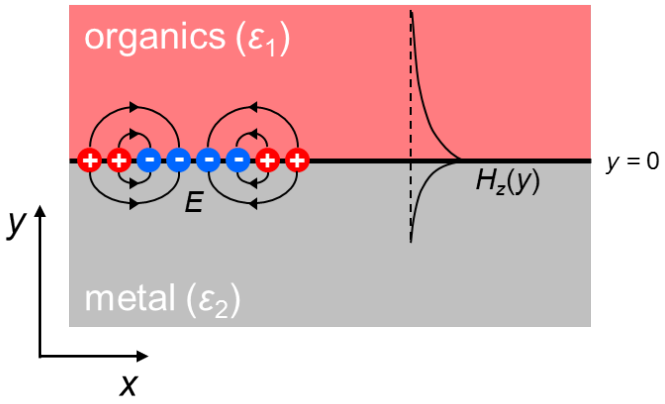

Figure 2.3: Schematic of the interface that supports surface plasmon modes. The oscillating surface charge distribution necessitates both normal and tangential electric field components thus limiting SP to TM modes. The magnetic field profile of the mode, $H_z(y)$, is shown.

no minimum thickness exists below which there are no TM modes. For an asymmetric waveguide, the lowest order TM mode is always present and is in fact identical to the SP mode [10].

2.3 Surface plasmon polaritons

Surface plasmons (SPs), or more formally – *surface plasmon polaritons*, are non-radiative guided modes confined to the interface between a metal and a dielectric that result from the coupling of the electric field with a surface charge density. To achieve such interaction, a component of the electric field must be normal to the interface: thus SP are associated with TM but not TE modes. As shown in Fig. 2.3, the field intensity is highest at the interface and decays exponentially in both films. The surface charge is the result of a discontinuity in the normal component of the field across the interface [10].

Like waveguided modes, SP fields take the form of Eq. 2.6 and satisfy Maxwell's curl relationships in Eq. 2.8. The transverse magnetic field components are the same as the

evanescent parts of a waveguide mode in Eq. 2.10:

$$\begin{aligned} H_z^{(1)}(y) &= e^{ik_\perp^{(1)} y} \qquad y \geq 0 \\ H_z^{(2)}(y) &= e^{-ik_\perp^{(2)} y} \qquad y \leq 0 \end{aligned} \tag{2.17}$$

where $y = 0$ is the interface, and regions (1) and (2) correspond to the dielectric and metal films, respectively. Since the fields decay exponentially, the normal component of the wavevector in both regions must be imaginary. We can use Eq. 2.9 to write the tangential TM components on both sides of the interface:

$$\begin{aligned} ik_\perp^{(1)} H_z^{(1)} &= i\omega\varepsilon_1 E_x^{(1)} \\ -ik_\perp^{(2)} H_z^{(2)} &= i\omega\varepsilon_2 E_x^{(2)} \end{aligned} \tag{2.18}$$

Given the continuity of tangential fields across the interface ($F_\parallel^{(1)} = F_\parallel^{(2)}$), we divide the expressions in Eq. 2.18 to arrive at

$$\frac{k_\perp^{(1)}}{\varepsilon_1} = -\frac{k_\perp^{(2)}}{\varepsilon_2}. \tag{2.19}$$

Recalling that $\beta = k_\parallel^{(1)} = k_\parallel^{(2)}$ by conservation of in-plane momentum and that $k^2 = \beta^2 + k_\perp^2 = \varepsilon\omega^2/c^2$, we can use the relationship in Eq. 2.19 to derive the SP dispersion relation:

$$\omega = \beta c / \sqrt{\frac{1}{\varepsilon_1} + \frac{1}{\varepsilon_2}}. \tag{2.20}$$

Since dielectric constant of metals is complex ($\varepsilon = \varepsilon' + i\varepsilon''$), the propagation constant of SPs will have both real and imaginary parts. The real in-plane momentum corresponds to harmonic wave propagation, while the imaginary component results in attenuation. Thus, after a short distance the SP mode is lost. For an interface between Al and Alq_3, the propagation distance is approximately 20 μm [10].

The frequency dependence of the real part of the metal dielectric constant can be

well approximated by the Drude-Sommerfeld model [11]:

$$\varepsilon'(\omega) = 1 - \frac{\omega_p^2}{\omega^2}, \qquad \omega_p^2 = \frac{ne^2}{\varepsilon_0 m}. \tag{2.21}$$

Here, ω_p is the plasma frequency; e, m and n are the electron charge, mass and density, respectively; and ε_0 is the permittivity of free space. At low frequencies, the metal dielectric constant approaches negative infinity, behaving like an ideal conductor, and Eq. 2.20 simplifies to light-like behavior: $\omega = \beta c/\sqrt{\varepsilon_1}$. At larger wavevectors, as the plasma frequency is approached, the dispersion asymptotes to $\omega = \omega_p/\sqrt{1+\varepsilon_1}$, as indicated in Fig. 2.4 [10]. Since the normal wavevector must be imaginary, $\beta > n_1 k_0$ and the surface plasmon dispersion always lies beyond the light-line of the adjacent dielectric. This means that there is no coupling between radiative or waveguided modes and the surface plasmons in this structure. The excitation of these modes in OLEDs occurs strictly through near-field evanescent coupling and depends strongly on the separation between the emitter and the metal surface [9, 12, 13].

2.4 Distribution of optical power

Figure 2.4 summarizes the ω-β dispersion characteristics of various modes in a typical OLED structure. In the air and substrate, there exists a continuum of available modes contained within the light-cones defined by $\omega/\beta = c/n$. The glass light-line has smaller slope reflecting the higher refractive index and hence reduced velocity of light. Likewise, the light-line for organic layers is beyond that of glass. However, as indicated by Eq. 2.15, there is only a discrete set of waveguide modes. Beyond the organic light cone where $\beta > n_1 k_0$, only surface plasmons are supported by the metal-dielectric interface. Emission originating in the organic layers couples to all these modes, but only the light within the air light-cone contributes to device efficiency. Glass mode light propagates laterally and is generally lost to edge emission while waveguide and

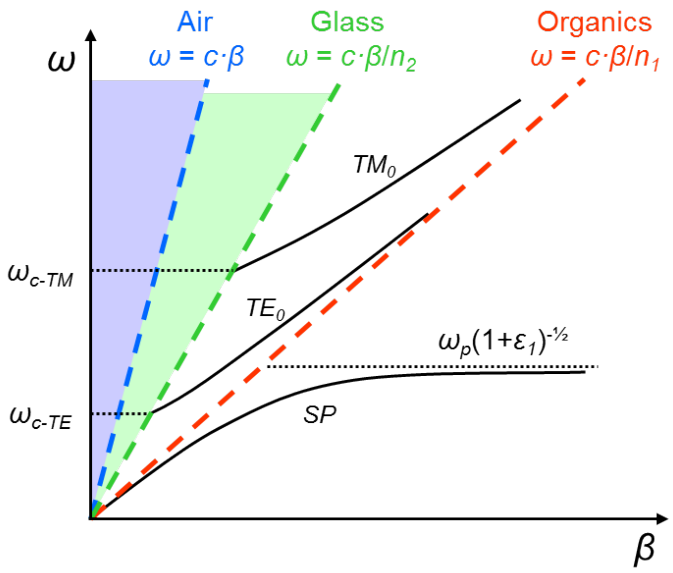

Figure 2.4: Dispersion diagram for an OLED. Within a layer, the in-plane momentum β of propagating light cannot exceed the total wave-vector $nk_0 = n\omega/c$ indicated by the dashed light-lines. In the organic core, the lowest of the quantized modes TM_0 and TE_0 are shown. Beyond the organic light-line, surface plasmons are supported by the metal-dielectric interface. Inside the glass cladding light cone, there is a continuum of available modes; however, due to TIR at the glass-air interface only a fraction of those is coupled to the outside world.

SP modes are lost to absorption in the electrodes and organic layers. The coupling to the modes (or alternatively, the amount of light extracted from the high-index regions) depends on the exact structure of the device and position of the emitting layer.

The radiative lifetime of the emitter is also weakly modified by the fields in the structure due to the Purcell effect [1, 14, 15]; generally emission at a field anti-node is favored. The radiative rate is also sensitive to near-field coupling between the emitter and the metal cathode. Chance, Prock and Silbey (CPS) treated this effect by modeling the emitter as a classical point-dipole whose field can be calculated using dyadic Green's functions [12, 13]. To accurately model the power flow into the modes of the planar multilayer structure of an OLED, various techniques were developed subsequently, including approaches based on transfer-matrix formalism with dipole source terms [16], eigenmode expansion [17], CPS extended with Fermi's golden rule [1], and direct cal-

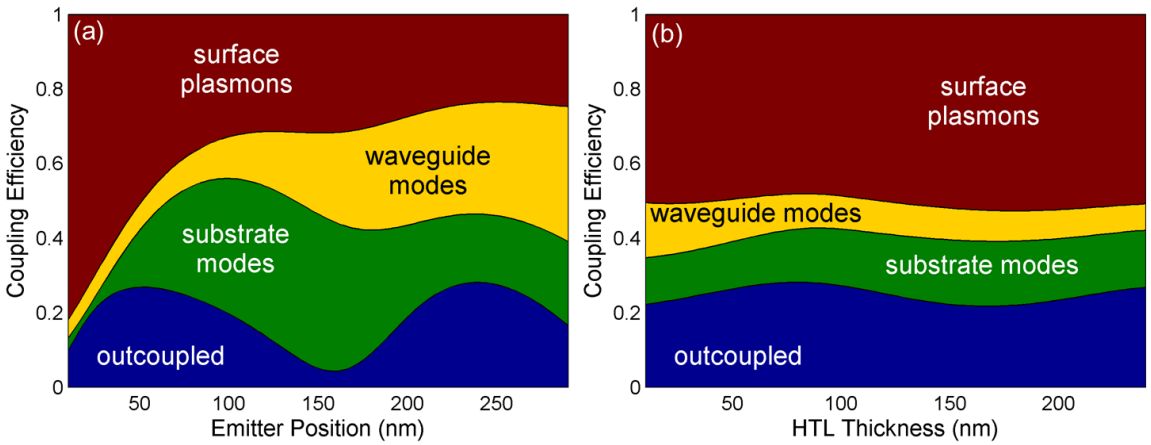

Figure 2.5: The coupling of emitted light to various modes as a function of (a) dipole distance from metal in a 300 nm thick organic layer, and (b) thickness of the HTL for a dipole positioned 50 nm from the cathode.

culation of the Poynting vector using dyadic Green's functions [18]. Using the latter, we plot the coupling of $\lambda = 550$ nm emission to different modes in Fig. 2.5 for two cases: (a) the structure is 100 nm Al/ 300 nm organic/ 100 nm ITO/ glass, and the emitter position is changed relative to the cathode; (b) the structure is Al/ 50 nm ETL/ emitter/ HTL/ ITO/ glass, and the HTL thickness is varied. It is apparent that the distribution of power is most sensitive to the separation between the metal and the emitter. At short distances, this is due to near-field coupling, while the periodic variation is due to the standing optical field.

For a given set of emitting layers, the device structure must be optimized optically by adjusting the film thicknesses within the electrical constraints. As an example, in Fig. 2.6, we show the combined emission spectrum of a stacked white OLED consisting of red (PQIr), green ($Ir(ppy)_3$) and blue (FIr6) emissive layers as in Ref. [19], simulated using CAMFR [20]. By rearranging the position of the emitters in the stack, the contribution of each color to the total outcoupled light is significantly altered. For a white OLED, this has consequences beyond simply affecting the outcoupling efficiency: if the spectrum is too far from a black-body emitter or the color coordinate is not white, the generated light will have a low CRI and will appear unpleasant.

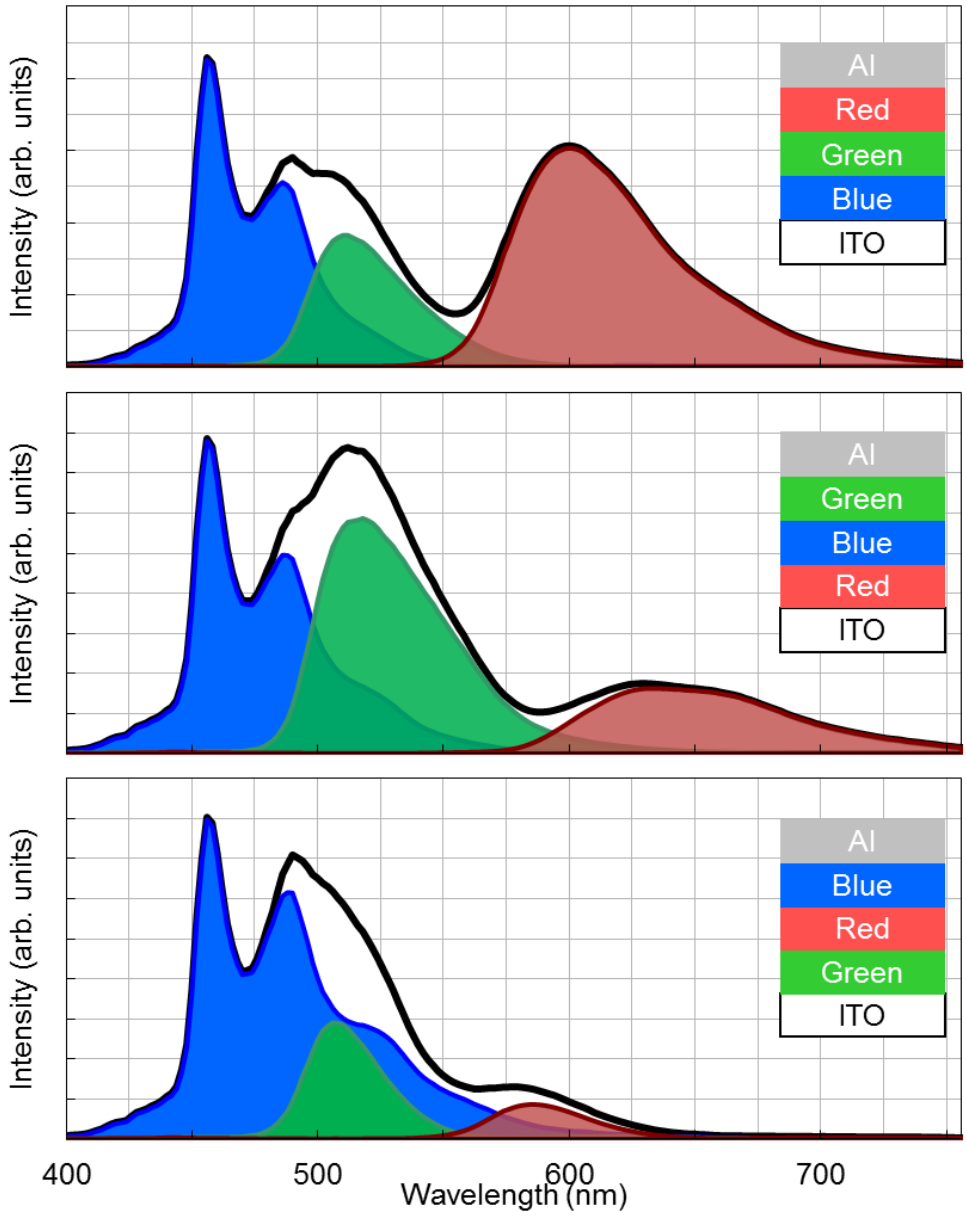

Figure 2.6: Simulated emission spectra of stacked white OLEDs consisting of separate red (PQIr), green ($Ir(ppy)_3$) and blue (FIr6) emitters as in Ref. [19]. Because the outcoupling for each wavelength and position in the stack is different, the total spectrum (black line) is changed when the emitting layers are rearranged. The spectra are normalized to the blue peak.

2.5 Conclusion

In this chapter, we briefly outlined the various optical losses to guided and non-radiative modes in OLEDs. Due to the combination of these effects, the outcoupling efficiency of conventional devices is around 20 %. Increasing light extraction is of the utmost importance for several reasons. Firstly, as we saw in §1.3.2, this would increase device efficiency and reduce power consumption. Second, since OLED EQE rolls off at higher current densities [21], equivalent luminance achieved at lower drive current using outcoupling will provide a compounded efficiency boost. Finally, OLED lifetime can also be prolonged in this operation regime since degradation is accelerated at higher current [22].

In typical photonic structures, coupling between various modes is achieved through the use of diffractive gratings where the periodicity, Λ, defines a grating wavevector: $K = 2\pi/\Lambda$. Guided modes (waveguide or plasmon) can then be folded into the escape cone in Fig. 2.4 by resonant scattering: $\beta_{final} = \beta_{initial} - K$. The drawback to this method is a strong wavelength and angle dependence which produces undesirable angular intensity distortion and spectral shifts. In the following chapters, we will numerically and experimentally explore light extraction techniques based on non-resonant scattering of trapped modes.

CHAPTER II

Bibliography

[1] V. Bulović, V. B. Khalfin, G. Gu, P. E. Burrows, D. Z. Garbuzov, and S. R. Forrest, *Phys. Rev. B* **58**, 3730 (1998).

[2] S. Chen and H. S. Kwok, *Opt. Express* **18**, 37 (2010).

[3] S. Moller and S. R. Forrest, *J. Appl. Phys.* **91**, 3324 (2002).

[4] Y. Sun and S. R. Forrest, *J. Appl. Phys.* **100**, 073106 (2006).

[5] H. J. Peng, Y. L. Ho, X. J. Yu, and H. S. Kwok, *J. Appl. Phys.* **96**, 1649 (2004).

[6] J. J. Shiang, T. J. Faircloth, and A. R. Duggal, *J. Appl. Phys.* **95**, 2889 (2004).

[7] R. Bathelt, D. Buchhauser, C. Gärditz, R. Paetzold, and P. Wellmann, *Org. Electron.* **8**, 293 (2007).

[8] Y.-H. Cheng, J.-L. Wu, C.-H. Cheng, K.-C. Syao, and M.-C. M. Lee, *Appl. Phys. Lett.* **90**, 091102 (2007).

[9] C. Yeh and F. Shimabukuro, *The Essence of Dielectric Waveguides* (Springer, 2008).

[10] P. A. Hobson, "Photonic modes of organic light emitting structures," PhD thesis (University of Exeter, 2002).

[11] C. Kittel, *Introduction to Solid State Physics* (Wiley, 2004).

[12] R. R. Chance, A. Prock, and R. Silbey, *J. Chem. Phys.* **62**, 771 (1975).

[13] R. Chance, A. Prock, and R. Silbey, "Molecular fluorescence and energy transfer near metal interfaces," in *Advances in Chemical Physics*, Vol. 37, edited by I. Prigogine and S. Rice (Wiley, New York, 1978).

[14] E. M. Purcell, *Phys. Rev.* **69**, 681 (1946).

[15] T. Tsutsui, C. Adachi, S. Saito, M. Watanabe, and M. Koishi, *Chem. Phys. Lett.* **182**, 143 (1991).

[16] H. Benisty, R. Stanley, and M. Mayer, *J. Opt. Soc. Am. A* **15**, 1192 (1998).

[17] P. Bienstman, "Rigorous and efficient modelling of wavelength scale photonic components," PhD thesis (Ghent University, 2001).

[18] K. Celebi, T. D. Heidel, and M. A. Baldo, *Opt. Express* **15**, 1762 (2007).

[19] X. Qi, M. Slootsky, and S. Forrest, *Appl. Phys. Lett.* **93**, 193306 (2008).

[20] *CAMFR: CAvity Modeling FRamework* (Dept. Inf. Technol., Ghent University, Belgium).

[21] N. C. Giebink and S. R. Forrest, *Phys. Rev. B* **77**, 235215 (2008).

[22] N. C. Giebink, B. W. D'Andrade, M. S. Weaver, J. J. Brown, and S. R. Forrest, *J. Appl. Phys.* **105**, 124514 (2009).

CHAPTER III

Full-wave simulation of OLEDs with an embedded low-index grid

Mehr Licht! (More Light!)

– Goethe's final words

3.1 Introduction

Organic light-emitting devices (OLEDs) have been thoroughly pursued in recent years as a viable alternative for large-area white lighting and display applications due to their high brightness and low power-consumption [1]. A typical bottom-emitting device uses a transparent ITO anode deposited on a glass substrate. The organic layers are grown onto the ITO and are capped by a metal cathode [2]. The light is generated in the organic layers when the injected charges form excitons and recombine, producing photons that are subsequently emitted through the ITO and substrate. Using phosphorescent dopants, nearly 100 % internal quantum efficiency (IQE) in OLEDs has been demonstrated [3]; however, the external quantum efficiencies (EQEs) remain low due to incomplete extraction of light from the emissive layers. As discussed in Chapter II, this is due to the refractive index differences at the substrate-air and ITO-substrate interfaces, resulting in total internal reflection (TIR) that traps light in the substrate (producing so-called *substrate* or *glass* modes), and in the high-index ITO and organic layers (*waveguide* modes). In an OLED on a flat glass substrate, these effects limit EQE

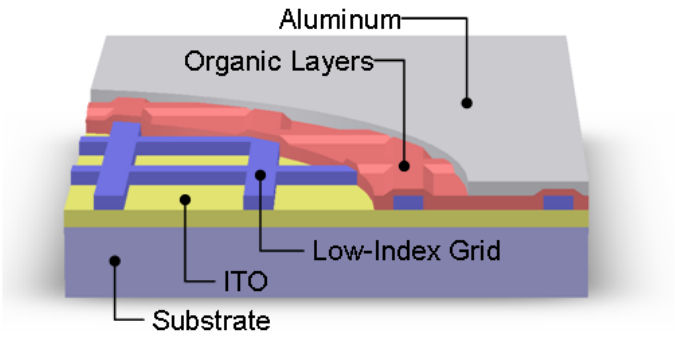

Figure 3.1: Schematic illustration of the embedded low-index grid (LIG) used for outcoupling waveguided light

to ∼20 %, while ∼30 % of the light is trapped in the substrate and ∼50 % in the lossy waveguide and plasmon modes [4, 5].

Several methods for enhancing the outcoupling efficiency of these devices have been proposed [4, 6–13]. Many of these methods only extract glass modes, and those that outcouple waveguide modes tend to suffer from distorted angular emission profiles and a strong wavelength dependence which makes them undesirable for display and lighting applications. Furthermore, practical outcoupling schemes must be simple (and hence low cost) to implement. Since more than half of the emitted light is confined to the high-index regions, effective waveguide mode extraction opens an avenue to significant gains in external quantum and power efficiencies, and potentially longer lifetimes due to the ability to achieve a given brightness at a relatively low operating current.

In 2008, Sun and Forrest [2] experimentally demonstrated a method for extracting waveguided light via an embedded low-index grid (LIG) inserted within the organic layers (Fig. 3.1). While the embedded grid scatters the waveguided modes, only a fraction of the scattered light will couple directly to viewable air modes, as some of this light is trapped in the substrate due to TIR. Fortunately, the vast majority of the light extracted from the high-index regions by the LIG can be further outcoupled into the forward viewing direction using low cost and wavelength independent schemes such as microlens arrays [2]. Indeed, using a grid made of silica (SiO_2, refractive index

$n = 1.45$) and a polymer microlens array, a device with $EQE = 34\,\%$, corresponding to 2.3 times that of a conventional OLED on a glass substrate, was demonstrated [2]. Moreover, since the width of the organic region in the spaces between the grid lines is much larger than the emission wavelength, the outcoupling enhancement was found to be wavelength and viewing angle independent. In this chapter, we use full-wave electromagnetic simulations to further investigate the dependence of the outcoupling enhancement on LIG parameters such as refractive index, width of the organic and low-index regions, and grid geometry.

3.2 Simulation methods

The simulations were performed with the COMSOL Multiphysics (ver. 3.4) finite element analysis software [14]. For simplicity, the OLED structure was modeled as a 100-nm-thick homogeneous organic layer sandwiched between a 100-nm-thick aluminum cathode and a 100-nm-thick ITO anode layer on an optically thick glass substrate. With the exception of the cathode, all layers are assumed to be lossless, with refractive indices of $n_{ITO} = 1.8$, $n_{org} = 1.75$ and $n_{glass} = 1.45$. Although there is measurable absorption in these layers, particularly in the anode, this has only a slight impact on the relative improvement between control and LIG devices which are both subject to similar absorption losses. The Lorentz-Drude model [15] is used to calculate the complex index of refraction of the Al cathode. It is crucial to include the metal extinction in order to account for both absorption of waveguided modes and near-field coupling of the emitter to SPs. Unless noted otherwise, all of the simulations were performed at a wavelength of $\lambda = 550\,\text{nm}$ (close to the peak spectral response of the human eye).

The non-uniformity introduced by the deposition of the organic and cathode layers onto the LIG was neglected and instead all planar interfaces were assumed. This focuses the simulation to the effects on waveguide but not SP modes. Moreover, since a microlens array can be used to outcouple nearly all glass modes produced by the LIG,

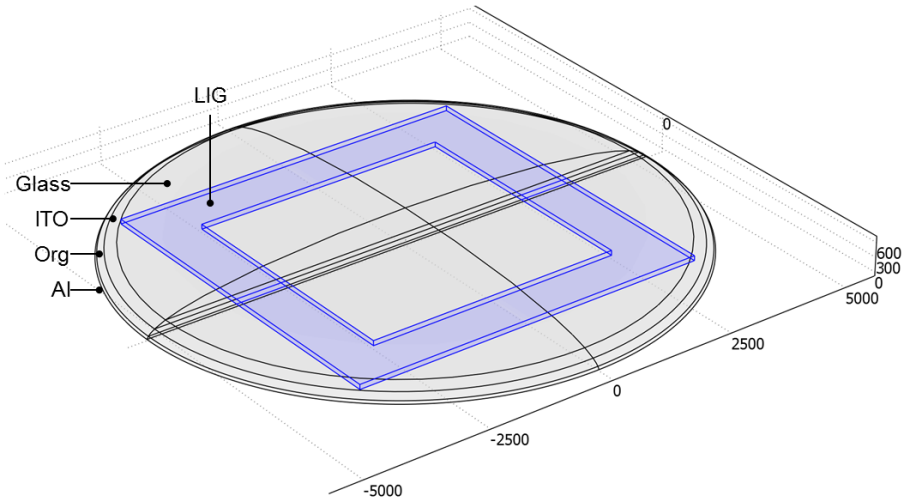

Figure 3.2: Hemispherical simulation domain. The thickness of the Al, organic and ITO layers is 100 nm. All emitted power flows out through the hemispherical boundary or is absorbed by the metal. Units are nm.

we restricted our analysis to calculating only the combined glass and air modes in the substrate disregarding the substrate-air interface. Since the index difference between the ITO and glass is relatively small, the waveguided modes are loosely confined and the evanescent field extends over 200 nm into the substrate (i.e. $\sim 33\,\%$ of the waveguided light lies outside of the ITO/organic region). Thus, care must be taken when separating the waveguided modes from the glass and air modes in the substrate.

A hemispherical simulation domain was chosen such that all the power emitted into waveguide, glass and air modes flows through the hemispherical surface (Fig. 3.2). Unless noted otherwise, the radius of the model domain was 5.4 μm and the height was 1.5 μm allowing sufficient room for light scattered by the grid to be distinctly separated from the still-confined modes. The scattering boundary condition was used for the external boundaries. This provides a transparent surface with no reflections back into the model without the added computational complexity of perfectly matched layers. The sub-domains of the model were meshed such that the linear element size remained below $\lambda/(5n)$ where n is the refractive index in the domain, producing 3-5 million mesh elements for the entire volume. Due to computer memory limitations, the model was

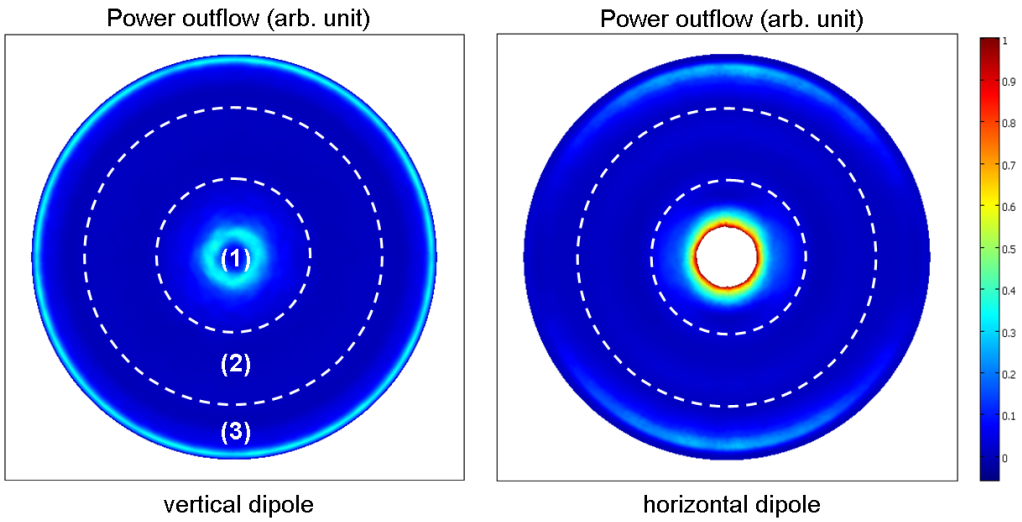

Figure 3.3: Simulated power flow through the curved surface of the simulation domain for vertical and horizontal dipole orientations in a conventional OLED projected onto a plane. The dashed lines roughly delineate (1) air modes, (2) substrate modes, and (3) waveguide modes. The majority of light from the vertical dipole is waveguided as seen by the light-blue ring near the edge of the model. For the horizontal dipole, the scale is compressed to show the presence of waveguided light; the vast majority of power, however, is in the clipped region in the center.

solved iteratively using the generalized minimal residual (GMRES) solver.

The light source was modeled as a randomly oriented electric dipole source [5] located in the center of the hemisphere and in the middle of the organic layer. The total emitted power was measured by summing the power flow from the external waveguide and substrate boundaries with power dissipated to the cathode: $P_{tot} = P_{sub} + P_{wav} + P_{cath}$. Since a randomly oriented dipole can be decomposed into horizontal (in-plane) and vertical (normal to the substrate) components, the average emitted power for is obtained following: $P_{ave} = \frac{2}{3}P_{\parallel} + \frac{1}{3}P_{\perp}$. Because dipoles radiate power mainly equatorially, the majority of the radiation emitted by the vertical dipoles in an OLED is confined to the high-index regions, while the horizontal dipole only couples weakly into the waveguide modes (Fig. 3.3). Therefore, we expect the enhancement due to the LIG to be more pronounced for a vertical than for a horizontal dipole.

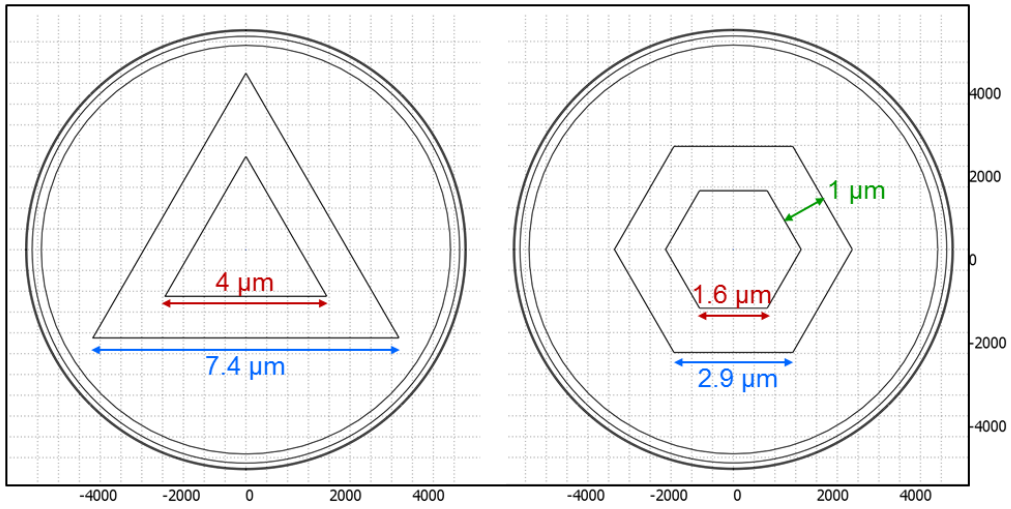

Figure 3.4: Triangular and hexagonal cell geometries. The square unit cell (not shown) has inner dimension of 2.6 µm. The LIG widths are approximately 1 µm for all geometries.

3.3 Unit cell shape

To determine dependence on grid shape, three space-filling unit cells were modeled: square, triangular and hexagonal. The width of the grid was kept at $w = 1\,\mu\text{m}$ for all three, while the overall dimensions were adjusted to achieve roughly equal ratio of organics-to-LIG area yielding inner edge lengths of 2.6 µm, 4 µm and 1.6 µm, respectively (Fig. 3.4). The refractive index was set at $n = 1.1$.

Figure 3.5 shows the simulated power flow through the hemisphere for the three geometries. As expected, the dominant scattering by the LIG occurs for the strongly guided light emitted by the vertical dipole Fig. 3.5(a,c,e). A small amount of light is scattered for the horizontal dipole. The difference between the two horizontal dipole orientations in the asymmetric triangular and hexagonal cells is negligible. Relative to the control, the amount of light that enters the substrate is increased by a factor of 1.45 for square and hexagonal cells and 1.43 for the triangular cell. For the triangular cell, the simulation domain edge is close to the vertices making it difficult to correctly assign the peaks overlapping the dashed line; likely the outcoupling is slightly underestimated.

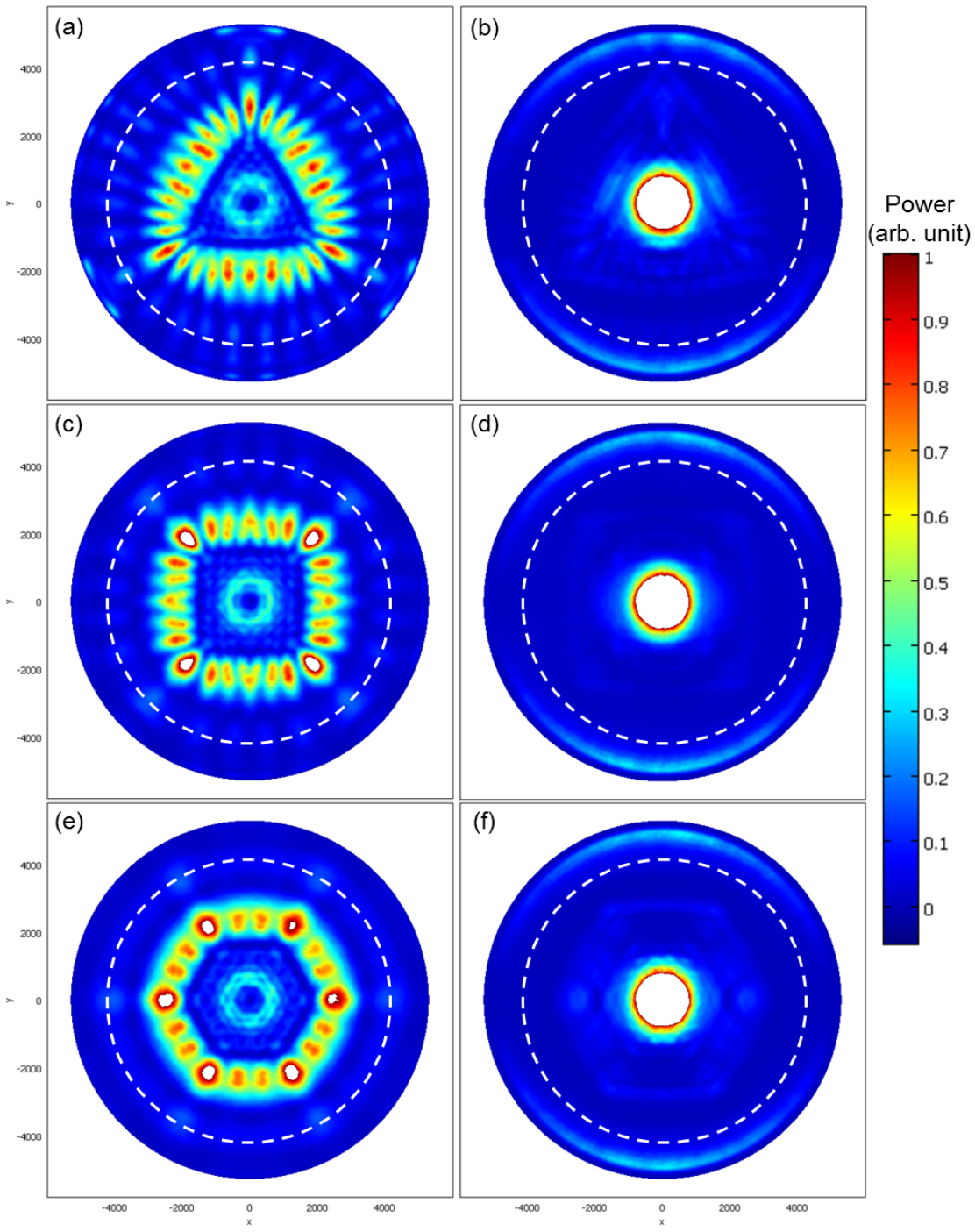

Figure 3.5: Power outflow from the vertical and horizontal dipoles surrounded by triangular (a,b), square (c,d) and hexagonal (e,f) low-index ($n = 1.1$) unit cells. Dashed line approximately separates waveguide and glass/air modes. The color scale is normalized to that in (a).

In any case, the difference between the three shapes is negligible. Examining the outer edge for the vertical dipole emission (i.e. the waveguided light), it is apparent that little power remains beyond the LIG. Indeed, simulations with a 3×3 square cells show that the first cell of the square grid provides more than 90 % of the total enhancement, allowing us to neglect cells beyond the one containing the source dipole.

3.4 Wavelength dependence

Experimentally, the SiO_2 LIG was found to have no wavelength dependence [2]. Likewise, in simulation, we confirmed that the enhancement is not strongly dependent on the wavelength (Fig. 3.6) using a grid with $n = 1.05$, width $w = 1\,\mu\text{m}$ and periodicity $p = 6\,\mu\text{m}$. The extremely low refractive index means that the optical width of the grid is smallest and thus most susceptible to wavelength-dependent interference effects. While there is a small variation of 5–10 % in enhancement across the visible spectrum, the actual fraction of power in glass and air modes in the LIG device trends similarly to the control. Therefore, the variation can be attributed to the weak microcavity effects inherent in thin film structures [5] and the dispersion in the Al optical constants (ITO and organic layers were assumed to have fixed refractive index).

3.5 Effect of grid dimensions

For the square grid, the effects of the grid width (w) and grid period (p) were also investigated. In the first case, simulations were performed for organic widths $w_{org} = 4\,\mu\text{m}$, $5\,\mu\text{m}$ and grid index $n = 1.1$. Although, this changes the period since $p = w_{org} + w$, the distance from the dipole to the inner edge of the grid is unchanged. The maximum fraction of light in the combined glass and air modes is 0.56 and 0.54, an increase of 1.3 and 1.25, respectively, over that for a conventional OLED, as shown in Fig. 3.7. If the glass mode light is coupled into the air modes, this enhancement

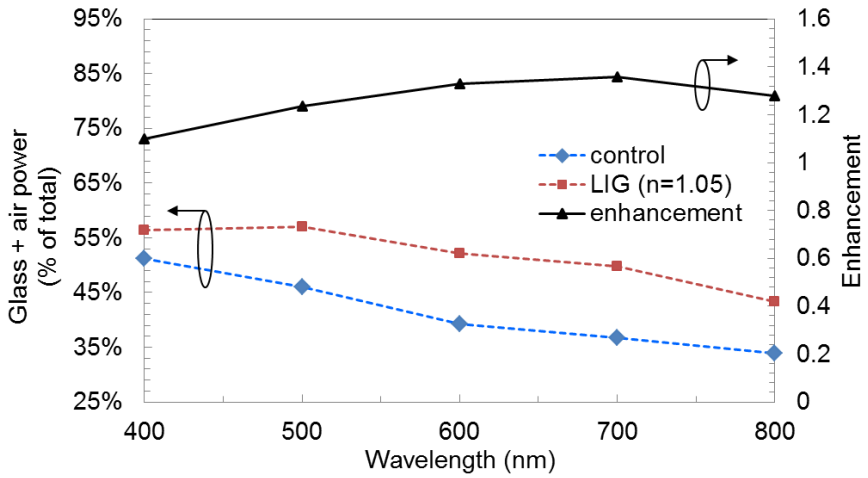

Figure 3.6: LIG outcoupling wavelength dependence. The grid parameters are $n = 1.05$, $w = 1\,\mu m$ and $p = 6\,\mu m$.

corresponds to outcoupling efficiencies exceeding 50%. Additionally, it is found that the enhancement increases with the LIG width up to a width of approximately $1\,\mu m$; beyond which further increases in w_{LIG} leave the outcoupling unchanged. This width corresponds to approximately two wavelengths in the low-index material, and indicates a transition to a fully scattered regime without interference effects.

By decreasing the period (i.e. the width of the organic region), additional light can be extracted from the waveguide into the substrate, as shown in Fig. 3.8. The simulations here, were performed for a grid with $w = 0.5\,\mu m$ and $n = 1.1$. Using data from Fig. 3.7 and adjusting the period accordingly, we estimate the maximum saturated enhancement for $w = 1\,\mu m$ to be approximately 5.5 % higher than the thinner grid. When varying periodicity, two issues must be considered: (i) the active device area must be large enough to provide sufficient brightness per device area as demanded by the application (e.g. displays or illumination sources), and (ii) the spacing must remain much larger than the wavelength to avoid interference effects which distort the emission spectrum and angular profile. Evidently, despite the reduced area due to the LIG, the enhanced outcoupling efficiency more than overcomes the reduction in luminance. For example, a 2.3-fold increase in EQE was observed [2] for a LIG where $w = 1\,\mu m$ and $p = 7\,\mu m$,

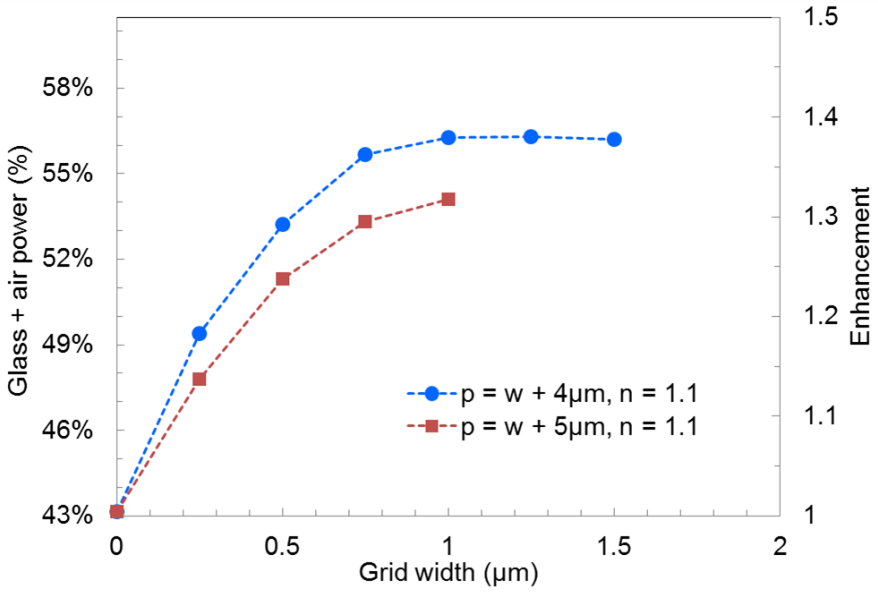

Figure 3.7: Outcoupling dependence on grid width, w, for organic widths of $w_{org} = 4\,\mu m$ and $w_{org} = 5\,\mu m$ and grid refractive index $n = 1.1$. The outcoupling enhancement saturates at $w > 1\,\mu m$.

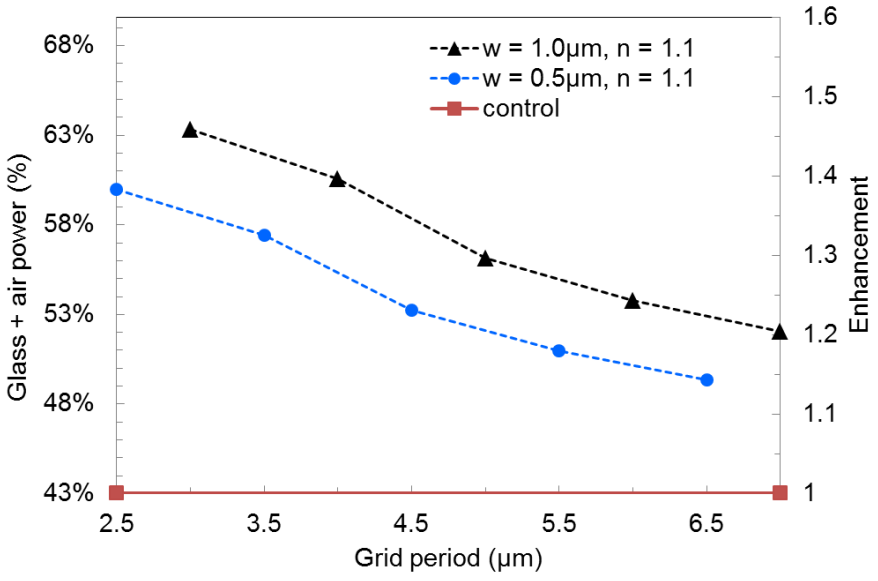

Figure 3.8: Outcoupling dependence on grid period for grid widths $w = 0.5\,\mu m$, $1\,\mu m$ and $n = 1.1$. The thicker grid is estimated by using the data in Fig. 3.7 and adjusting the periodicity accordingly.

corresponding to only 18 % reduction in emitting area. Hence, the second restriction on the minimum width of the organic region is of primary concern. At $w_{org} < 2\,\mu m$, interference effects may distort the emission spectrum. Moreover, because the fraction of active area with a LIG is given by $\frac{w_{org}^2}{p^2}$, the practical dimension is likely to be greater than the minimum allowed by interference considerations.

3.6 Effect of grid refractive index

Our simulations show that decreasing the refractive index of the LIG leads to a higher outcoupling efficiency. As indicated in Fig. 3.9, the fraction of power in glass and air modes is increased from 50 % by a grid with $n = 1.45$, $p = 3.6\,\mu m$, $w = 1\,\mu m$, to 65 % when the index is lowered to $n = 1.03$. Given the enhancement achieved experimentally at $n = 1.45$ [2], the model predicts significant room for improvement by reducing the dielectric refractive index even further. A moderate improvement can be practically achieved through a different choice of LIG material (e.g. MgF_2, commonly used for antireflection coatings with $n \approx 1.38$). However, ultra-low refractive indices close to that of air require more exotic selections such as the highly porous silica aerogel ($n = 1.03$) which has been used previously to enhance outcoupling in OLEDs [11] or obliquely deposited porous SiO_2 ($n = 1.05$) which has been employed to produce broadband antireflection coatings [16]. In Chapter IV, we will show experimentally that indeed reducing the refractive index allows enhanced outcoupling.

3.7 Discussion and conclusion

Experimentally, Sun et al. measured an improvement of approximately 1.32 in outcoupling into glass and air modes [2]. Using the same grid size and index parameters, our model significantly underestimates the outcoupling enhancement from the high-index regions for a conventional device at about 1.07. There are several likely reasons

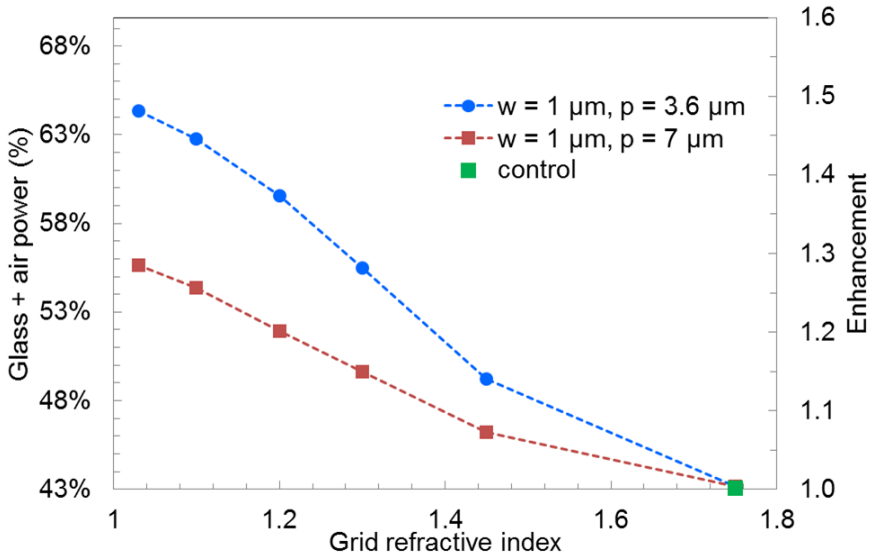

Figure 3.9: Outcoupling dependence on grid refractive index for grids with $p = 3.6\,\mu\text{m}$, $7\,\mu\text{m}$ and $w = 1\,\mu\text{m}$.

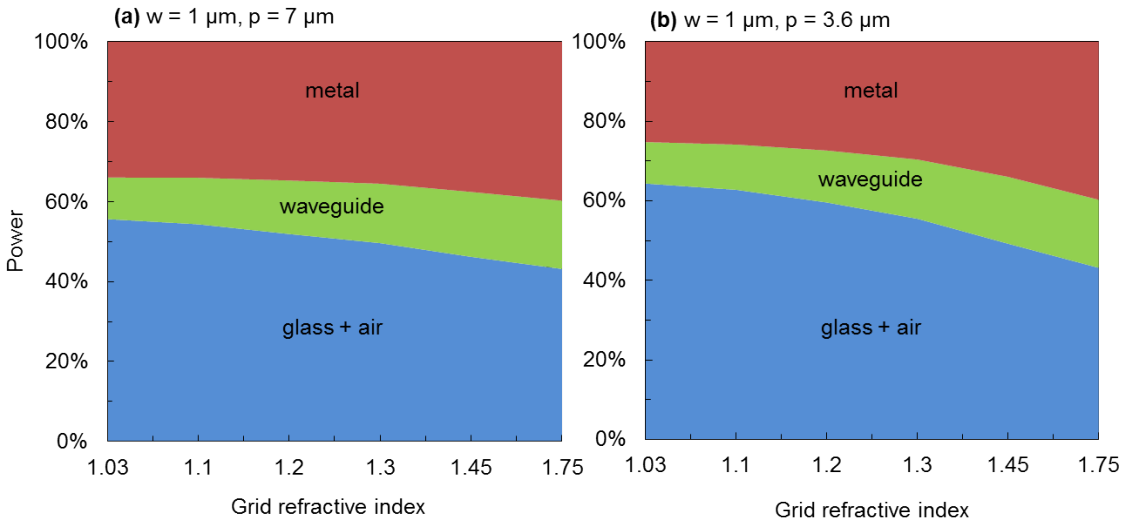

Figure 3.10: Simulated power distribution between glass/air, waveguide and metal dissipation for (a) $p = 7\,\mu\text{m}$ and (b) $p = 3.6\,\mu\text{m}$ LIGs (both with $w = 1\,\mu\text{m}$) as a function of refractive index. In both cases, a significant portion of the outcoupling enhancement comes from reducing loss to the metal in addition to scattering waveguided light.

for this. First, the experimental structure actually consists of three distinct emissive layers which are slightly spatially separated and spectrally broad. These differences change the intrinsic coupling to waveguided modes in the control device and thus the ability for the light to be extracted by the LIG. Similarly, the ITO thickness used experimentally is slightly greater, which can increase the amount of waveguide-confined light in the control device. Next, due to hardware limitations the mesh resolution of the metal surface is limited. The effect is to slightly underestimate losses to the metal both from near-field coupling with the dipole and from waveguided mode absorption. As mentioned previously, the absorption losses were also not modeled within the ITO and organic layers. Finally, the most significant factor is the non-uniformity introduced by depositing the OLED over the embedded grid which can serve to scatter both modes in the waveguide and surface plasmons in the metal. In Fig. 3.10, we plot the distribution of power among outcoupled light, waveguided modes and dissipation in the cathode as a function of refractive index for the two grids in Fig. 3.9. Clearly, the extra light extracted to glass and air modes by the LIG comes from reducing both waveguided light and loss to the cathode. Thus, it is quite certain that the enhancement due to the LIG is greater in absolute terms than indicated by the simulation due to the simplifying assumptions. Nonetheless, the *relative* effects of varying the simulated LIG parameters are not expected to depend strongly on the precise geometry. Thus, we expect these trends to be reflected in experimental results along with the added effects of metal corrugation.

In summary, we have presented the methodology for modeling outcoupling structures in OLEDs using a full-wave electromagnetic simulation. We find that, indeed, a low-index dielectric grid embedded in the organic layers of an OLED considerably increases the extraction of light trapped in the high-index organic layers and the ITO anode. Furthermore, simulations indicate that an optimized ultra-low-index grid can increase the amount of light outcoupled from the waveguided modes by as much as

50 %, and if combined with efficient outcoupling of glass modes into air can lead to very high external quantum and power efficiencies, without the drawback of producing changes in the electroluminescence spectra. Hence, low-index grids are a promising outcoupling solution for full color OLED displays and white solid-state lighting.

CHAPTER III

Bibliography

[1] S. R. Forrest, *Chem. Rev.* **97**, 1793 (1997).

[2] Y. Sun and S. R. Forrest, *Nat. Photon.* **2**, 483 (2008).

[3] C. Adachi, M. A. Baldo, M. E. Thompson, and S. R. Forrest, *J. Appl. Phys.* **90**, 5048 (2001).

[4] Y.-J. Lee, S.-H. Kim, J. Huh, G.-H. Kim, et al., *Appl. Phys. Lett.* **82**, 3779 (2003).

[5] V. Bulović, V. B. Khalfin, G. Gu, P. E. Burrows, D. Z. Garbuzov, and S. R. Forrest, *Phys. Rev. B* **58**, 3730 (1998).

[6] C. F. Madigan, M. H. Lu, and J. C. Sturm, *Appl. Phys. Lett.* **76**, 1650 (2000).

[7] Y. Sun and S. R. Forrest, *J. Appl. Phys.* **100**, 073106 (2006).

[8] T. Nakamura, N. Tsutsumi, N. Juni, and H. Fujii, *J. Appl. Phys.* **97**, 054505 (2005).

[9] S.-H. Cho, Y.-W. Song, J.-g. Lee, Y.-C. Kim, et al., *Opt. Express* **16**, 12632 (2008).

[10] J. Ziebarth, A. Saafir, S. Fan, and M. McGehee, *Adv. Func. Mater.* **14**, 451 (2004).

[11] T. Tsutsui, M. Yahiro, H. Yokogawa, K. Kawano, and M. Yokoyama, *Adv. Mater.* **13**, 1149 (2001).

[12] T. Yamasaki, K. Sumioka, and T. Tsutsui, *Appl. Phys. Lett.* **76**, 1243 (2000).

[13] P. Hobson, S. Wedge, J. Wasey, I. Sage, and W. Barnes, *Adv. Mater.* **14**, 1393 (2002).

[14] *COMSOL Multiphysics*, ver. 3.4 (Comsol Inc., Stockholm, Sweden, 2008).

[15] A. D. Rakić, A. B. Djurišić, J. M. Elazar, and M. L. Majewski, *Appl. Opt.* **37**, 5271 (1998).

[16] J.-Q. Xi, M. F. Schubert, J. K. Kim, E. F. Schubert, et al., *Nat. Photon.* **1**, 176 (2007).

CHAPTER IV

Extraction of waveguided light in OLEDs using an ultra-low-index grid

4.1 Introduction

Organic light-emitting devices (OLEDs) have potential use in full-color displays and white lighting applications. Although phosphorescent OLEDs can reach near unity internal quantum efficiency [1], their external quantum efficiency (EQE) remains near 20 % due to inefficient light extraction [2]. In a conventional OLED where light is emitted from the glass substrate surface, nearly 50 % of the produced light is confined in waveguide modes due to the refractive index mismatch between the transparent indium-tin-oxide (ITO, $n = 1.8$) electrode and substrate ($n = 1.45$); similarly, the index difference at the substrate-air interface results in additional ∼30 % loss due to total internal reflection (glass modes) [2]. Consequently, outcoupling schemes for increasing EQE and luminous efficacy are needed to allow for higher luminance at a given current density, or alternatively to operate at a reduced current density to achieve a desired luminance, thereby prolonging the operational lifetime.

Numerous techniques have been proposed to efficiently outcouple glass mode light, including surface roughening and microlenses, but only a few methods extract waveguide modes without detrimentally affecting the emission spectrum and angular profile. In this work, we focus on the previously demonstrated silica (SiO_2) low-index grid (LIG, $n = 1.45$) embedded in the organic layer of the OLED, which has been shown to

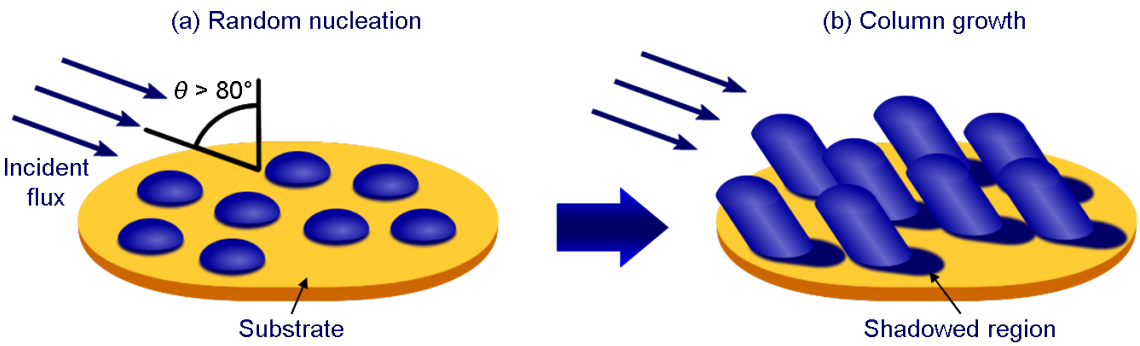

Figure 4.1: Schematic of glancing-angle deposition (GLAD). The substrate is positioned such that incident material flux is at a large angle to the substrate normal. (a) Initial nucleation on the substrate is random. (b) Self-shadowing causes material to be preferentially deposited only where there is already growth producing tilted columns.

efficiently scatter waveguided light into the substrate and forward viewing direction [3]. Using numerical full-wave electromagnetic field simulations we demonstrated in Chapter III that the outcoupling should significantly increase as the refractive index of the LIG material is reduced to that of air, theoretically allowing $EQE > 50\,\%$ [4]. In this chapter, we utilize glancing-angle deposition (GLAD) of SiO_2 to form ultra-low index films that serve as a basis for our new grid. Consistent with numerical simulations, this leads to a significant improvement in light-extraction from the waveguide compared to the previous aclig.

4.2 Glancing-angle deposition (GLAD) and grid fabrication

Although, in general, optical dielectric materials have $n > 1.35$ (approximately that of MgF_2 [5] and some polymers [6]) for visible wavelength light, ultra-low-index films have been achieved by using highly porous materials e.g. silica aerogels ($n = 1.03$) [7] and nanostructured films ($n = 1.05$) deposited using GLAD [8, 9]. The latter of these methods is particularly attractive for the fabrication of LIGs due to the relative ease of the deposition method: by placing the substrate at an oblique angle to a directional material flux, highly porous tilted pillar structures can be grown due to self-shadowing

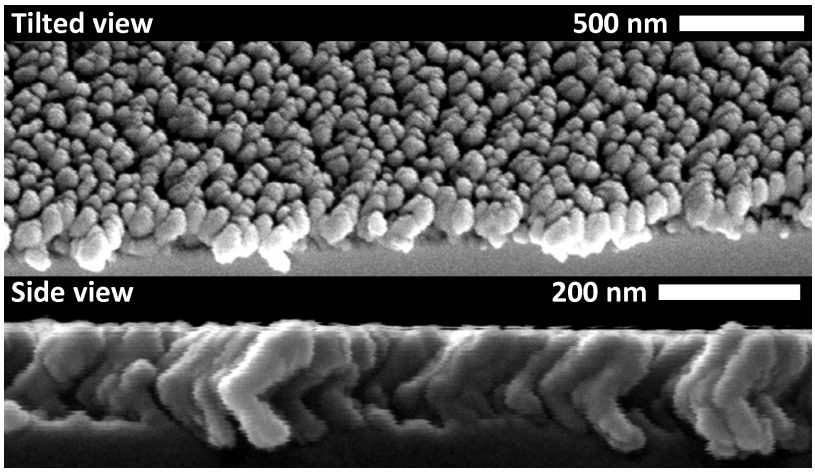

Figure 4.2: The surface (top) and cross-sectional (bottom) SEM images of obliquely deposited porous SiO_2 used for the UltraLIG. The chevron shaped pillars are grown by two subsequent GLAD growths, rotating the substrate 180° in between.

(Fig. 4.1. Although the size and spacing of the pillars is influenced by the initial random nucleation and adatom mobility of the material on the substrate [10], the simplest means of controlling the porosity of the film is by varying the incident flux angle [11]. Since the resulting features are on a scale smaller than the visible emission wavelengths of the OLED, the effective medium approximation is valid, and the films appear homogeneous to visible light with an index of refraction much lower than that of the source material [9].

To create an ultra-low-index grid (UltraLIG), highly porous 100-nm-thick SiO_2 films were deposited (Fig. 4.2) on commercial, pre-patterned ITO-coated glass at an oblique angle using an e-beam evaporator. The material was deposited at a rate of $\sim$10 Å/s, at a chamber pressure of 2×10^{-6} torr, and at an incidence angle of 80–85° to the substrate normal. The thickness and optical constants of the films were measured using variable-angle spectroscopic ellipsometry. Films with refractive indices of $n = 1.10 - 1.15$ in the visible were consistently obtained (see Fig. 4.3), while previous works have demonstrated values as low as $n = 1.05$ by further optimizing growth conditions [8, 9]. The porous films were isotropic, producing identical optical constants

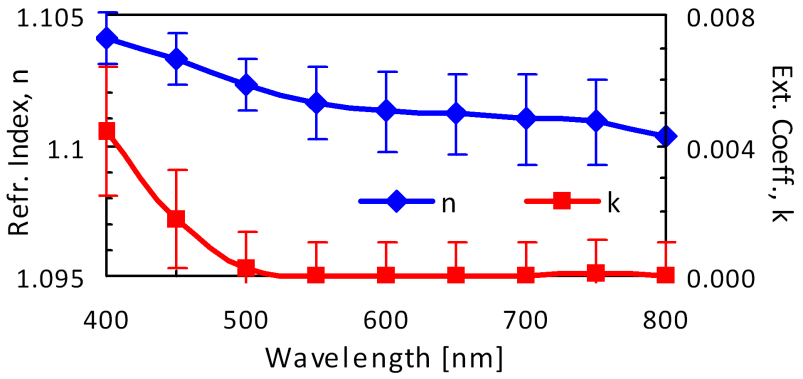

Figure 4.3: Optical constants n (diamonds) and k (squares) measured by ellipsometry of a 110-nm obliquely deposited SiO_2 film. The corresponding density of this film is 23.9 ± 0.1 % that of conventional, e-beam deposited SiO_2.

regardless of orientation with only a minor directional dependence when oriented along the growth direction. If necessary, this can be eliminated by introducing azimuthal substrate rotation during deposition to produce corkscrews, chevrons as in Fig. 4.2, or vertical columns instead of tilted pillars [11]. The resulting nanostructured films are capable of withstanding repeated solvent treatments, as well as application and removal of photoresist without noticeable damage.

When using large-area substrates for GLAD, the evaporated material flux can be noticeably different between the top and bottom of the substrate due to differing distance from the source resulting in a thickness gradient. Using a 4" Si wafer, we mapped the thickness variation after a single 100 nm growth, shown in Fig. 4.4(a). Within the top 1" of the substrate holder, the uniformity is better than 5 %; however, the film is nearly 50 % thicker at the bottom of the substrate due to the increased flux. For small-area devices (substrate size <2.5 cm, even this level of uniformity is sufficient. Regardless, the problem is almost entirely mitigated by a second GLAD growth after a 180° azimuthal rotation. This compensating deposition brings the thickness uniformity across the entire wafer to within 10 % as shown in Fig. 4.4(b). In both cases, the refractive index remains at a low $n = 1.16$ regardless of film thickness. An even greater degree of uniformity could be achieved with continuous azimuthal rotation, but this is beyond the scope of

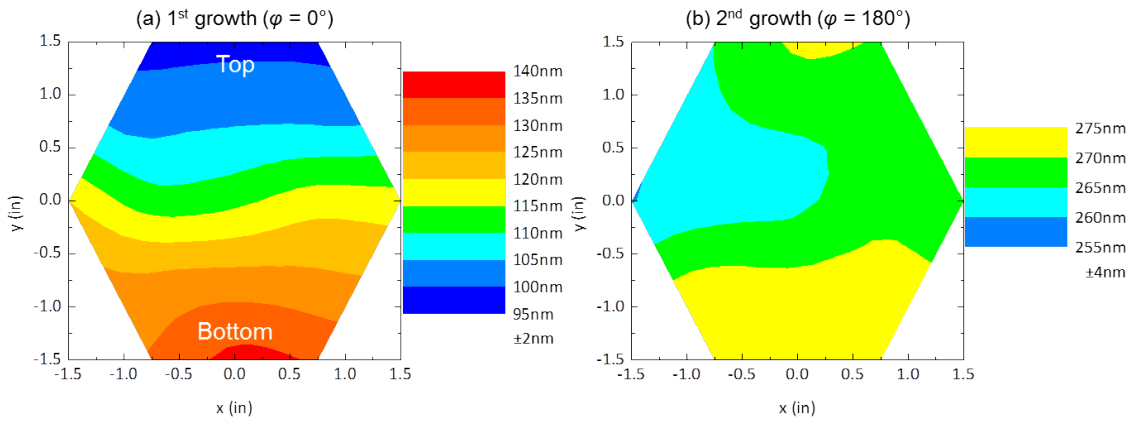

Figure 4.4: GLAD thickness uniformity over a 4" Si wafer after (a) a single growth and (b) after a 180° azimuthal rotation and second growth.

this work.

A grid pattern consisting of 6 µm × 6 µm square openings with 1 µm spacing identical to that of [3] was used. According to simulations, the 1 µm spacing is optimal for outcoupling waveguide modes. A small additional enhancement can be achieved by shrinking the size of the openings, although this may introduce undesirable angle- or wavelength-dependent extraction [4]. To define the grid, photoresist was spin-coated onto the porous film, lithographically exposed, and developed following previous methods [3]. During spin-coating, the photoresist penetrates the porous silica, completely filling in the voids, and thus protecting against etchant penetration and undercut of the defined structure in subsequent steps. The film was dry etched for 4 min in a parallel plate RIE reactor using a 1:1 CF_4:CHF_3 plasma (20 mTorr, 150 W RF power), followed by a 5-sec wet etch in buffered oxide etch (J.T.Baker 5334, NH_4 34.3 wt%: HF 6.48 wt%) diluted 7:1 with deionized water to remove any residual polymer and SiO_2 accumulation. The photoresist was removed by soaking the substrates for 5–10 min in a 1:1:5 NH_4OH:H_2O_2:H_2O solution at 105 °C (RCA organic clean), followed by a sequential solvent clean with hot trichloroethylene (140 °C), sonicated acetone, and hot isopropanol (150 °C) for 2 × 5 min each, and a 5-min exposure to UV-Ozone.

4.3 OLED fabrication and testing

The OLED layers were deposited onto the UltraLIG and conventional control substrates by vacuum thermal evaporation (chamber base pressure: 1×10^{-7} torr). Shadow masks were applied to the substrates in a nitrogen ambient prior to deposition of the cathode to define 1-mm-square devices. The electrophosphorescent device structure consisted of ITO (100 nm)/ NPD (40 nm)/ CBP doped with 8 wt% $Ir(ppy)_3$ (25 nm)/ BCP (10 nm)/ Alq_3 (25 nm)/ LiF (8 Å)/ Al (80 nm). While this green-emitting OLED was chosen for simplicity, previous work has shown that the LIG outcoupling is wavelength-independent across the visible spectrum due to the large feature size of the grid compared to the emission wavelength [3].

The current-density–voltage–luminance (J-V-L) characteristics of the devices were collected using a semiconductor parameter analyzer (HP-4156A) and a calibrated Si photodetector (Hamamatsu S3584-08). The current density for the UltraLIG devices was adjusted by a factor of $\left(\frac{6}{7}\right)^2$ to account for the reduced active area resulting from the dielectric grid. The electrophosphorescent spectrum was measured using a miniature fiber-optic spectrometer (OceanOptics 4000). EQE and PE were then calculated using standard methods [12]. Because the embedded grid redirects light into both air and glass modes, substrate outcoupling via the attachment of microlenses is typically necessary for optimum performance [3]. In this work, an IML with $n_{IMF} = 1.51$ was applied between the calibrated photodetector and substrate to extract the glass mode light with nearly 100 % efficiency without affecting waveguide outcoupling. This allows for direct measurement of the substrate quantum efficiency (SQE) and is necessary to separate the waveguide outcoupling effects from glass mode outcoupling.

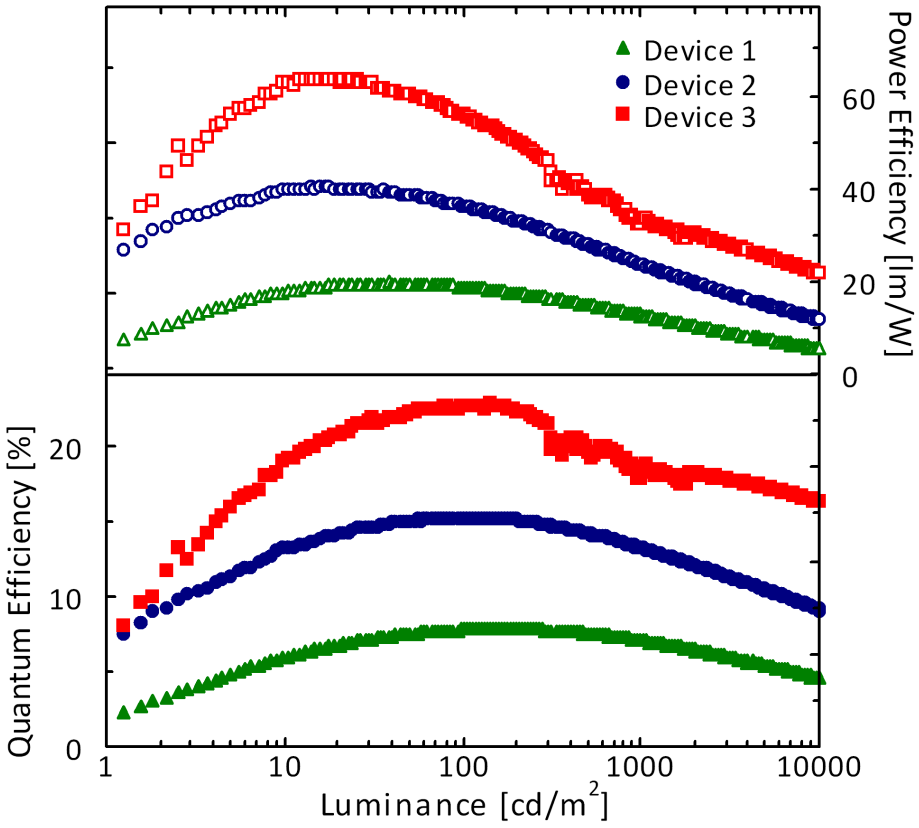

Figure 4.5: Luminous power (top) and quantum (bottom) efficiencies as functions of total OLED luminance in the forward-viewing direction. Device 1 (triangles) is a conventional OLED structure, Device 2 (circles) is Device 1 measured using an index matching liquid (IML) between the glass substrate and the photodetector to outcouple all substrate modes, and Device 3 (squares) is for an UltraLIG using an IML

4.4 Outcoupling performance

Quantum and power efficiencies are plotted as functions of luminance in Fig. 4.5 for three devices: (1) a conventional OLED with no outcoupling, (2) a conventional OLED with IML glass mode outcoupling, and (3) an UltraLIG ($n \approx 1.15$) based OLED with IML. Peak forward-viewing efficiencies of $EQE = 22.5 \pm 0.3\%$ and $PE = 64 \pm 3\,\mathrm{lm/W}$ are obtained for Device 3 compared to $EQE = 7.8 \pm 0.1\%$ and $PE = 20 \pm 2\,\mathrm{lm/W}$ for the conventional Device 1, and $EQE = 15.4 \pm 0.2\%$ and $PE = 40 \pm 2\,\mathrm{lm/W}$ for glass outcoupled Device 2. By comparing the light output of devices 2 and 3, a $48 \pm 4\%$ increase in light extraction from waveguided modes by the UltraLIG is observed at a luminance of $100\,\mathrm{cd/m^2}$, compared to $34 \pm 2\%$ enhancement obtained previously with an $n = 1.45$ LIG [3]. As with the previous work, the UltraLIG outcoupling exceeds the approximately 24 % enhancement predicted by numerical simulation due to the artificially high performance of the simulated control device in [4]. However, if the control device is relatively adjusted to the experimental data of [3], the predicted improvement in waveguide extraction for $n = 1.15$ is approximately 47 %, close to that of the experimental UltraLIG-based device. Additionally, the combined outcoupling of the IML and UltraLIG leads to a total performance increase of 2.9 and 3.0 over the conventional device in both the external quantum and power efficiencies, respectively.

The enhancement remains relatively constant (2.9 ± 0.3 total and 1.45 ± 0.04 waveguide outcoupling) at luminances between 10–$1000\,\mathrm{cd/m^2}$ (see Fig. 4.6); however, below and above these values, the enhancement increases (Fig. 4.6 inset) due to the unavoidable small variations between devices being amplified. In the low luminance regime near the device turn-on, the increase appears to be unrelated to the UltraLIG, as it is present in the ratio of the glass-outcoupled device EQE to that of the control. It is possible that charge imbalance shifts the position of the emission region, affecting the light extraction efficiency from the waveguide modes. On the other hand, at high current densities, the device efficiency also decreases; here, small differences in film morphol-

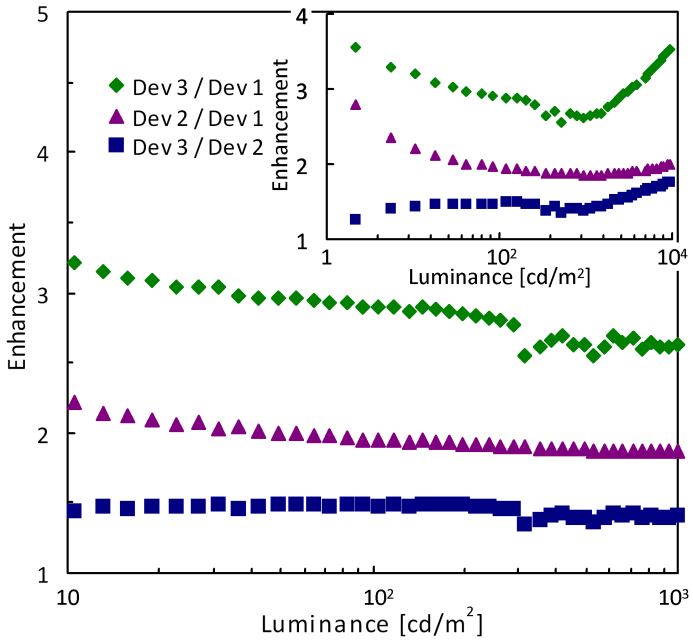

Figure 4.6: Device efficiency enhancement ratios as functions of luminance. Squares are the ratio of outputs of Dev3 to Dev2 (see Fig. 4.5), triangles compare Dev2 to Dev1, and diamonds compare the UltraLIG device (Dev3) to a conventional OLED (Dev1). Inset: The data in Fig. 4.6 over a greater range of luminance.

ogy or other effects may alter the efficiency roll-off behavior. As expected, the power efficiency enhancement follows the same trends as *EQE*.

4.5 Conclusion

In summary, an ultra-low-index grid is fabricated by obliquely depositing a highly porous but nearly isotropic film of SiO_2 with the resulting index of $n \approx 1.15$. Patterning of the UltraLIG was accomplished using standard lithographic techniques to define the grid onto which a phosphorescent OLED is evaporated. The embedded grid efficiently scatters light normally trapped in the high-index layers of the OLED, with nearly 50 % more light extracted from waveguided modes, an enhancement of ∼1.4 over a previously demonstrated $n = 1.45$ grid. The improvement is nearly constant across a wide range of luminance and is in reasonable agreement with prior full-wave electromagnetic simulations. Moreover, when glass mode light is additionally outcoupled at the

substrate-air interface by an index matching fluid, a three-fold enhancement in external quantum and luminous power efficiencies is produced compared to a conventional OLED. This method extends previous work [3], and inherits its advantages in terms of wavelength-independence, non-directionality and scalability making it applicable to both large-area indoor lighting and full-color high-resolution displays.

CHAPTER IV

Bibliography

[1] C. Adachi, M. A. Baldo, M. E. Thompson, and S. R. Forrest, *J. Appl. Phys.* **90**, 5048 (2001).

[2] V. Bulović, V. B. Khalfin, G. Gu, P. E. Burrows, D. Z. Garbuzov, and S. R. Forrest, *Phys. Rev. B* **58**, 3730 (1998).

[3] Y. Sun and S. R. Forrest, *Nat. Photon.* **2**, 483 (2008).

[4] M. Slootsky and S. R. Forrest, *Appl. Phys. Lett.* **94**, 163302 (2009).

[5] D. M. Roessler and D. R. Huffman, "Magnesium fluoride," in *Handbook of optical constants of solids II*, edited by E. D. Palik (Academic Press, Mar. 21, 1991), pp. 899–918.

[6] S. M. Jeong, F. Araoka, Y. Machida, K. Ishikawa, et al., *Appl. Phys. Lett.* **92**, 083307 (2008).

[7] T. Tsutsui, M. Yahiro, H. Yokogawa, K. Kawano, and M. Yokoyama, *Adv. Mater.* **13**, 1149 (2001).

[8] J.-Q. Xi, J. K. Kim, and E. F. Schubert, *Nano Lett.* **5**, 1385 (2005).

[9] J.-Q. Xi, M. F. Schubert, J. K. Kim, E. F. Schubert, et al., *Nat. Photon.* **1**, 176 (2007).

[10] L. Abelmann and C. Lodder, *Thin Solid Films* **305**, 1 (1997).

[11] K. Robbie and M. J. Brett, *J. Vac. Sci. Technol. A* **15**, 1460 (1997).

[12] S. R. Forrest, D. D. Bradley, and M. E. Thompson, *Adv. Mater.* **15**, 1043 (2003).

CHAPTER V

Full-wave simulation of nanoparticle scattering films

5.1 Introduction

In Chapters III and IV, we demonstrated numerically and experimentally how a dielectric low-index grid embedded in the organic layers of an OLED can enhance efficiency by scattering light normally confined in the high-index regions of the device. While quite effective, there are some drawbacks to utilizing such structures. Aside from reduced device area, the significant non-uniformity introduced by the grid complicates OLED growth and can lead to electrical shorting or accelerated degradation. An alternative approach recently demonstrated by several groups [1–3] is to use a diffuse scattering film consisting of nano-particles (NPs) embedded in a host layer and positioned between the substrate and ITO. The NP diameter is generally 200–500 nm in diameter. For example, Lee et al. [3] used a high-index TiO_2 host with embedded SiO_2 nanoparticles, while the groups of Chang [1] and Gather [2] used spin-coated polymer hosts with TiO_2 nanoparticles. The enhancement in *EQE* was reported by these groups to be roughly $1.7-2.13$. However, since the measurement of combined glass and air mode light was not reported, the exact nature of the outcoupling enhancement is unclear. Table 5.1 summarizes the performance of these scattering films along with the methods discussed in previous chapters. Presently, we investigate the effect of this technique on waveguided light extraction and its dependence on various optical and geometric parameters.

Table 5.1: Performance summary of outcoupling techniques. For waveguide outcoupling methods, the *SQE* is listed when available. The enhancement is calculated from source data at peak *EQE* or in the region of relatively constant improvement, rather than in the roll-off region where the efficiency is low and small differences in electrical behavior can result in anomalously high apparent improvement.

Outcoupling method	*EQE* enhancement	*SQE* enhancement	Refs.
Microlens array	1.7	-	[4]
Index-matching liquid IML	$2-2.5$	-	[4, 5]
LIG + microlens array	2.3	1.36	[4]
UltraLIG + IML	2.9	1.5	[5]
TiO_2 NPs/ polymer host	1.7	*NR*	[1]
TiO_2 NPs/ polymer host	1.45	*NR*	[2]
TiO_2 NPs/ polymer host + macro-extractor	2.13	1.07*	[2]
SiO_2 NPs/ TiO_2 host	2	*NR*	[3]

NR = Not reported, *estimated assuming macro-extractor doubles EQE

5.2 Simulation methods

The numerical simulations were performed using COMSOL Multiphysics (ver. 3.5) [6]. The simplified OLED structure consists of three 100 nm layers (Al, organics, ITO) on glass and identical optical constants were used as those in Chapter III. Since the evanescent fields of the waveguide and surface plasmon modes only extend approximately 400 nm into the substrate, we can restrict the simulation to thin scattering films. The nanoparticles are modeled as spheres with uniform diameters ($d = 200$ nm or 300 nm) in different geometric configurations. The simulation domain is hemispherical with a diameter of 5 μm and height of 3 μm such that all the light not absorbed by the cathode escapes through the curved surface, as before. The fraction of total power outcoupled to the substrate (*SQE*) is calculated for a randomly oriented dipole as before. Unless specified otherwise, simulations were performed for $\lambda = 550$ nm light. Here, the iterative GMRES method was again used to solve for the fields in the model.

5.3 Dependence on scatterer distance from ITO

The main attractive features of the scattering film are its position external to the electrically active regions of the device, its nearly planar nature, and in Refs. [1, 2] the ease of fabrication by simple spincoating. However, the random nature of the NPs distribution within the relatively thick film means that many scatterers may be far removed from the evanescent fields of the waveguided modes. To investigate the dependence on distance from ITO, we begin by modeling a single monolayer of high-index nano-spheres ($n = 2.6$) placed into a host layer with a glass-matched index of $n = 1.5$. The spheres are arranged in a regular square lattice. The outcoupling enhancement into the substrate is calculated for three separations of the monolayer from ITO: 0, 50 and 100 nm. Figure 5.1 shows the side view of the resulting power flux of vertical and horizontal dipole emission for a lattice with sphere radius $r = 300$ nm and period $p = d$ (approximately 50 % volume loading). When the nanoparticles are adjacent to the ITO surface, there is clear scattering out of the waveguide for both dipole orientations and the overall outcoupling enhancement is 1.51. However, as the distance between the scattering monolayer and ITO is increased, significantly less waveguide light is extracted from the vertical dipole. Moreover, the high-index spheres detrimentally trap part of the horizontal dipole emission. Thus, the outcoupling is reduced to 1.07 and 0.98 relative to the control for distances of 50 nm and 100 nm, respectively.

In Fig. 5.2, the enhancement in SQE is plotted for several monolayer configurations as a function of distance from ITO. The decreased outcoupling trend is repeated for a sparser monolayer ($p = 1.414d$ or ∼25 % volume loading) for source dipoles located directly under a sphere and those centered beneath the gap between spheres. A similarly sparse array of smaller spheres ($d = 200$ nm) also performs worse as the separation from ITO is increased. Intuitively, the low-index barrier between the waveguide and the nanoparticles prevents significant scattering interaction since the field decays exponentially in the cladding.

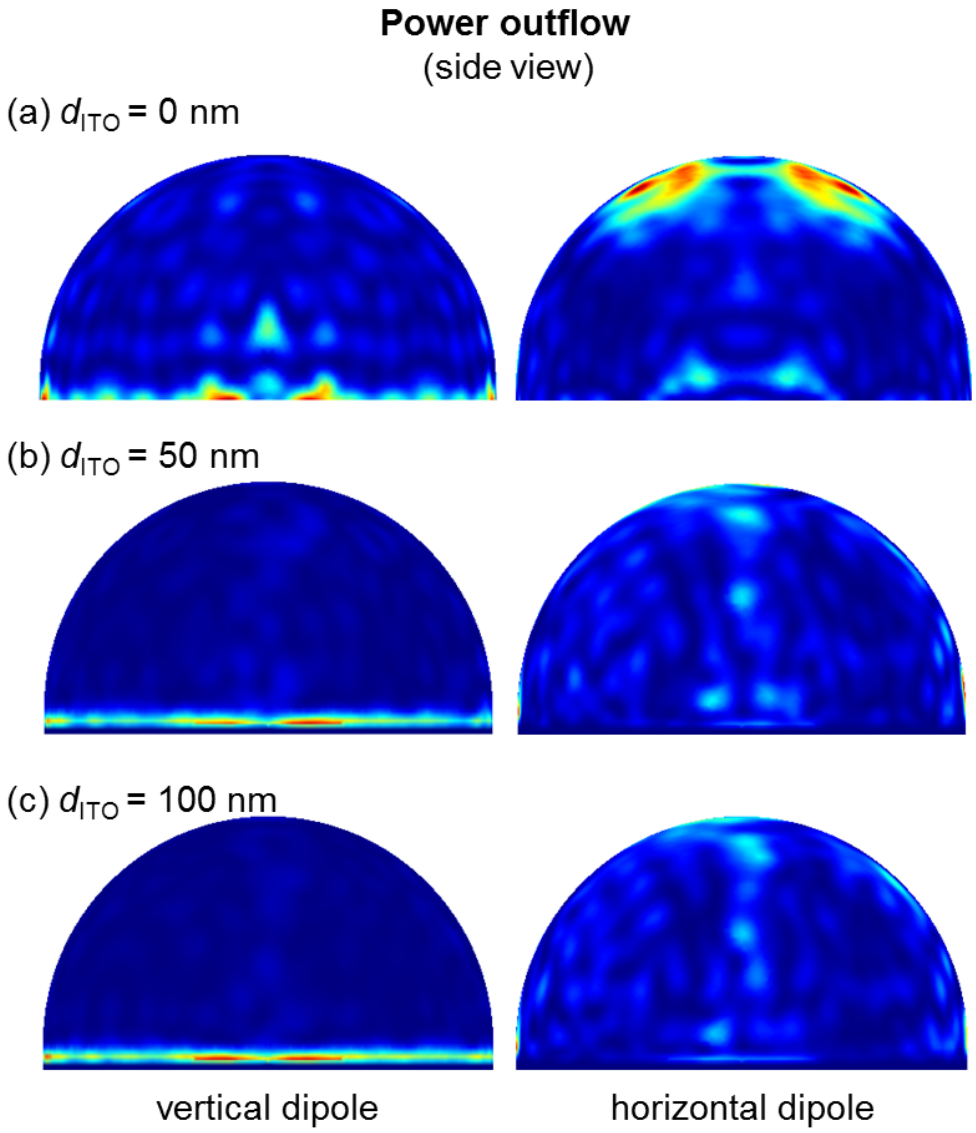

Figure 5.1: Side view of power outflow for a monolayer of $d = 300\,\text{nm}$ spheres and monolayer-ITO separations of (a) 0 nm, (b) 50 nm and (c) 100 nm. When the spheres are adjacent to the ITO, significant scattering is observed. As the distance is increased, light from the horizontal dipole is blocked and scattering is reduced.

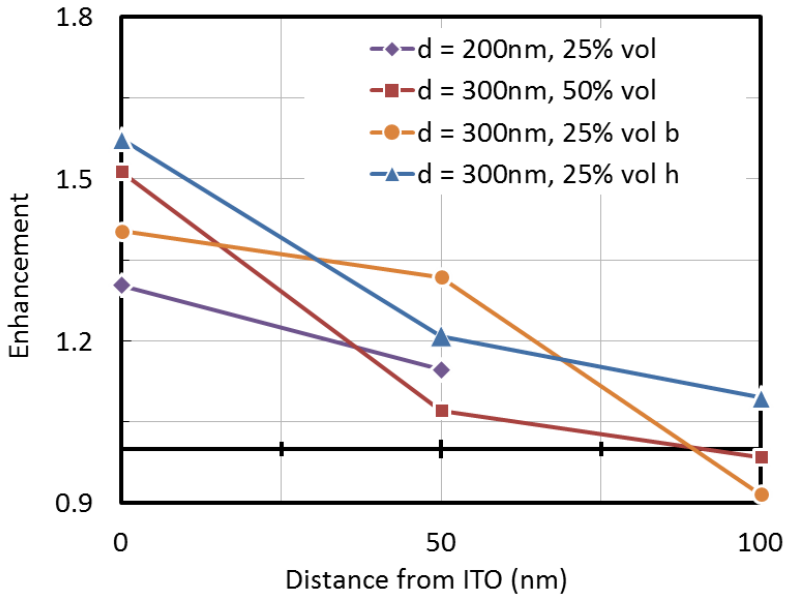

Figure 5.2: Plot of SQE enhancement for several configurations of the TiO_2 NP scattering layer as a function of distance from ITO. Labels b and h correspond to dipoles located beneath a sphere and below a space between spheres, respectively, as depicted in Fig. 5.5

5.4 Refractive index dependence

It is clear that the enhanced outcoupling occurs when the guided mode encounters regions of abrupt refractive index contrast causing some of the scattered light to couple to substrate or radiative modes. In §5.3, we found that due to the exponentially decaying field outside of the waveguide this interaction is reduced with distance away from the core. However, if the refractive index of the scattering film matrix is close to that of ITO, the core of the waveguide will be extended to include the scattering NPs as in Refs. [1, 3]. On the other hand, this effectively thicker waveguide may support additional modes trapping more light. In this section, we investigate this balance by varying the refractive indices of both the scattering film and the nanoparticles. For these simulations, the square lattice of spheres with $d = 300\,\text{nm}$ and $p = 300\,\text{nm}$ is used. The thickness of the host layer is taken to be the same as the sphere diameter.

As the host layer refractive index is varied from $n_{host} = 1.5$ to $n_{host} = 2.0$ for a

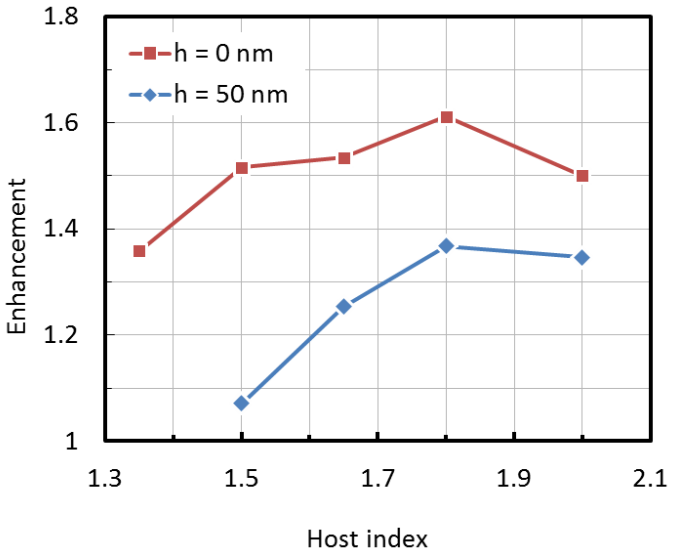

Figure 5.3: Outcoupling enhancement for a monolayer of scattering nano-spheres ($d = 300\,\text{nm}$, $p = d$, $n_{sphere} = 2.6$) as a function of host layer refractive index for sphere-ITO separations of 0 and 50 nm.

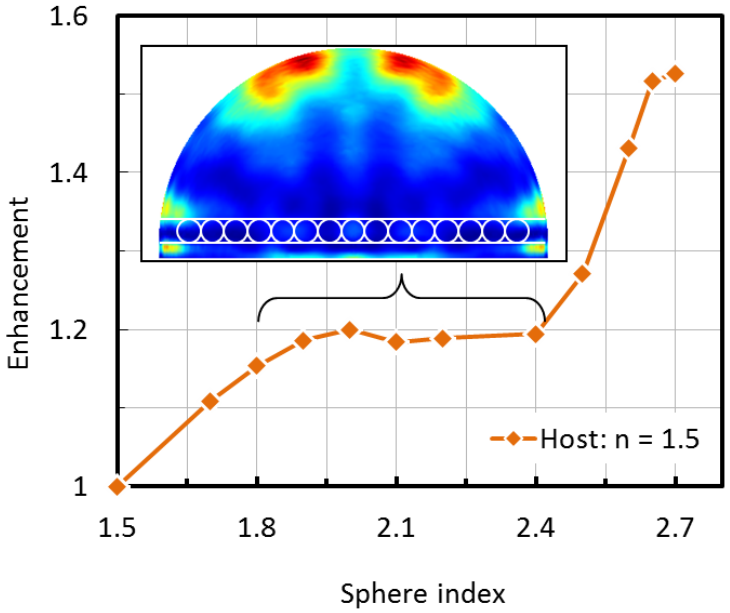

Figure 5.4: Outcoupling enhancement for a monolayer of scattering nano-spheres ($d = 300\,\text{nm}$, $p = d$, $n_{host} = 1.5$) adjacent to the ITO as a function of nano-sphere refractive index. The inset shows the power outflow for $n_{sphere} = 1.8$. The dipole orientation is horizontal (normal to the page). Significant waveguiding is observed even for the horizontal dipole when the sphere index is close to that of the waveguide core reducing the performance compared to high-contrast configurations.

monolayer adjacent to the ITO (Fig. 5.3), little variation in outcoupling is observed. If the host index is decreased to $n_{host} = 1.35$, below that of the substrate, the outcoupling is reduced as the evanescent fields are compressed towards the waveguide core. On the other hand, if the lattice is moved 50 nm away from the ITO, increasing the host refractive produces up to 37 % added outcoupling at $n_{host} = 1.8$. As the host index is increased beyond that of the waveguide core, the enhancement saturates. Evidently, when the spheres are in contact with the waveguide, the coupling to evanescent modes is quite strong and expanding the optical field by increasing the host layer index has negligible effect on outcoupling. For the poorly-coupled distant spheres, the extended field aids in outcoupling; however, the overall effect is not as great as for the ITO-adjacent monolayer. This is likely due to the increased number of available waveguide modes and reduced index contrast between spheres and host.

To directly see the impact of the index contrast, we simulate the monolayer with n_{host} fixed at 1.5 and vary the refractive index of the spheres (Fig. 5.4). The outcoupling is highest when the index difference between host and spheres is maximized, and lowest when their indices match. Rather than observing a monotonic improvement as a function of sphere index, we observe a plateau in the $n_{sphere} = 1.8-2.4$ region. This is attributed to partial waveguiding in the spheres themselves when the refractive index is similar to that of the ITO. This is apparent in the inset of Fig. 5.4 where a significant amount of light is seen directly above and below the monolayer near the edge of the simulation domain. Indeed, even when there is good index contrast between the spheres and both the host layer and anode, a significant amount of light is scattered into shallow angle substrate modes that may be difficult to extract at the air interface. It is expected that the sphere-guiding effect can be reduced with a sparse packing of scattering NPs. Additional layers or vertical disorder in the sphere position could aid in redirecting the shallowly scattered light towards the substrate normal.

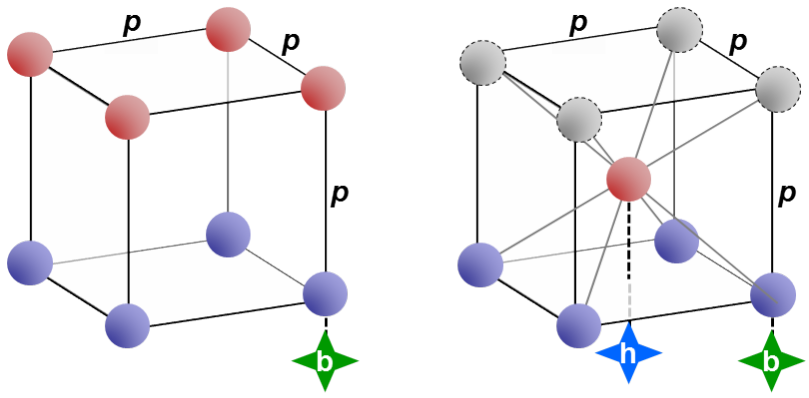

(a) *SC* (b) *bcc*

Figure 5.5: Simulated multilayer geometries consist of the first (blue) and second (red) planes of (a) simple cubic (*SC*) and (b) body-centered cubic (*bcc*) Bravais lattices. Grey positions are shown for reference. For the *bcc* lattice, the dipole was positioned below a sphere in the first monolayer (position *b*) or below one in the second monolayer (position *h*).

5.5 Sphere spacing, dipole position and multiple layers

Although the waveguide mode only extends a short distance into the substrate, the facile fabrication methods based on spin-coating can produce much thicker scattering films (e.g. $\sim$2 μm in Ref. [2]). Since the scattering NPs are randomly distributed throughout the film, it is important to consider the interplay of spheres at different distances from the waveguide. In §5.3, we saw that, in general, distant spheres tend to trap light. On the other hand, the added disorder and increased spacing of thick sparse films may be beneficial in reducing sphere-guided light. In this section we model single and double monolayers of spheres. We use dense (i.e. spheres in contact with nearest neighbors) and sparse monolayers arranged such that they form two planes of cubic Bravais lattices, namely, simple cubic (*SC*) and body-centered cubic (*bcc*) (Fig. 5.5). The results are summarized in Table 5.2.

Noting that a single plane of either *SC* or *bcc* is simply a square packing as used previously, we first compare the outcoupling dependence on sphere spacing. Positioning

Table 5.2: Outcoupling enhancement for various arrangements of single- and double-layer scattering films using $n_{host} = 1.5$ and $n_{sphere} = 2.6$. The lattice type and dipole positions are shown in Fig. 5.5.

Sphere diameter (nm)	Lattice	Lattice constant (nm)	Dipole position	Single-layer enhancement	Double-layer enhancement
200	*bcc*	200	*b*	1.24	1.47
200	*bcc*	282	*b*	1.30	1.37
200	*bcc*	282	*h*	1.30	1.32
300	*SC*	300	*b*	1.51	1.41
300	*bcc*	424	*b*	1.40	
300	*bcc*	424	*h*	1.57	1.12

the dipole below a sphere (position *b*), the enhancement for a 50 % density monolayer of $d = 300$ nm spheres is fairly high at 1.51; if we reduce the density by a factor of 2, the outcoupling is decreased to 1.4. However, if we move the dipole beneath the now-open region (position *h*), an enhancement of 1.57 is achieved. The power flow for both dipole positions is shown in Fig. 5.6. It is apparent that in both positions, there is significant scattering away from the forward direction for emission originating from the horizontal dipole. For spheres with a smaller 200 nm diameter, the initial improvement of 1.24 using a dense monolayer is increased to 1.3 for a sparse monolayer, regardless of dipole position. Clearly, a balance must be achieved between scattering light in the waveguide and blocking the direct-to-substrate emission: although the smaller spheres appear to block less light as evidenced by the improvement in both dipole positions in the sparse monolayer, they also scatter less total light compared to either the dense or sparse films of the larger NPs.

Next, we add second monolayers as indicated in Fig. 5.5. For dipoles centered under a sphere, a second monolayer in the *bcc* configuration shows a modest improvement. For example, the enhancement using a dense lattice of small spheres is increased from 1.24 to 1.47, and for a sparse lattice the increase is from 1.3 to 1.37. Likely, the light scattered into angles nearly parallel to the interface by the blocking sphere above the dipole

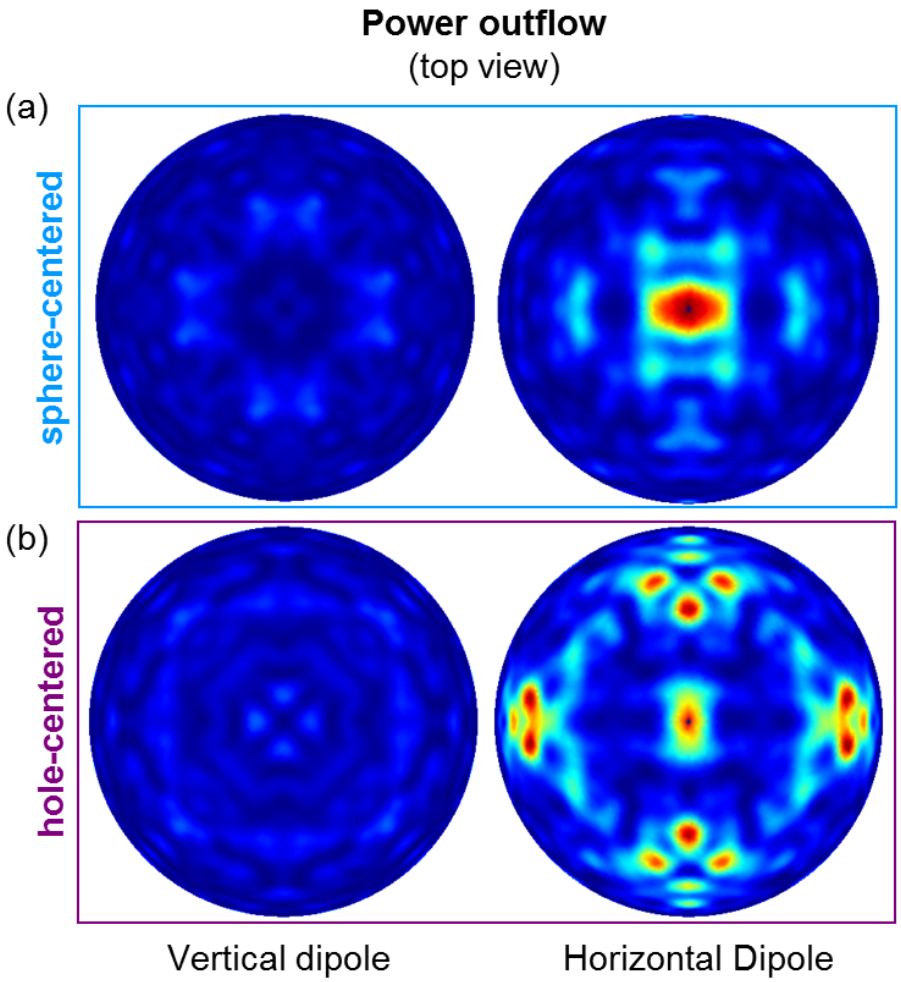

Figure 5.6: Power outflow for a single monolayer with $d = 300\,\text{nm}$ and $p = 424\,\text{nm}$ with a source dipole positioned (a) under a sphere (position b) and (b) under the space between spheres (position h). Significant scattering away from the normal direction is observed for emission originating from the horizontal dipole.

(clearly seen in Fig. 5.1) is then redirected by the particles of the second monolayer. Unfortunately, this effect is counterbalanced by the decrease in outcoupling enhancement when the dipole is located beneath a gap in the first monolayer. In this arrangement, the high enhancement of a single sparse array of large spheres is reduced from 1.57 to merely 1.12 as the second monolayer acts to block the direct emission without adding significant scattering. This situation parallels the case of a single monolayer that is removed from the ITO and which traps light that would otherwise be directly or indirectly coupled to the substrate. Finally, a simple cubic lattice with the second plane of spheres aligned exactly with the first also yields no benefit as the enhancement is reduced from 1.51 to 1.41. Again, the second monolayer cannot efficiently scatter the waveguided modes while potentially blocking direct emission or acting as a waveguiding layer.

5.6 Discussion

We began our analysis based on the premise of an outcoupling solution for waveguide modes that, being placed between the device and substrate, would not detrimentally impact OLED fabrication or create roughness and non-uniformities impacting the electrical performance. Because the scattering nano-particle film is parametrically more complex than the embedded grid discussed in Chapter III, we have not exhaustively pursued an optimum geometric or optical configuration. Moreover, the limited lateral extent of our simulation domain suggests that any absolute enhancement calculated may be somewhat underestimated since the propagation lengths before full absorption for waveguide and SP modes are roughly 50 μm and 7 μm, respectively [2]. Nonetheless, we can generally identify the effects introduced by our idealized planar scattering layer as falling into three main categories:

1. Interaction of scattering nano-particle with waveguide/SP modes.

2. Scattering of the direct- or nearly direct-to-substrate emission (particularly from

the in-plane dipole).

3. Waveguiding by the scattering layer host and/or scattering particles.

Of these, only (1) is unambiguously advantageous as a means of improving efficiency. Since the interaction is with light that in a conventional OLED is already hopelessly trapped, at worst the effect is null. Predictably, we observe that maximum enhancement is produced when there is high degree of simultaneous refractive index contrast between the scattering particles, the waveguide and the substrate. Likewise, as the scattering particles are moved farther from the waveguide core, the interaction with the evanescent field is reduced and the outcoupling rapidly decreases.

Effect (2) is largely detrimental, since some of the light already outcoupled in a conventional device may be reflected back toward the lossy metal cathode or scattered into angles nearly parallel to the waveguide, potentially leading to effect (3) which is wholly undesirable. Evidently, increased distance from the ITO *also* leads to increased trapping due to (2), adding to the problem of reduced waveguide mode scattering. The obvious consequence is that thick scattering films with low volume loading such as those used in Ref. [2] are unlikely to significantly outcouple light trapped in the waveguide due to the on-average large distance of scatterers from the anode. This also explains the reduction in outcoupling predicted using FDTD simulations in Ref. [3] when a relatively thick neat planarizing layer was inserted between the ITO and the scattering film. Unfortunately, corrective actions one might pursue in order to compensate for the reduced coupling in (1), e.g. increasing the host index, are likely to result in detrimental waveguiding effects (3). In turn, additional monolayers that may mitigate effect (3), cause more light trapping (2). In general, it appears that achieving a delicate balance between these three competing effects would require extensive optimization and precise fabrication.

Overall, it seems unlikely that the methods employed experimentally thus far to produce such scattering nano-particle films can provide the necessary degree of control

to ensure efficient waveguide outcoupling. Moreover, the films produced by the spin-coating method in Ref. [1] and the sol-gel method in Ref. [3] retain a significant amount of roughness and non-uniformity. Although this may indeed produce some scattering from the waveguide, more likely the impact is on glass mode outcoupling and electrical performance of the device. For example, control and scattering devices in Ref. [1] have dissimilar EQE roll-off behavior, consistent with their vastly different current-density–voltage (J-V) characteristics. Clearly, the non-uniform scattering films are impacting the electrical properties of the OLED and leading to the claimed "fourfold power efficiency improvement" in the roll-off region. Since the control EQE quickly drops in this range, device comparisons are largely distorted here due to division by small numbers. A more meaningful enhancement can be calculated in the low-current region (where EQE is flat and optical effects are dominant) to be < 2. This is well within the improvement achievable by outcoupling only glass modes with e.g. microlenses (see Table 5.1).

Similarly, in Ref. [3], the rough device with the scattering layer shows almost no improvement in EQE but a factor of 1.5 increase in power efficiency. This indicates that the effects are primarily electrical and not optical in nature as the latter produces concomitant enhancement in both efficiencies. This is indeed observed when a low-index planarizing layer is inserted between the anode and the scattering layer: both EQE and PE are doubled. Since a direct measurement of SQE is not reported, it is not possible to unambiguously determine whether the enhancement is from waveguide outcoupling; however, the improvement with the planarizing layer present contradicts both the presented FDTD simulations and our full-wave modeling of the waveguide region. On the other hand, the optically non-uniform film can scatter light trapped by TIR at the glass/air interface allowing it to escape after a few reflections [7]. Undoubtedly, the re-scattering of TIR-trapped light is also the main effect in Ref. [2]. Using both the sparse 2 μm-thick scattering film and a hemispherical lens macro-extractor, a factor of 2.13 improvement in EQE is achieved. Although a reference device with only the

macro-extractor is not provided, we can conservatively estimate that the hemisphere functions as well as using an IML to outcouple all glass modes i.e. doubling the *EQE*. Based on this, the incremental outcoupling from waveguide modes is just 7 %.

5.7 Conclusion

In this chapter, we numerically analyzed an outcoupling method based on diffuse scattering films consisting of nanoparticles embedded in a host layer. Based on our simulations, we conclude that this structure can extract light from the waveguide provided the nanoparticles are positioned close enough to the high-index region of the OLED to significantly overlap with the evanescent fields of the loosely bound waveguide modes. Furthermore, a high refractive index contrast is necessary for efficient scattering. Provided the particle size, volume loading and film thickness are optimized, the OLED *EQE* can be enhanced while maintaining a nearly planar surface for subsequent OLED deposition. However, due to the constraints of competing optical effects and limitations of the simple self-assembly fabrication methods, we find that recent implementations of this technique [1–3] observed efficiency improvements unrelated to waveguide outcoupling. Namely, substrate mode outcoupling and/or modified electrical properties of the resulting devices are largely responsible for the reported improvements. In the future, applying deterministic fabrication techniques will be necessary to fully reap the benefit of outcoupling by nanoparticle scattering films without impacting the active regions of the OLED.

CHAPTER V

Bibliography

[1] C.-H. Chang, K.-Y. Chang, Y.-J. Lo, S.-J. Chang, and H.-H. Chang, *Org. Electron.* **13**, 1073 (2012).

[2] H.-W. Chang, J. Lee, S. Hofmann, Y. H. Kim, et al., *J. Appl. Phys* **113**, 204502 (2013).

[3] J. Lee, Y. Y. Kwon, E.-H. Choi, J. Park, H. Yoon, and H. Kim, *Opt. Express* **22**, A705 (2014).

[4] Y. Sun and S. R. Forrest, *Nat. Photon.* **2**, 483 (2008).

[5] M. Slootsky and S. R. Forrest, *Opt. Lett.* **35**, 1052 (2010).

[6] *COMSOL Multiphysics*, ver. 3.5a (Comsol Inc., Stockholm, Sweden, 2009).

[7] T. Yamasaki, K. Sumioka, and T. Tsutsui, *Appl. Phys. Lett.* **76**, 1243 (2000).

CHAPTER VI

Waveguide light outcoupling using a sub-ITO grid

6.1 Introduction

In previous chapters, we demonstrated how a micron-scale grid embedded in the active layers of an OLED can be used to effectively redirect light from the waveguide modes to the substrate and eventually into the forward viewing direction. The grid structure affords us precise control over the geometric parameters and allows straightforward optimization both numerically and experimentally. On the other hand, in Chapter V, we evaluated the potential of using a nano-particle scattering film placed externally to the waveguide to prevent detrimentally affecting electrical performance. Full-wave simulations demonstrated that in order to achieve maximum benefit, the nano-particles must be in intimate contact with the ITO, a constraint not easily satisfied with typical fabrication methods for the films [1–3]. Additionally, the outcoupling enhancement is sensitive to the precise geometry which cannot be easily controlled. Here, we endeavor to unite the best traits of the LIG and the scattering film by designing a grid embedded in a thin planar layer directly between the substrate and ITO.

6.2 Full-wave simulations

To understand key parameters of the sub-ITO grid, we model the structure using COMSOL 4.3b [4]. The general methodology is the same as that in previous chapters with slight alterations to increase computational performance. The simulation domain,

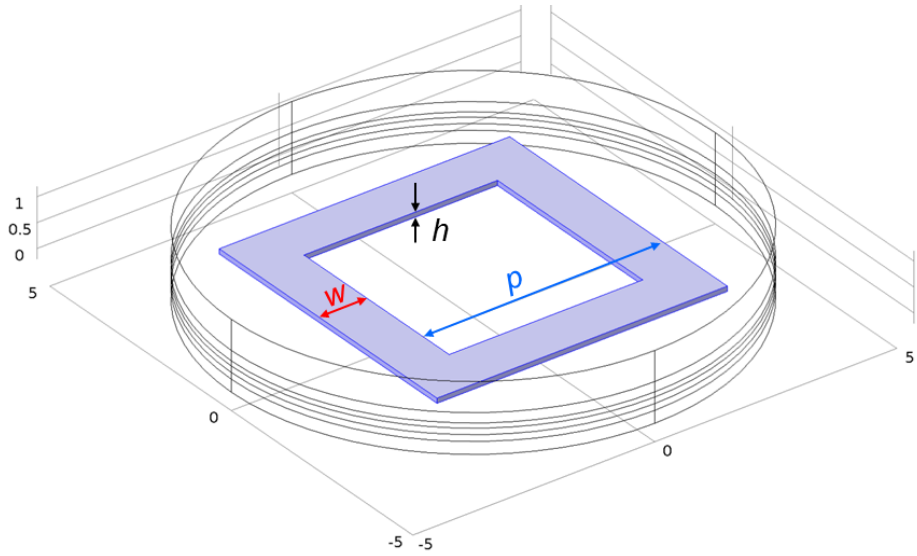

Figure 6.1: Simulation domain for the sub-ITO grid structure. Units are µm.

shown in Fig. 6.1, is cylindrical with a diameter of 10 µm and a height of roughly 1.5 µm. The high-index region consists of 100 nm-thick lossless layers of organic ($n_{org} = 1.75$) and ITO ($n_{ITO} = 1.8$). An impedance boundary condition is used for the Al cathode with the same Lorentz-Drude parameters as before [5]. The grid is embedded in a film with thickness equal to its height and positioned between ITO and the glass substrate. The full electro-magnetic fields in the model are solved for directly with the parallel direct sparse solver (PARDISO) using a workstation with two 10-core Intel Xeon processors (E5-2660v2) and 128 GB of memory.

6.2.1 Refractive index dependence

Using a single unit cell of a square grid with dimensions given by $p = 5\,\mu m$, $w = 1\,\mu m$ and $h = 100\,nm$, the dependence of the refractive index of both grid material and surrounding film on outcoupling is investigated. The grid refractive index is varied between 1 and 2 for film indices in the range of 1.2–2.2. The results are most conveniently visualized in terms of the index contrast, $\Delta n = n_{film} - n_{grid}$ (Fig. 6.2). Unsurprisingly, the outcoupling from the waveguide is maximized for large Δn. Around the zero point

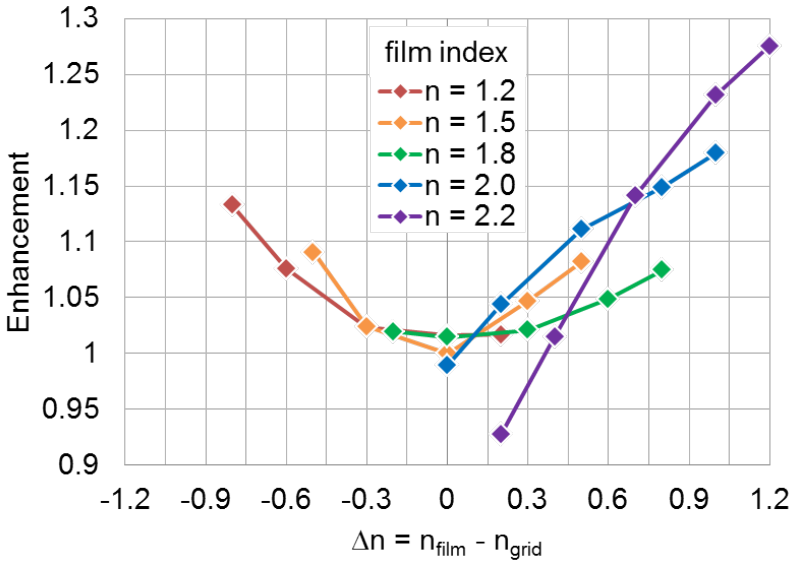

Figure 6.2: Outcoupling enhancement as a function of index contrast $\Delta n = n_{film} - n_{grid}$ for $p = 5\,\mu m$, $w = 1\,\mu m$ and $h = 100\,nm$.

(corresponding to neat films with no grid), we observe nearly symmetric outcoupling enhancement. The negligible degree of asymmetry arises from the different dimensions of the low- and high-index regions. Unlike the LIG where emission is strictly from the region between the grid lines, excitons in this structure can recombine anywhere relative to the grid. Therefore, it is fortuitous that the scattering effect is roughly equal regardless from which side of the interface (laterally) the light originates. For high-index films, the competition between micro-cavity effects and scattering of guided light is evident. For example, if the contrast is reduced in a film with $n_{film} = 2.2$ such that there is no scattering, the outcoupling falls to merely 93 % that of the control device. Somewhat surprisingly, the maximum improvement is also achieved with the same film and $n_{grid} = 1.0$. This suggests that the OLED stack must be optimized in conjunction with the sub-ITO grid i.e. the optically optimal organic layer thicknesses may not be the same as for a device on a conventional substrate.

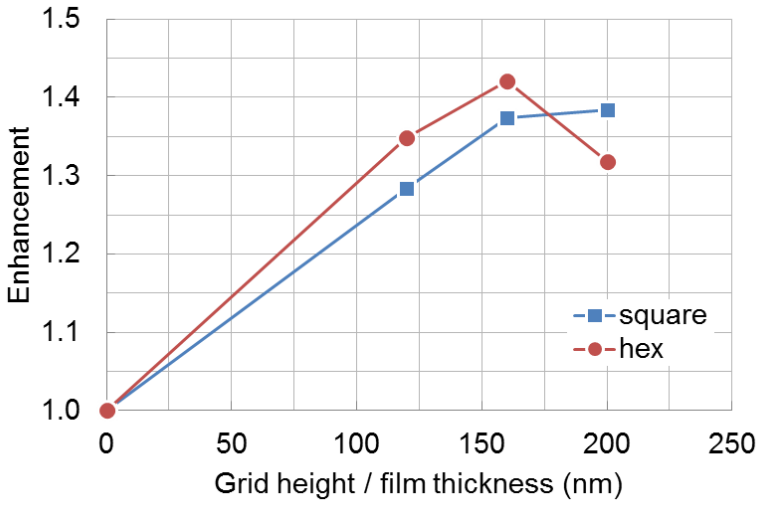

Figure 6.3: Outcoupling dependence on grid height for square and hexagonal unit cells with $p = 4\,\mu\text{m}$, $w = 1\,\mu\text{m}$, $n_{grid} = 1.5$ and $n_{film} = 2.2$. The high-index film thickness is taken to be the same as the grid height.

6.2.2 Geometry dependence

Since the grid is no longer embedded in the active layer, its height is not restricted by the thickness of the organics or the potential electrical issues associated with the resulting step edge. Using conventional vacuum deposition techniques, this parameter can be easily and precisely controlled and gives us an additional pathway for optimizing optical performance. Outcoupling dependence on height of square and hexagonal grids with $p = 4\,\mu\text{m}$, $w = 1\,\mu\text{m}$, $n_{grid} = 1.5$ and $n_{film} = 2.2$ is shown in Fig. 6.3. The waveguide extraction enhancement is seen to increase up to $h = 160\,\text{nm}$, beyond which, it saturates. Since the refractive index of the host film is higher than that of the substrate, the evanescent field penetration depth is reduced, and, evidently, less than 200 nm of low-index material is sufficient for full interaction with the guided modes. The slight advantage of the hexagonal unit cell here is due to the on-average shorter lateral distance between the source dipole and the grid line.

Using a square grid with a near-optimum height ($h = 150\,\text{nm}$), embedded in an equal thickness film with $n_{film} = 2.2$, we examine the importance of grid line width and period

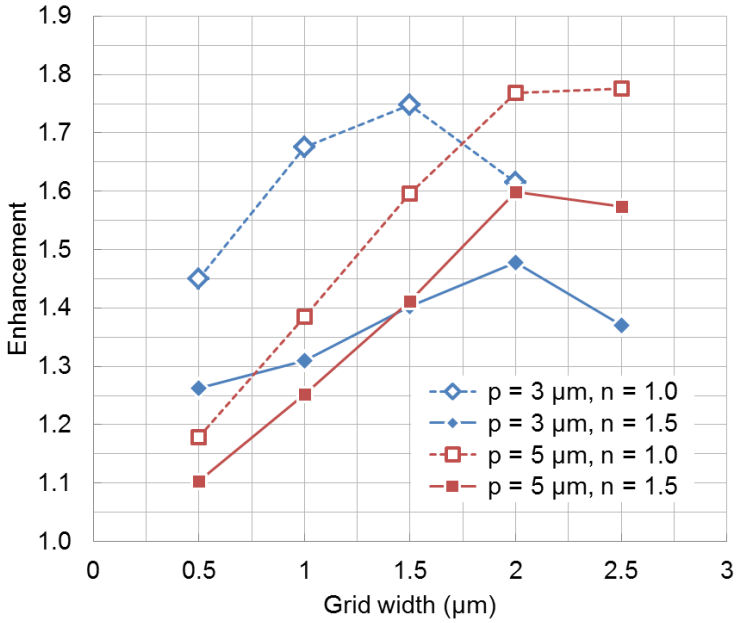

Figure 6.4: Outcoupling dependence on grid width for square unit cells with $p = 3$ (diamonds) and 5 μm (squares), $n_{grid} = 1$ (open symbols) and 1.5 (filled symbols), and $n_{film} = 2.2$.

for two different refractive index materials ($n_{grid} = 1$ and 1.5). The width is varied within 0.5–2.5 μm range for periods of 3 and 5 μm. The results are plotted in Fig. 6.4. For all choices of period and width, reducing the refractive index increases outcoupling consistent with previous simulations. As the width of the low index region is increased, light extraction initially goes up; however, for all four grids, the improvement peaks and begins to decline near the $w = p/2$ point. As discussed in §6.2.1, the scattering effect is nearly symmetric for a given index contrast regardless of whether the grid is the low- or high-index material. Thus, it is reasonable for the optimum dimensions of these regions to be roughly equal.

Initially, for small widths, the smaller period grids outperform their $p = 5$ μm counterparts; however, since the larger period unit cell can accommodate a wider grid line, the large cells take the lead as the small ones begin to roll-off. Presumably, one must balance the added scattering of a wide grid with large spacing against absorption of waveguided light by the device. This is further complicated by the fact that, here, more

than one period may be contributing to outcoupling. Nonetheless, even a single cell of a grid with $n_{grid} = 1$, $p = 5\,\mu m$ and $w = 2\,\mu m$ embedded in a host film with $n_{film} = 2.2$ is predicted to produce an astounding 75 % outcoupling enhancement.

6.3 Experimental methods

6.3.1 Air grid fabrication

Figure 6.5 demonstrates the fabrication process for a sub-ITO air grid consisting of a patterned 170–210 nm thick TiO_2 film. The TiO_2 was deposited by e-beam evaporation onto a 4" Si carrier wafer pre-coated with a lift-off resist (LOR) sacrificial layer (MicroChem LOR 3A). Photoresist (PR) (Microposit S1805) was subsequently spin-coated onto the TiO_2 film. The desired grid pattern was photolithographically defined and the photoresist (PR) was developed using AZ726 in a CEE puddle developer tool for 60 s. The TiO_2 was partially etched to a depth of 150–165 nm by a chlorine-based inductively-coupled plasma (LAM 9400). After etching, the PR was stripped using an O_2 plasma at 200 W (YES plasma tool).

Prior to bonding, the carrier wafer with the patterned film was megasonically cleaned using DI water (SUSS MicroTec CL200) to remove any residual particulates while a glass wafer was cleaned using an RCA1 solution in the same tool. Both the carrier and glass wafers were subsequently treated with O_2 plasma to make them hydrophilic. A sodium silicate solution (Sigma-Aldrich SKU#338443) diluted to 2 % by volume with DI water was spin-coated onto the glass wafer following the procedure in Ref. [6]. Immediately, the glass and carrier wafers were brought into contact and pressure was applied by hand. Subsequently, the combined wafers were cured at 20 MPa and 90 °C for 1 h and left to cool under pressure overnight.

The bonded wafers were diced into 15 mm × 15 mm substrates which were soaked in N-Methyl-2-pyrrolidone (NMP) at 80 °C for 24–30 h to dissolve the sacrificial LOR

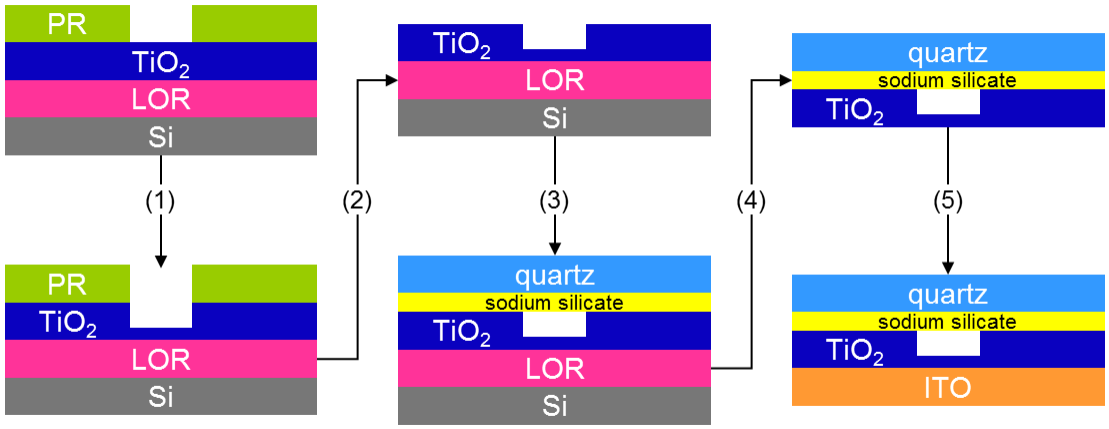

Figure 6.5: Fabrication flow for an air grid. A TiO_2 film coated with lithographically patterned PR is prepared on a sacrificial layer of lift-off resist (LOR). (1) The TiO_2 is partially etched and (2) the PR is stripped off. (3) The patterned film is bonded to quartz using a sodium silicate solution. (4) The sacrificial LOR layer is dissolved separating the grid layer from the carrier wafer. (5) ITO (and the OLED) is deposited onto the grid.

layer separating the TiO_2 film from the Si carrier. Figure 6.7(a) shows the atomic force microscopy (AFM) image of the transferred TiO_2 film with square embedded air grid. The surface is quite planar and root-mean-square roughness is below 1 nm. A continuous grid was found to form protrusions at the intersections of the grid lines after a subsequent ITO annealing step. Thus, squares of TiO_2 were inserted into the pattern, shown in Fig. 6.8(a), to help pin the surface.

6.3.2 Buried grid fabrication

Figure 6.6 shows the process flow for fabricating a SiO_2 grid embedded in a planar layer of TiO_2 placed between the ITO and the substrate. A fused silica substrate was patterned using lithographically defined bi-layer photoresist (MicroChem LOR 3A and Shipley SPR220-3.0) as an etch mask. Square and hexagonal grids, shown in Fig. 6.8, were fabricated. The bi-layer PR was used to produce an undercut profile during developing. The etching was performed using an inductively-coupled CF_4:CHF_3 plasma (LAM 9400). Without removing the PR, TiO_2 was deposited at 2 Å/s using e-beam evaporation

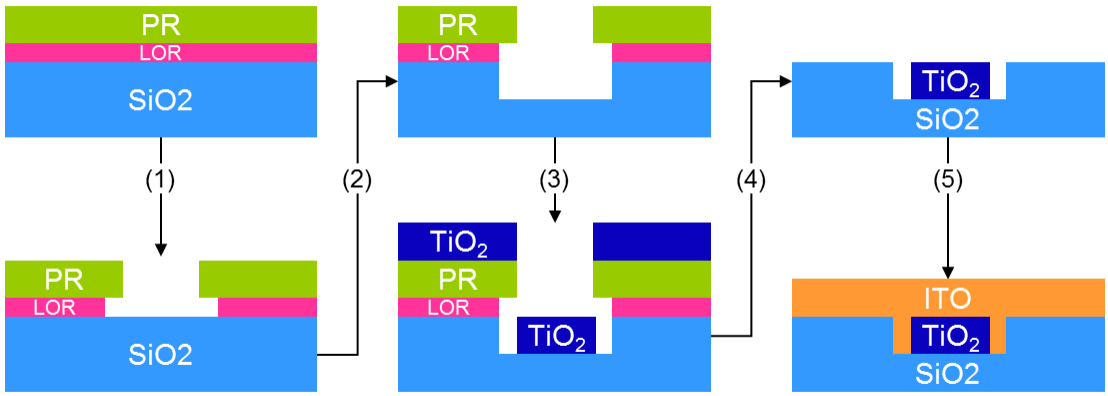

Figure 6.6: Fabrication flow for a buried grid. Bi-layer resist is prepared on a fused silica substrate. (1) The PR is lithographically patterned and developed producing an undercut profile. (2) The SiO_2 layer is etched using plasma. (3) Without removing PR, TiO_2 is deposited filling in the etched region. (4) The PR is removed using hot Remover PG to dissolve the lift-off resist (LOR); the remaining surface is nearly planar. (5) ITO is deposited onto the grid layer.

with a thickness equal to the etch depth, thus evenly filling in the openings in the SiO_2 grid. The excess TiO_2 was lifted-off by dissolving the LOR in RemoverPG at 70 °C for 2 h. An AFM image of the resulting surface is shown in Fig. 6.7(b). After re-fill with TiO_2, the step-height between the grid and surrounding material is approximately 5 nm and the surface roughness is 1.1 nm. It is important to deposit TiO_2 as nearly to normal incidence as possible to prevent shadowing and sidewall deposition on the PR which result in the slight troughs and peaks visible on either side of the grid.

6.3.3 Device growth and testing

After grid preparation, 70 nm ITO was sputtered onto the grid layers at a rate of 0.6 Å/s followed by annealing for 2 h at 250 °C and 1×10^{-6} mTorr . Control substrates consisted of ITO deposited directly onto pre-cleaned quartz and onto neat TiO_2 films with equivalent thickness to the grid layers. The ITO was subsequently annealed in vacuum at 250 °C. The ITO-coated substrates were cleaned using acetone, hot isopropanol and UV-ozone immediately prior to OLED deposition. Sonication was used during the acetone

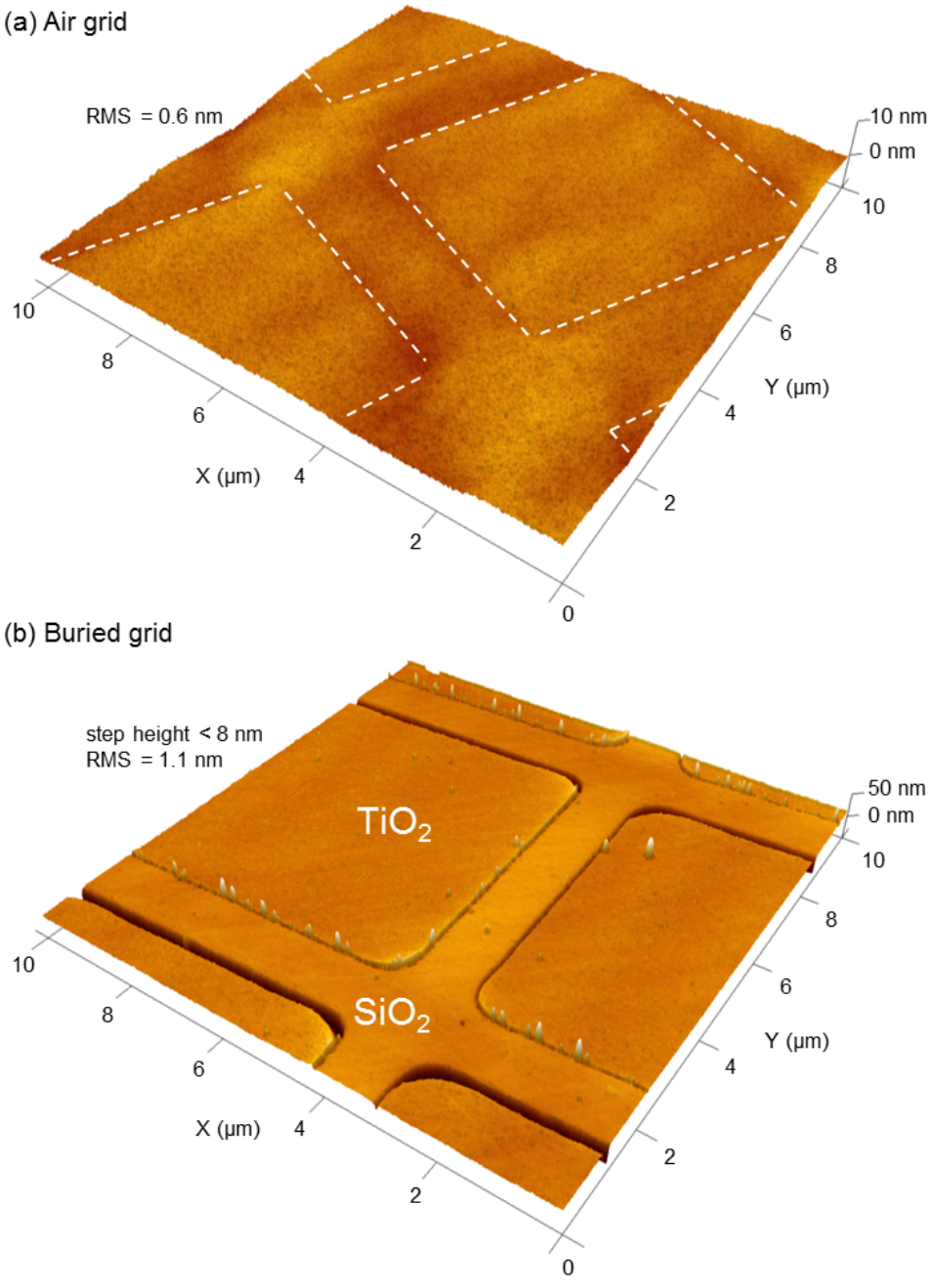

Figure 6.7: Atomic force microscope images of the surface of (a) an air grid embedded in TiO_2 and (b) a grid of SiO_2 filled with TiO_2.

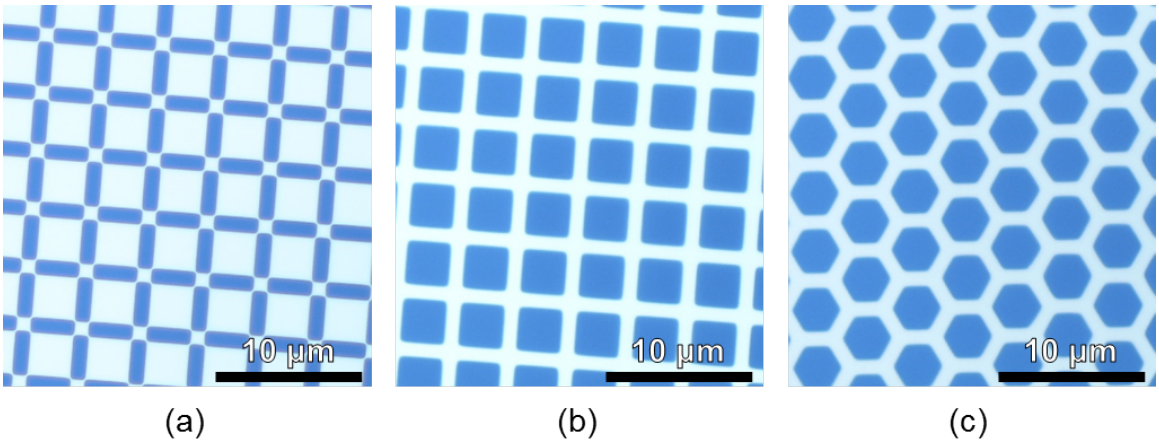

Figure 6.8: Micrographs of the (a) square air grid, (b) square SiO_2 and (c) hexagonal SiO_2 grids embedded in TiO_2 films. In (a), the air voids etched into a TiO_2film are the dark blue regions; in (b) and (c), the light color regions are SiO_2.

step for control and buried grid substrates; however, the void grid was found to be too fragile for sonication.

Organic layers and cathode were deposited using VTE at a rate of 0.5–2 Å/s. The green OLED structure is as follows: ITO/20 Å MoO_3/ 400 Å CBP/ 150 Å 15 % $Ir(ppy)_3$:CBP/ 650 Å TPBI/ 8 Å LiF/ 100 nm Al. Since we expect the full effect of waveguide outcoupling to be observed only with efficient substrate light extraction, the J-V-L characteristics of the devices were collected with IML using the procedure in §4.3 to measure the substrate quantum efficiency (SQE). The angular intensity profile was measured using a goniometer with 5° resolution. Three grid geometries with $p = 4\,\mu m$, $w = 1\,\mu m$ embedded in TiO_2 films ($n_{film} = 2.2$) were used for OLED growth:

1. Air grid: $3\,\mu m \times 3\,\mu m$ and $1\,\mu m \times 1\,\mu m$ squares of TiO_2 separated by 1 µm-wide air gaps and covered with a thin neat layer, shown in Fig. 6.8(a). The TiO_2 thickness is 200 nm while the air grid height is approximately 160 nm.

2. Silica square buried grid: $3\,\mu m \times 3\,\mu m$ squares of TiO_2 separated by 1 µm-wide SiO_2 grid lines ($n_{grid} = 1.45$). Fig. 6.8(b).

3. Silica hexagonal buried grid: hexagonal regions 3 μm across and filled with TiO_2, separated by 1 μm-wide SiO_2 grid lines. Fig. 6.8(c).

The measured performance of preliminary devices on different substrates is shown in Fig. 6.9. The control device is a relatively efficient phosphorescent architecture with a peak *SQE* of 35 % (a factor of 2.05 higher than its *EQE* due to the IML). The largest improvement is achieved using the hexagonal SiO_2 grid, reaching an *SQE* of 41 % or 1.17 enhancement in waveguide outcoupling. Both the square buried grid and air grid reach a peak *SQE* of just 36 %. While the hexagonal grid device has nearly the same efficiency roll-off behavior as the control device, the air and square grids behave differently. The device on the air grid shows three orders of magnitude higher current prior to turn-on. This leakage causes the quantum efficiency to be much lower for $J < 0.1$ mA/cm than the other devices. At higher injection, the performance of the air grid begins to match that of the hexagonal grid. The square silica grid, on the other hand, initially performs slightly better than the control, but begins to roll-off earlier. Both square and hexagonal buried grids show higher current at a given bias than the control.

The emission spectrum, shown in Fig. 6.10(a), is slightly red shifted for the SiO_2 grid devices compared to the conventional OLED. Since this device consists of two distinct weak-microcavities [7], a combination of their spectra is expected. The grid device redshift is less pronounced than that of an identical OLED grown on a substrate with a neat TiO_2 film of the same thickness as the grid layer. On the other hand, the air grid shows almost no spectral change. It appears that the emission from beneath the low-index grid-lines compensates that of the high-index TiO_2 regions. The angular emission of both control and grid devices is free from any distinct features, confirming that the grid does not act as a diffractive grating. As shown in Fig. 6.10, the scattering from the sub-ITO structure actually brings the angular emission profile closer to that of an ideal Lambertian.

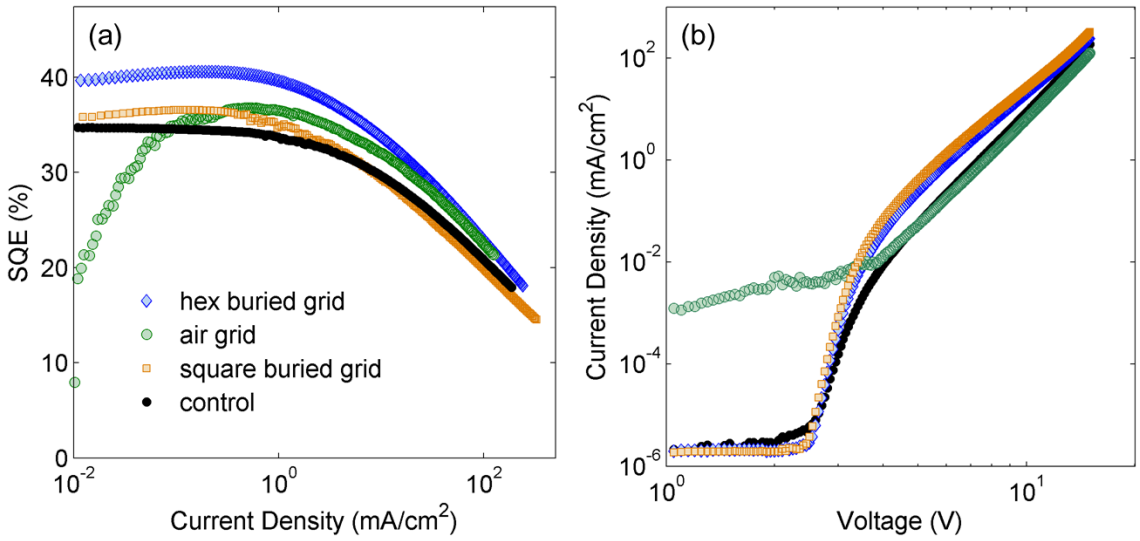

Figure 6.9: Measured (a) *SQE* and (b) *J-V* of OLEDs on the three sub-ITO grid geometries shown in Fig. 6.8.

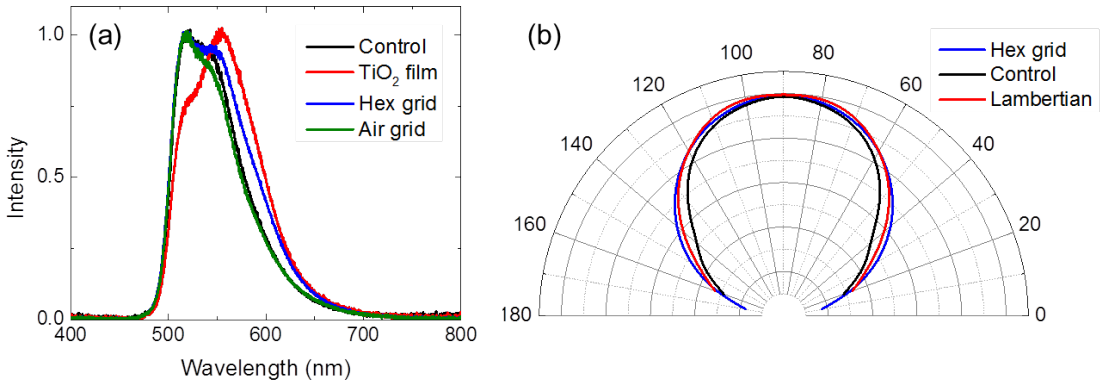

Figure 6.10: (a) Spectrally- and (b) angularly-resolved electroluminescence of devices on sub-ITO grid substrates compared against conventional devices.

6.4 Discussion and conclusions

Although full-wave simulations suggest that the sub-ITO structure can be effective at scattering light trapped in the waveguide, preliminary experimental results have only indicated a modest enhancement in outcoupling. For the best performing hexagonal grid, the improvement is approximately half of that predicted with our model. There is indication that the grid behaves as anticipated, for example, as we vary the thickness of the grid layer the resulting trend is that of Fig. 6.3 for both square and hexagonal silica structures, but the experimental outcoupling enhancement is significantly lower. Likely, the main culprit is excess leakage current formed by shunt paths in the device due to slight non-uniformities introduced by grid fabrication. In Fig. 6.7, both spikes and troughs can be observed near the SiO_2/TiO_2 boundaries. The gaps result from shadowing by the PR during the re-fill step, while the spikes are remnants of sidewall deposition. Using the less directional sputter-depositions may help avoid these defects. Alternatively, a planarizing layer (e.g. PEDOT:PSS) could be spin-coated onto the ITO.

While the air grid does not suffer from protrusions after transfer from the sacrificial layer, it was found that during ITO annealing the thin layer of TiO_2 above the voids can deform significantly, especially at the grid line intersections. Modifying the pattern to only partially solved this issue. Other geometries may be more advantageous, but it is likely that this may not be a viable method for designing structures with wide low- and high-index regions, predicted by simulations to outperform current geometries. In particular, the relatively large-period/large-width configuration is worth exploring experimentally as it both lends itself to easy fabrication and is predicted to be nearly twice as effective as the dimensions tested so far.

Overall, the outlook for developing well-controlled structures placed in close proximity to the OLED but outside the electrically active layers is promising. Numerical modeling indicates that an optimized geometry should perform at least as well as the embedded LIG without reduction of active area or other drawbacks. Despite some re-

maining issues in the microfabrication process, we have generally demonstrated two possible methods for creating such scattering layers with precise control of both dimension and optical parameters. In the first approach, micron-scale void channels formed separately on a sacrificial carrier and transferred to the OLED substrate prior to device growth allow for very large refractive index contrast advantageous for efficient scattering. The second technique leverages precision fabrication techniques to create in-plane patterns while retaining the desired high-quality smooth surface. Initial data for devices grown on substrates with these grids suggests that the technique is compatible with both display and lighting applications by providing largely spectrally- and angle-independent outcoupling.

CHAPTER VI

Bibliography

[1] C.-H. Chang, K.-Y. Chang, Y.-J. Lo, S.-J. Chang, and H.-H. Chang, *Org. Electron.* **13**, 1073 (2012).

[2] H.-W. Chang, J. Lee, S. Hofmann, Y. H. Kim, et al., *J. Appl. Phys* **113**, 204502 (2013).

[3] J. Lee, Y. Y. Kwon, E.-H. Choi, J. Park, H. Yoon, and H. Kim, *Opt. Express* **22**, A705 (2014).

[4] *COMSOL Multiphysics*, ver. 4.3b (Comsol Inc., Stockholm, Sweden, 2013).

[5] A. D. Rakić, A. B. Djurišić, J. M. Elazar, and M. L. Majewski, *Appl. Opt.* **37**, 5271 (1998).

[6] H. Wang, R. Foote, S. Jacobson, J. Schneibel, and J. Ramsey, *Sensor. Acutat. B-Chem.* **45**, 199 (1997).

[7] V. Bulović, V. B. Khalfin, G. Gu, P. E. Burrows, D. Z. Garbuzov, and S. R. Forrest, *Phys. Rev. B* **58**, 3730 (1998).

PART II

Strong light-matter coupling regime

CHAPTER VII

Microcavity exciton-polaritons

In §I, we focused on a regime where the field inside the device structure only serves to perturb the excited states and Fermi's golden rule can adequately predict radiative transition probability [1]. In this limit of weak coupling, the spontaneous emission rate of an exciton can be modified by changing the photonic density of states, for example, by placing the exciton in an optical microcavity [2]. This effect, first described by Purcell for radio frequencies [3], is embodied in the Purcell factor:

$$F_P = \frac{3}{4\pi^2}\left(\frac{\lambda}{n}\right)^3 \frac{Q}{V}, \tag{7.1}$$

where Q is the cavity quality factor, V is the mode volume and λ/n is the wavelength of light in the material. In OLEDs, which naturally form a weak microcavity, this effect can influence internal quantum efficiency by enhancing or suppressing the radiative recombination rate.

In the limit of strong light-matter interaction, however, one can no longer treat the excited state and the radiation field separately. Instead, one must consider the new normal modes of the coupled system that are formed from a mixture of photonic and excitonic components [4]. These new eigenstates are termed exciton-polaritons. Other important examples of polaritons are surface plasmon polaritons and phonon-polaritons;

however, in the context of this dissertation we will use the shorthand "polariton" to exclusively refer to microcavity exciton-polaritons. These quasiparticles necessarily emerge when there is a combination of intense electric field, strong oscillator strength in the material and low damping (and thus narrow linewidth) for both exciton and photon.

Qualitatively, one can imagine an exchange of excitation between the matter state and the photon mode at resonance due to the coupling. If the time scale of this exchange is longer than the respective lifetimes of the photon and exciton, the transfer is one directional (e.g. the photon is absorbed creating an exciton which then decays, or an exciton emits a photon which then escapes the cavity). This is the weak coupling regime. In contrast, if the lifetimes are long compared to the interaction time, or in other words, if the dipole interaction exceeds the irreversible decay mechanisms, coherent cyclic exchange will occur at a characteristic frequency Ω, called the vacuum Rabi frequency, that is proportional to the interaction strength. The lifetime of the exciton is determined by the radiative and non-radiative recombination rates, while for the photon it is proportional to the cavity Q.

In this chapter, we outline the physics and phenomena of the strong coupling regime. The organization is as follows: in §7.1, we introduce the basic properties of planar microcavities without active material resonances; three ways of modeling the energy-momentum dispersion of a strongly-coupled exciton in a cavity are presented in §7.2; and, finally, we conclude with a summary of prior work, in §7.3, focusing the discussion on major milestones and effects relevant to Chapters VIII and IX.

7.1 Planar microcavities

Due to the simplicity of their fabrication, much of the work on polaritonic phenomena in both organic and inorganic semiconductors has been performed in planar Fabry-Pérot (FP) microcavities; as such, we begin with a brief discussion of their properties.

Most simply, a planar microcavity consists of two mirrors, with reflectivities R_1 and R_2, separated by a distance L_c. The mirrors can consist of highly-reflective metallic films or distributed Bragg reflectors (DBRs) – stacks of alternating high- and low-index layers with thickness equal to $\lambda_0/4n_i$ where λ_0 is the target center wavelength and n_1 and n_2 are the layer refractive indices.

The high reflectivity of DBRs originates from constructive interference of reflections from each successive interface, which produce a wide stop-band centered at λ_0. The width of the band depends on the index contrast of the layers, while the overall reflectivity depends on both the contrast and the number of layer pairs, N, in the stack. The reflectivity can be calculated using the transfer matrix method and is given at normal incidence by [5]:

$$R = 1 - 4\frac{n_{ext}}{n_c}\left(\frac{n_1}{n_2}\right)^{2N} \qquad n_1 < n_2, \tag{7.2}$$

where n_c is the refractive index from which light is incident (e.g. the cavity) and n_{ext} is the index of the material on the other side of the mirror. For wavelengths near the center of the stopband, the angle-dependent reflectivity can be expressed as an approximately linear function of frequency by [5]:

$$r_{DBR}(\omega) = \sqrt{R}\exp\left[i\frac{n_c}{c}(\omega - \omega_0)L_{DBR}\cos\theta_c\right], \tag{7.3}$$

where ω_0 is the stopband center frequency, θ_c is the incidence angle, and L_{DBR} is the penetration depth of the optical field into the mirror. The expression in the exponent is the phase shift on reflection due to this penetration compared to an ideal mirror, $\Delta\phi(\omega)$. At normal incidence, L_{DBR} corresponds to twice the distance a fixed-phase mirror must be moved to achieve an equivalent phase shift [6]. It depends on both frequency and polarization of the incident light and is given, at normal incidence, by [5]:

$$L_{DBR} = \frac{\pi c}{n_c}\frac{n_1 n_2}{n_2 - n_1}. \tag{7.4}$$

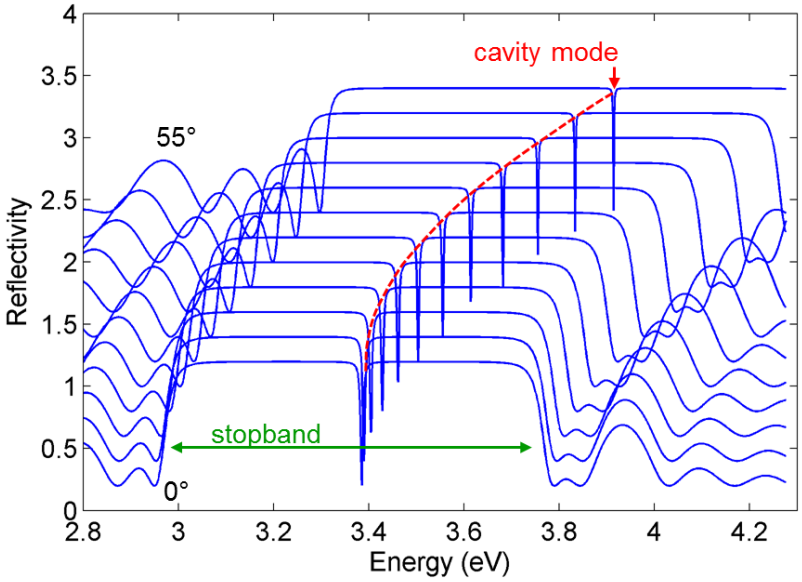

Figure 7.1: TE-polarized Fabry-Pérot cavity reflectivity for $\theta = 0$–$55°$ simulated using the transfer-matrix method. The cavity uses symmetric 8.5-pair SiO_2/Si_3N_4 DBR mirrors separated by a 230 nm SiO_2 layer. The dashed line highlights the dispersion of the cavity mode which is generally different than that of the DBRs themselves (as observed in the sidebands around the stopband).

In a Fabry-Pérot cavity, the resonance occurs when the constructive interference condition after one round trip is satisfied. For ideal mirrors, the resonance is directly related to the optical distance between the mirrors and is given by $\omega_c' = m\pi c/L_c n_c \cos\theta$ where m is an integer. Due to the penetration into the DBR, however, the effective optical distance is increased and the resonant cavity mode frequency is [5]:

$$\omega_c(\theta) = \frac{L_c\omega_c'(\theta) + L_{DBR}(\theta)\omega_0(\theta)}{L_{DBR} + L_c}. \tag{7.5}$$

Because of the extended optical field, the mode volume in these microcavities is larger than that for other structures (for example, using all metal mirrors). Nonetheless, fairly high quality factors can be achieved prolonging the photon lifetime ($\tau_c = \frac{Q\lambda_c}{2\pi c}$) and producing a sufficient degree of light-matter interaction for strong coupling to be observed.

The constructive interference condition gives rise to the quantization of the wavevec-

tor along the cavity axis: $k_\perp = \pi/L_{eff}$, where $L_{eff} = L_c + L_{DBR}$ and $k = \sqrt{k_\perp^2 + k_\parallel^2} = 2\pi/\lambda$. Using these relations, we can then express the energy-momentum dispersion of the cavity mode as:

$$\begin{aligned} E_{ph}(k) &= \hbar\omega_c = \frac{\hbar c}{n_c}k \\ &= \frac{\hbar c}{n_c}\left[\left(\frac{\pi}{L_{eff}}\right)^2 + k_\parallel^2\right]^{1/2}. \end{aligned} \tag{7.6}$$

Upon substituting $k_\parallel = E_{ph}(k)\sin(\theta)/\hbar c$ into Eq. 7.6, we can approximately express the incident angle-dependent energy of the photon mode [7]:

$$E_{ph}(\theta) = E_0\left(1 - \frac{\sin^2(\theta)}{n_{eff}^2}\right)^{-1/2} \tag{7.7}$$

where $E_0 = E_{ph}(\theta = 0)$ is the cut-off energy, and we have lumped the effects of mirror penetration and different layer dielectric constants into an effective refractive index n_{eff}. The result is that there is a one-to-one mapping between the in-plane momentum and incidence angle, which we can exploit to experimentally measure the energy-momentum dispersion of the photon (and the polariton) using angle-resolved reflectivity. In Fig. 7.1, we plot the reflectivity of a microcavity simulated by the transfer matrix method. The dispersions in the cavity mode and in the stopband can be clearly observed.

7.2 Strong exciton-photon coupling

In this section, we will outline three different methods of modeling the interaction between light in a microcavity with a resonant absorber. We briefly describe approaches based on the semiclassical [8], quantum [7] and classical linear dispersion theories [9].

7.2.1 Semiclassical theory

The semiclassical theory is frequently used to describe the strong coupling regime in inorganic microcavities where the excitons are confined to a series of quantum wells (QWs). It explicitly includes effects due to the position of the excitons in the cavity and reflections from the QW. Organic microcavities generally do not have a confined active layer distinct from the cavity material, and the treatment does not need to be so strict [9]. Nonetheless, for completeness, we will highlight the main features here. To correctly model the properties of QW, we must include nonlocal effects which can be represented by generalized transmission and reflection coefficients. For TE modes these are given by [5, 8, 10]:

$$\begin{aligned} r_{QW} &= -\frac{i\hbar\Gamma}{\Delta + i\hbar\Gamma} \\ t_{QW} &= 1 + r_{QW} \end{aligned} \tag{7.8}$$

here, Γ is the angle dependent radiative decay rate of the QW which is proportional to the exciton oscillator strength and $\Delta = \hbar\omega - \hbar\omega_{ex} - i\gamma_{ex}$ where $\hbar\omega_{ex} = E_{ex}$ is the exciton resonance and γ_{ex} is the exciton non-radiative broadening. Using the transfer matrix approach we can then write down the condition for constructive interference in the cavity [5, 8, 10]:

$$r_{DBR}^2\left(t_{QW}^2 - r_{QW}^2\right)\exp(i2k_z L_c) + 2r_{DBR}r_{QW}\exp(ik_z L_c) = 1. \tag{7.9}$$

Combining Eq. 7.8 and Eq. 7.9, and rearranging the terms yields:

$$\frac{\hbar\Gamma}{\hbar\omega - E_{ex} + i\gamma_{ex}} = i\frac{1 - r_{DBR}\exp(ik_z L_c)}{1 + r_{DBR}\exp(ik_z L_c)}. \tag{7.10}$$

Solutions to this equation are the eigenmodes of the system. For the case of a QW in the center of the cavity and near-resonance at normal incidence we get [8]:

$$(\hbar\omega - E_{ex} + i\gamma_{ex})(\hbar\omega - E_{ph} + i\gamma_{ph}) = V^2 \tag{7.11}$$

$$V^2 = \frac{\left(1+\sqrt{R}\right)}{\sqrt{R}} \frac{c\hbar\Gamma}{n_c L_{eff}} \tag{7.12}$$

where V is the interaction between the photon and exciton (off-diagonal matrix element in the Hamiltonian), γ_{ph} is the cavity halfwidth and other terms are defined in §7.1. The solutions to Eq. 7.11 are those for a system of coupled damped harmonic oscillators [8]:

$$\hbar\omega = \frac{E_{ex}+E_{ph}}{2} - i\frac{\gamma_{ex}+\gamma_{ph}}{2} \pm \sqrt{V^2 + \frac{1}{4}\left[E_{ex} - E_{ph} - i(\gamma_{ex}-\gamma_{ph})\right]^2}. \tag{7.13}$$

This directly gives us the energies of the polariton modes ($E = \hbar\omega$) in terms of the excitonic and cavity resonances. Clearly, the modes will be split if the square root is real. In the simple case of zero detuning between the cavity and exciton, $\delta = E_{ph} - E_{ex} = 0$, the strongly-coupled eigenmode energies are given by:

$$E = E_{ex} - i\frac{\gamma_{ex}+\gamma_{ph}}{2} \pm \frac{\Omega}{2}, \tag{7.14}$$

where Ω is the so-called Rabi splitting given by

$$\Omega = 2\sqrt{V^2 - \frac{1}{4}(\gamma_{ex}-\gamma_{ph})^2}. \tag{7.15}$$

A fully quantum-mechanical treatment of the system yields the same results [8].

Two immediate consequences are apparent: (i) the criterion for strong-coupling regime (i.e. normal mode splitting) is when the interaction exceeds the *difference* in linewidths, $2|V| > |\gamma_{ex} - \gamma_{ph}|$, and (ii) the splitting is maximized for well-matched linewidths of the exciton and cavity resonances with a maximum value $\Omega = 2V$. This

means that, knowing the linewidths and measuring the Rabi splitting, we can directly determine the strength of the exciton-photon coupling. From Eq. 7.12, it is also apparent that to increase the interaction strength, we want materials with large oscillator strength and mirrors with low penetration depth. Lastly, one should note that due to the generally broad excitonic resonances in organic materials, strong coupling can occur even in fairly low-Q cavities provided the oscillator strength is sufficient.

7.2.2 Coupled harmonic oscillator model

A convenient treatment is to directly take the exciton and photon as coupled harmonic oscillators. We will assume a dispersionless energy for the exciton (as is the case in organics) and a photon dispersion given by Eq. 7.7. As before, V will be the interaction matrix element of the coupled-system Hamiltonian [7]:

$$\begin{pmatrix} E_{ph} & V \\ V & E_{ex} \end{pmatrix} \begin{pmatrix} \alpha \\ \beta \end{pmatrix} = E \begin{pmatrix} \alpha \\ \beta \end{pmatrix}. \tag{7.16}$$

Here, α and β are the so-called Hopfield coefficients which represent the composition of the eigenstate in terms of the original uncoupled modes. This can be diagonalized to yield eigenvalue solutions of nearly the same form as Eq. 7.13:

$$\hbar\omega = \frac{E_{ex} + E_{ph}}{2} \pm \frac{1}{2}\sqrt{4V^2 + \left(E_{ex} - E_{ph}\right)^2}. \tag{7.17}$$

Although we have neglected broadening of the oscillators due to their finite lifetime, this model is convenient for systems where the Rabi splitting is greater than the cavity and exciton linewidths. Furthermore, it is straightforward to extend Eq. 7.16 to any number of coupled photons and/or excitons. Subsequently, we can use this Hamiltonian to fit angle-resolved photoluminescence (ARPL) or reflectivity data and extract each individual interaction strength.

7.2.3 Macroscopic linear dispersion model

Lastly, we outline a model frequently used in organic strongly coupled systems: that of classical macroscopic, linear dispersion. Here, we assume the cavity medium to have a background dielectric constants ε_b and a dispersionless absorption resonance at the exciton energy. We can adopt a definition for the Rabi splitting from the classical linear dispersion treatment of a Lorentzian oscillator in a cavity [11]:

$$\Omega = \sqrt{\frac{\alpha d F}{\pi}\delta_{ex}\delta_{ph} - \frac{\left(\delta_{ex} - \delta_{ph}\right)^2}{4}}. \tag{7.18}$$

Here, δ denotes the full-width half-maximum (FWHM) linewidth of the uncoupled photon mode or exciton, α is the active layer absorption, d is the active layer thickness, and $F = \frac{\pi\sqrt{R_1 R_2}}{1-R_1 R_2}$ is the finesse of the cavity given mirror reflectivities R_1 and R_2. Comparing this to Eq. 7.15, we identify the first term under the root as the interaction potential V. In this model, the width of the polariton features is the average of the uncoupled oscillator widths. Therefore, the Rabi splitting will be resolved when $\Omega >> (\delta_{ex} + \delta_{ph})/2$, or, more explicitly, when $\alpha d >> \pi/F$ [11].

To get the polariton eigenenergies, we can write down the following Maxwell equation for a transverse EM wave [9, 12]:

$$\frac{\hbar^2 c^2}{E^2}\left(k_z^2 + k_\parallel^2\right) = \varepsilon_b + \frac{A}{E_{ex}^2 - E^2 - 2iE\gamma_{ex}}. \tag{7.19}$$

Here, the in- and out-of-plane wavevectors are defined as before, ε_b accounts for all non-resonant transitions, A is proportional to the oscillator strength, and γ_{ex} is the total broadening of the exciton resonance. Near the point of resonance, we arrive at a familiar quadratic expression:

$$\left[E - E_{ph}(k_\parallel)\right]\left[E - E_{ex} + i\gamma_{ex}\right] = V^2, \tag{7.20}$$

with $V^2 = A/4\varepsilon_b$. If the resonance broadening is much smaller than the Rabi splitting, the solutions to Eq. 7.20 are the same as those attained previously with the semiclassical method (Eq. 7.13) and the coupled-oscillator Hamiltonian (Eq. 7.17). Despite the simplified treatment which neglects both multiple reflections by the active layer and its position within the cavity, for organic structures where the cavity is filled with the active material, this treatment is in good agreement with more accurate models.

7.3 Prior work

For the last two decades, microcavity polaritons using both organic and inorganic semiconductor active materials have been studied experimentally and theoretically. In this section, we will highlight some of the milestones leading to the current state of the field. A much richer compendium is available in Ref. [13].

7.3.1 Polaritons in inorganic microcavities

The first experiment observing the strong-coupling regime in a semiconductor microcavity was that of Weisbuch et al. in 1992 [14]. Using an in-plane thickness variation to tune the resonance of a double-DBR microcavity with multiple embedded GaAs QWs, the normal-incidence reflectivity of the structure was measured at 5 K. The low temperature increases the exciton lifetime and reduces the broadening, while multiple wells were used to increase the oscillator strength. This is necessary due to the WM-type excitons in GaAs having a large exciton Bohr radius ($a_B > 10\,\text{nm}$), weak binding on the order of 10 meV and relatively low absorption [15]. At positions where the cavity mode energy matched that of the exciton, rather than a single reflectivity minimum due to the QW resonance, two split minima were observed. As a function of detuning, these features formed two polariton branches anti-crossed around the resonance point with a Rabi splitting of 5 meV.

Following the initial demonstration, Houdré and Weisbuch measured the polariton

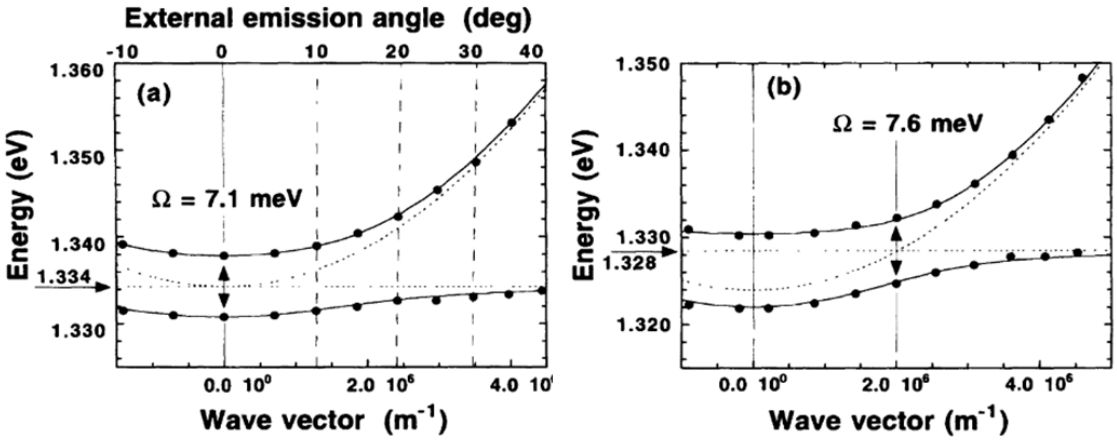

Figure 7.2: Polariton energy-momentum dispersion curves (solid lines) extracted from angle-resolved photoluminescence peak positions (circles) for resonances at (a) $\theta = 0°$ and (b) $\theta = 29°$. Broken lines indicate energies of the uncoupled cavity mode and exciton. Figure reproduced from Ref. [16].

energy-momentum dispersion using ARPL from a cavity containing InGaAs quantum wells at 77 K [16]. Due to the translational invariance in the plane of the cavity, the in-plane momentum ($k_{\|}$) of the polariton is conserved as the photonic component escapes the cavity by coupling to radiation modes. By measuring the angle and spectrum of the cavity luminescence, both $k_{\|}$ and energy of the original polariton were conveniently extracted (Fig. 7.2). Again, a clear branch splitting ($\Omega \approx 7$ meV) was observed near the point of degeneracy between the photon mode and exciton.

Relaxation dynamics and photoluminescence

The intensity of angle-dependent emission from strongly-coupled cavities is governed by the population dynamics of the polaritons. In the limit of infinite photon and exciton lifetimes, the population would reach a thermal equilibrium described by the Bose-Einstein distribution function since polaritons are bosonic quasiparticles (at low densities, this is identical to the Boltzmann distribution). In reality, the lifetime of the polaritons is limited by that of the photonic component (τ_c) which is on the order of fs to ps depending on cavity Q. Hence, polariton radiative decay competes with thermaliza-

tion. Moreover, if polaritons are created non-resonantly (Fig. 7.3a), initial relaxation to the exciton reservoir can have significant impact on the overall population distribution as excitonic radiative and non-radiative recombination competes with other relaxation mechanisms.

Using the semiclassical Boltzmann equation, Savona and Tassone described polariton photoluminescence in the linear regime [17–19]:

$$\frac{dN_k}{dt} = G_k - \Gamma_k N_k - N_k \sum_{k'} W_{k\to k'}(1+N_{k'}) + (1+N_k)\sum_{k'} W_{k'\to k} N_{k'}. \tag{7.21}$$

Here, N_k is the number of polaritons with wavevector k, G_k is the generation (pump) term, Γ_k is the natural decay, and $W_{k\to k'}$ is the rate of polariton scattering from k to k'. The scattering and decay processes are proportional to the initial state population. The scattering rate is also quantum-mechanically modified by the final state population represented by the $(1+N_{k'})$ factors, where 1 corresponds to spontaneous (classical) and $N_{k'}$ to stimulated scattering. Generally, relaxation along a polariton branch occurs via emission of high-energy optical or low-energy acoustic phonons in the linear regime. In the lower polariton (LP) branch, as the particle relaxes toward $k_\parallel = 0$, the photon fraction $|\alpha(k_\parallel)|^2$ increases, as does the radiative decay $\Gamma_k = |\alpha(k_\parallel)|^2/\tau_c$. At the same time, polariton-phonon scattering which is proportional to the excitonic fractions of the initial and final states $\left(W_{k\to k'} \sim |\beta_k|^2|\beta_{k'}|^2\right)$ becomes less effective. This leads to a so-called polariton bottleneck at the position where radiative decay dominates over further relaxation. Nonlinear effects that occur at higher densities such as polariton-polariton scattering are necessary to bypass the bottleneck.

Nonlinear effects

The first observations of nonlinear behavior attributed to stimulated scattering in the strong coupling regime were by Dang et al. [20], and Senellart and Bloch [21]. The

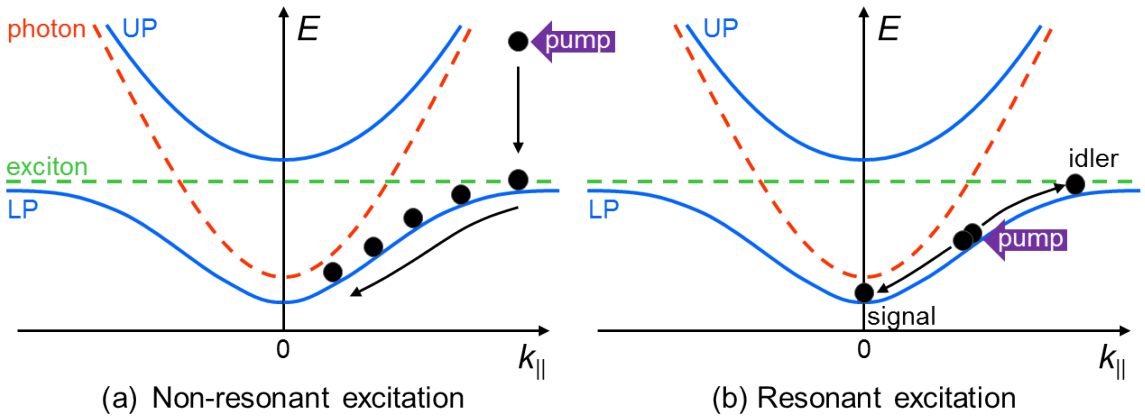

Figure 7.3: Diagram of optical excitation schemes for generating microcavity polaritons (a) non-resonantly and (b) resonantly. In (a), the pump energy is far above that of the polariton energy and creates hot excitons which relax to the reservoir before populating the polariton branch. In (b), the energy and momentum (angle) of the pump beam is chosen to coincide with a point on the dispersion curve directly exciting a polariton population. If Eq. 7.22 is satisfied, parametric scattering into the signal and idler states can occur.

latter identified polariton-polariton and polariton-exciton collisions as a contributing factor governing the population dynamics. The significant nonlinear polariton interactions stem directly from the large spatial extent of the Wannier-Mott excitons and the resulting low saturation density. At the turn of the century, Baumberg and Savvidis demonstrated parametric scattering of lower branch polaritons in a resonant pumping configuration (Fig. 7.3b) leading to *parametric oscillation* [22] and *parametric amplification* [23]. Parametric scattering can occur when both energy and momentum for the initial (pump) and final (signal and idler) states can be conserved:

$$\begin{aligned} 2E(k_{||}^{pump}) &= E(k_{||}^{signal}) + E(k_{||}^{idler}) \\ 2k_{||}^{pump} &= k_{||}^{signal} + k_{||}^{idler} \end{aligned} \tag{7.22}$$

By tuning the pump beam energy and angle to the spot on the LP dispersion which satisfies Eq. 7.22 (the so-called *magic angle*) and such that the $k_{||}^{signal} = 0$, a weak probe beam resonant with the branch minimum at normal incidence was significantly

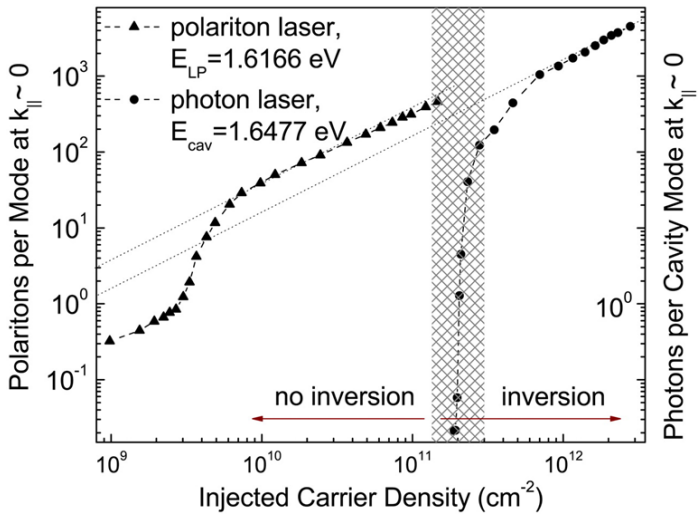

Figure 7.4: Polariton vs. photon lasing thresholds in a GaAs QW-based microcavity. The gray region marks the crossover from the strong- to weak-coupling regime as inversion is reached. Figure reproduced from Ref. [15].

amplified (parametric amplifier) [23]. Nonlinear polariton-polariton interaction was subsequently shown to be responsible for efficient population build-up in the probe (signal) state leading to the observed parametric gain [24]. Even without the probe beam, fluctuations in the population density at the signal energy can lead to stimulated parametric scattering producing a polariton parametric oscillator [22]. In both cases, the coherence of the emission results from the coherent pump.

The situation is different when non-resonant pumping is used to populate the polariton dispersion. As the initially produced excitons relax to large-wavevector polariton states via polariton-phonon scattering, the coherence of the initial pump beam is lost. Provided the subsequent relaxation mechanisms are sufficiently fast, as pump intensity is increased, the population build-up at the energy minimum can produce final state stimulation into the $k_{\|} = 0$ state (via the $1 + N_k$ factor in Eq. 7.21). This occurs when the final state population reaches $N = 1$. The resulting non-linear emission is termed *polariton lasing* and was first observed by Deng et al. [15, 25]. In this case, the coherence is not inherited from the pump, but instead arises spontaneously in the polariton ground state. The polariton lasing action is then due to *spontaneous* emis-

sion of radiation from a macroscopic coherent state, rather than *stimulated* emission of radiation as in a conventional laser. Indeed, as shown in Fig. 7.4, Deng observed that beyond the threshold for polariton lasing, pumping the same material system can produce an inverted electron-hole population resulting in conventional lasing with an order-of-magnitude higher threshold [15]. By measuring the second-order coherence, it was concluded that the polariton population transitions from a classical mixed state to a quantum-mechanical pure state above the polariton lasing threshold and thus forms a type of non-equilibrium Bose-Einstein condensation (BEC). The theoretical framework for the polariton laser was initially developed by Imamoğlu et al. [26].

Electrical injection and room temperature operation

For practical applications, electrically operated devices at room temperature are desired. While the majority of strong-coupled devices were studied under optical excitation, in 2008, several groups reported GaAs-based polariton light-emitting diodes operating at temperatures as high as 235 K under electrical injection [27–29]. Finally, in 2013, almost a decade after the first demonstration of an optically pumped polariton laser, two groups independently reported electrically-injected polariton lasing at low temperature using InGaAs/GaAs QWs embedded into an intrinsic active region between p- and n-doped DBRs.

The group of Pallab Bhattacharya at the University of Michigan used a 7 T magnetic field to reduce the WM exciton Bohr radius and increase the saturation density and exciton oscillator strength [30]. At 30 K, a nonlinear emission threshold corresponding to polariton lasing was observed at injection current density of $J = 12\,\mathrm{A/cm^2}$. At $J = 70\,\mathrm{A/cm^2}$, the system transitioned to the weak-coupling regime and conventional lasing threshold was reached at $J = 4 \times 10^4\,\mathrm{A/cm^2}$. In parallel, an international collaboration led by Sven Höfling observed both polariton and conventional lasing thresholds under electrical injection with and without an applied magnetic field [31]. In the absence

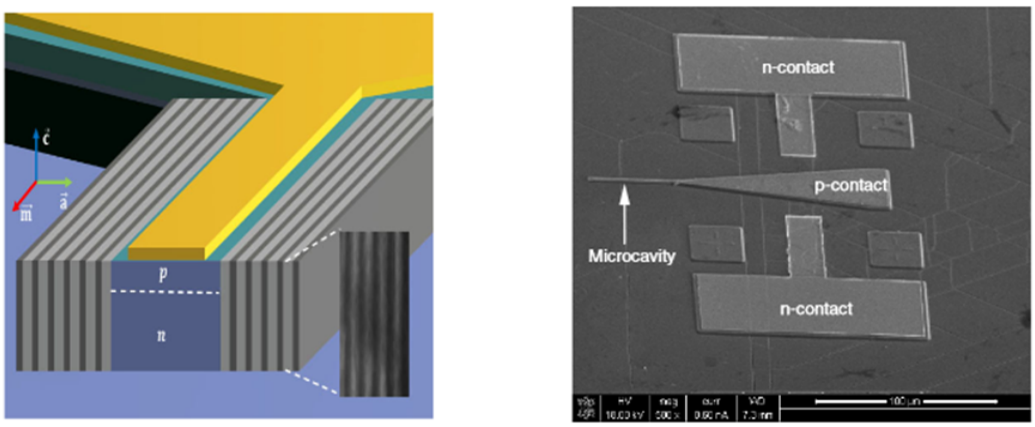

(a) (b)

Figure 7.5: Room-temperature electrically-pumped polariton laser GaN microcavity shown (a) schematically and (b) in SEM micrograph. The inset in (a) is an SEM image of the SiO_2/TiO_2 DBR. Figure reproduced from Ref. [32].

of the magnetic field, the polariton lasing threshold was reached at a current density of $J = 82 \pm 5\,\mathrm{A/cm^2}$, while at 5 T, the same nonlinear threshold at $J = 77 \pm 2\,\mathrm{A/cm^2}$ was much more pronounced due to changed cavity detuning and increased oscillator strength. In both cases, the conventional lasing threshold occurred at $J \approx 190\,\mathrm{A/cm^2}$. Still, these experiments were performed at 10 K due to the low-binding energy of GaAs excitons (4–10 meV) limiting their practicality.

Unlike GaAs, excitons in wide bandgap semiconductors GaN and ZnO are stable at higher temperatures due to binding energies of around 26 meV and 60 meV, respectively [33–35]. Taking advantage of this, strong-coupling demonstrations in bulk-based GaN [36] and ZnO [37] microcavities were extended to room temperature. Subsequently, room temperature polariton lasing was achieved in GaN and GaN/AlGaN QW cavities [38, 39], and in bulk ZnO microcavities [34]. Similar to the low-temperature regime, the thresholds for polariton lasing were shown to be an order of magnitude lower than those for conventional photon lasing in the same material systems [15, 34, 38].

These experiments were important steps toward practical polaritonic devices, and in 2014, Bhattacharya's group attained electrically-injected polariton lasing to room

temperature in a bulk GaN-based microcavity [32]. A unique feature of this cavity design was the orthogonal current injection relative to the optical feedback, shown in Fig. 7.5, allowing the use of a dielectric SiO_2/TiO_2 DBR on one side of the cavity. A polariton lasing threshold was observed at $J = 169\,\mathrm{A/cm^2}$, nearly one hundred times lower than edge- or surface-emitting GaN lasers, and much lower than the conventional lasing threshold reached at $J = 44\,\mathrm{kA/cm^2}$ in the same structure [32].

7.3.2 Polaritons in organic microcavities

High-temperature operation and electrically-pumped devices are a natural lead-in for our discussion of organic polaritons. Organic semiconductors offer several attractive properties for strongly-coupled structures particularly at room temperature. The Frenkel-type excitons in these materials possess binding energies $E_B = 0.1$–1 eV making them extremely stable even at room temperatures. Moreover, the oscillator strengths of organics far exceed those of inorganic materials leading to stronger interaction with light and greater Rabi splittings. On the other hand, the poor charge mobility in molecular materials is a contributing factor to the already considerable challenge of producing a conventional electrically-driven OSL. Since polariton laser thresholds can be lower than those for conventional lasers, achieving this in an organic microcavity may offer an alternate path toward electrical stimulation.

Early work

The earliest experimental demonstration of polariton formation in an organic microcavity was by Lidzey et al. [40]. Probed in reflectivity, the cavity was composed of a transparent polystyrene matrix doped with the dye 4TBPPZn and placed between a bottom DBR and a top silver mirror. The metal was used due to the difficulty of depositing a high-quality DBR on the organic film. Nonetheless, the observed Rabi splitting of $\Omega \approx 160\,\mathrm{meV}$ was significantly larger than any reported in inorganic cavities

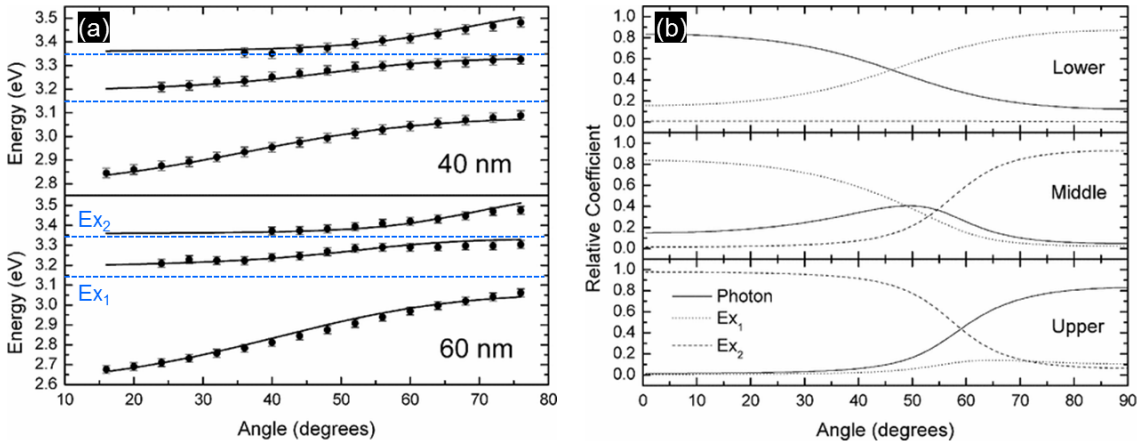

Figure 7.6: Strongly-coupled organic microcavity dispersions (a) for 40 nm and 60 nm thick NTCDA active regions. Both vibronic resonances of NTCDA couple to the photon mode producing three polariton branches. (b) The fractional composition of each branch for the 40 nm cavity. The middle branch is a hybrid of both excitons and the photon. Figure adapted from Ref. [42].

at the time [40]. The following year, polariton photoluminescence was reported at room temperature by the same group, this time, using J-aggregates of a cyanine dye [41]. The J-aggregates have relatively narrow resonances and oscillator strength that is proportional to the number of molecules in the aggregate. Typical of non-resonantly pumped organic polaritons, emission was only observed from the lower branch due to fast relaxation [9].

As discussed in §1.2.3, a characteristic feature of many organic materials is the presence of large-energy intramolecular vibrational modes. These can provide efficient relaxation pathways for polaritons. Moreover, Holmes and Forrest have shown that simultaneous strong coupling of the cavity photon to multiple vibronic resonances can occur [42]. Using a DBR and metal mirror cavity filled with thermally evaporated napthalene derivative NTCDA, a second anticrossing was observed near the resonance of the cavity mode with the 0-1 absorption line (Fig. 7.6a). This resulted in a "middle" polariton branch that is a hybrid of both excitonic transitions and the photon mode. Conceptually, this is similar to the polariton hybridization that will be discussed in §7.3.3; here, however, the multiple resonances originate from a single material.

It is straightforward to extend the Hopfield Hamiltonian in Eq. 7.16 to include multiple excitons:

$$\begin{pmatrix} E_{ph} & V_1 & V_2 \\ V_1 & E_{ex1} & 0 \\ V_2 & 0 & E_{ex2} \end{pmatrix} \begin{pmatrix} \alpha \\ \beta \\ \gamma \end{pmatrix} = E \begin{pmatrix} \alpha \\ \beta \\ \gamma, \end{pmatrix} \tag{7.23}$$

where the angle-dependent Hopfield coefficients $|\alpha|^2$, $|\beta|^2$ and $|\gamma|^2$ represent the fractional contribution of each photonic and excitonic resonance to the polariton. Holmes used this to fit the reflectivity data for the NTCDA microcavity and extract the hybridization as shown in Fig. 7.6. The rich population dynamics of strongly coupled molecules with vibronic progressions were analyzed theoretically by Mazza et al. [43].

Organic polariton laser

To date, there have been only three systems demonstrating polariton lasing in organic microcavities, two originally developed by Stéphane Kéna-Cohen and collaborators [44, 45] and one by Plumhof et al. [46]. The first system consisted of crystalline anthracene which was melt grown in thin capillary channels formed by cold-welding two high-quality PECVD-grown DBR mirrors using Au stripes. The schematic of the cavity, the anthracene crystal unit cell and the resulting polariton dispersion are shown in Fig. 7.7. Under pulsed non-resonant pumping, nonlinear increase in emission was observed upon reaching a threshold pump fluence ($P_{th} = 120\,\mathrm{nJ}$). This was accompanied by simultaneous collapse of the population to the bottom of the lower polariton branch, a reduction in emission lifetime and spectral narrowing. A key realization was arranging the cavity detuning such that the lower polariton minimum coincided with the uncoupled first vibronic emission of anthracene thus allowing efficient direct dipole-mediated radiative scattering from the exciton reservoir [44, 47]. In Chapter VIII, we will investigate the connection between the polariton lasing threshold in this system and the critical density for Bose-Einstein condensation.

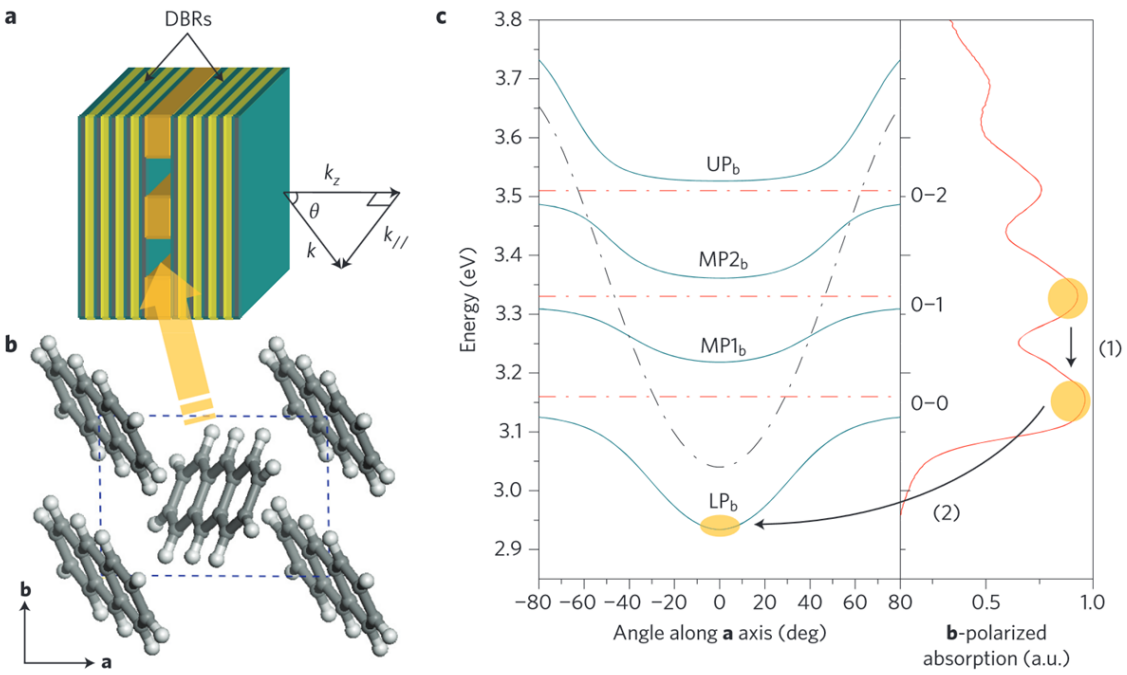

Figure 7.7: Schematic of (a) the anthracene polariton laser double-DBR microcavity, (b) anthracene crystal unit cell, and (c) the polariton dispersion resulting from coupling the cavity mode to three vibronic resonances. Upon non-resonant excitation, (1) fast relaxation occurs to the exciton reservoir from which (2) radiative pumping efficiently populates the lower polariton minimum. Figure reproduced from Ref. [44].

A more recent instance of small-molecule organic polariton lasing was reported in a strong-coupled microcavity consisting of thermally evaporated film of TDAF between two SiO_2/Ta_2O_5 DBRs [45]. Lasing was demonstrated for two different detunings. In addition to nonlinear emission increase, spectral and k-space narrowing, and a power-dependent blueshift was observed above lasing threshold. These findings indicate that in addition to efficient single scattering events from the exciton reservoir to the branch minimum, noticeable polariton-polariton or polariton-exciton interaction serves to redistribute the population. These nonlinear interactions have not been observed previously in organics and may eventually help reduce polariton lasing thresholds to allow electrical injection.

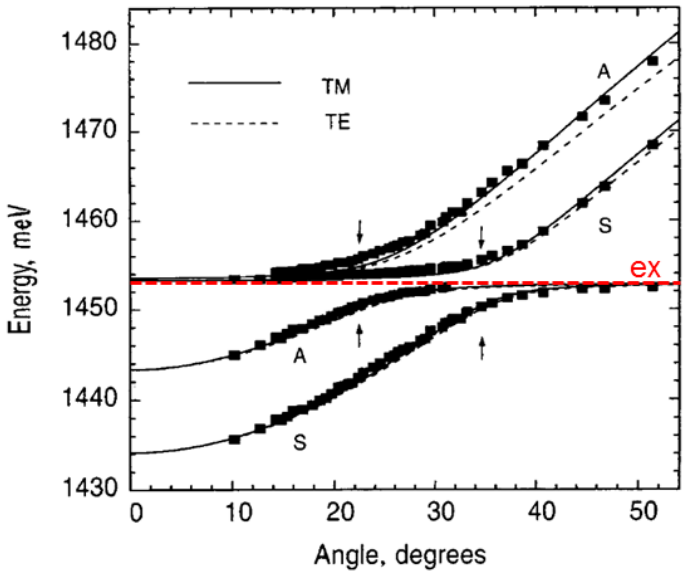

Figure 7.8: Simultaneous strong coupling of multiple cavities with one GaAs QW exciton resonance. Two anti-crossings (indicated by arrows) were observed in the polariton dispersion. Figure reproduced from Ref. [5].

7.3.3 Polariton hybridization

As mentioned previously, multiple cavity and excitonic resonances can be simultaneously strong coupled producing polariton branch anti-crossings at each degeneracy. In inorganics, Wainstain demonstrated simultaneous coupling of excitons from different-width QWs to the cavity photon [48]. Similarly, Panzarini coupled two nearby microcavities each containing several resonant GaAs QWs producing the two-photon/one-exciton mixed polaritons shown in Fig. 7.8 [5]. In organics, Lidzey used two spatially separate films of different cyanine dyes coupled to the same cavity mode [49] to produce photon-mediated hybridization. Advantageously, the resulting dispersion could be trivially tuned by adjusting the concentrations of each dye (and thus their respective oscillator strengths). Quite recently, Coles et al. have demonstrated that the hybrid states of two intermixed J-aggregated dyes in a strongly-coupled cavity serve as an efficient pathway for ultrafast energy transfer between their excited states [50].

Even prior to the realization of cavity polaritons in organics, Agranovich and others

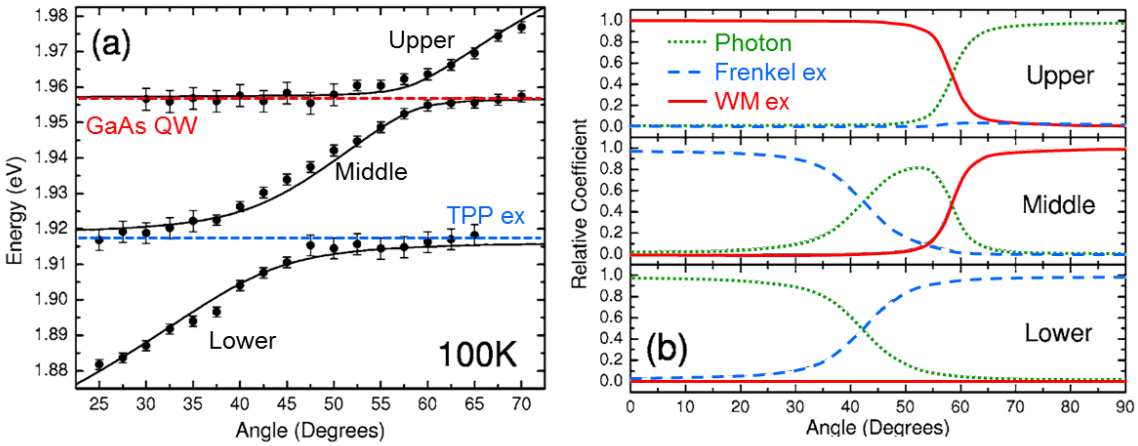

Figure 7.9: Strong coupling in a microcavity with GaAs QW and organic TPP resonances. (a) Hybrid organic-inorganic polariton dispersion measured by reflectivity. (b) Hopfield mixing coefficients of each polariton branch. Figure adapted from Ref. [56].

realized that the strong-coupling regime can be used to hybridize Frenkel and Wannier-Mott excitons [51]. The long-standing interest in such hybrid states stems from the possibility of producing excitations whose properties (e.g. oscillator strength, Bohr radius, saturation density) are a favorable combination of the constituent exciton character [52]. These hybrid Frenkel-Wannier-Mott excitations could be used to tailor the optical nonlinearity and energy transfer processes [53, 54]. A good overview of the physics in hybrid resonant nanostructures can be found in Ref. [55]. Furthermore, given recent advances in electrically injected inorganic polariton lasers [30–32], one can imagine hybrid organic-inorganic polariton systems that are stimulated electrically solely through the inorganic part of the cavity.

In 2006, the first experimental Frenkel-Wannier-Mott hybridization in the strong-coupling regime was demonstrated by Holmes et al. [56], and Wenus et al. [57]. Using an epitaxially grown bottom AlGaAs/AlAs mirror and nine InGaP QWs with thermally evaporated organic film of tetraphenylporphyrin (TPP) and a TiO_2/SiO_2 top DBR, Holmes observed three polariton branches reflectivity up to 100 K (Fig. 7.9a). At the point of equal Frenkel-Wannier-Mott (FWM) hybridization, the middle polariton branch

consisted of 10 % contributions from each exciton and 80 % photon (Fig. 7.9b). Similar experimental findings were reported for cavities containing the organic dye ZnTPP and the perovskite PEATBP at room temperature [57], and, later, ZnO and the perovskite MFMPB at 5 K [58]. In Chapter IX, we will revisit Frenkel-Wannier-Mott exciton hybridization, demonstrating angle-independent mixing of organic and inorganic excited states in the strong-coupling regime at room temperature.

CHAPTER VII

Bibliography

[1] V. Bulović, V. B. Khalfin, G. Gu, P. E. Burrows, D. Z. Garbuzov, and S. R. Forrest, *Phys. Rev. B* **58**, 3730 (1998).

[2] H. Yokoyama and K. Ujihara, *Spontaneous Emission and Laser Oscillation in Microcavities* (Taylor & Francis, 1995).

[3] E. M. Purcell, *Phys. Rev.* **69**, 681 (1946).

[4] J. J. Hopfield, *Phys. Rev.* **112**, 1555 (1958).

[5] G. Panzarini, L. Andreani, A. Armitage, D. Baxter, et al., *Phys. Solid State* **41**, 1223 (1999).

[6] D. I. Babic and S. Corzine, *J. Quantum Electron.* **28**, 514 (1992).

[7] M. S. Skolnick, T. A. Fisher, and D. M. Whittaker, *Semicond. Sci. Technol.* **13**, 645 (1998).

[8] V. Savona, L. Andreani, P. Schwendimann, and A. Quattropani, *Solid State Commun.* **93**, 733 (1995).

[9] V. M. Agranovich, M. Litinskaia, and D. G. Lidzey, *Phys. Rev. B* **67**, 085311 (2003).

[10] L. C. Andreani, *Phys. Lett. A* **192**, 99 (1994).

[11] Y. Zhu, D. J. Gauthier, S. E. Morin, Q. Wu, H. J. Carmichael, and T. W. Mossberg, *Phys. Rev. Lett.* **64**, 2499 (1990).

[12] R. Houdré, R. Stanley, U. Oesterle, M. Ilegems, and C. Weisbuch, *Phys. Rev. B* **49**, 16761 (1994).

[13] D. Sanvitto and V. Timofeev, *Exciton Polaritons in Microcavities: New Frontiers* (Springer, 2012).

[14] C. Weisbuch, M. Nishioka, A. Ishikawa, and Y. Arakawa, *Phys. Rev. Lett.* **69**, 3314 (1992).

[15] H. Deng, G. Weihs, D. Snoke, J. Bloch, and Y. Yamamoto, *P. Natl. Acad. Sci.* **100**, 15318 (2003).

[16] R. Houdré, C. Weisbuch, R. P. Stanley, U. Oesterle, P. Pellandini, and M. Ilegems, *Phys. Rev. Lett.* **73**, 2043 (1994).

[17] V. Savona, F. Tassone, C. Piermarocchi, A. Quattropani, and P. Schwendimann, *Phys. Rev. B* **53**, 13051 (1996).

[18] F. Tassone, C. Piermarocchi, V. Savona, A. Quattropani, and P. Schwendimann, *Phys. Rev. B* **53**, R7642 (1996).

[19] F. Tassone, C. Piermarocchi, V. Savona, A. Quattropani, and P. Schwendimann, *Phys. Rev. B* **56**, 7554 (1997).

[20] L. S. Dang, D. Heger, R. André, F. Bœuf, and R. Romestain, *Phys. Rev. Lett.* **81**, 3920 (1998).

[21] P. Senellart and J. Bloch, *Phys. Rev. Lett.* **82**, 1233 (1999).

[22] J. J. Baumberg, P. G. Savvidis, R. M. Stevenson, A. I. Tartakovskii, et al., *Phys. Rev. B* **62**, R16247 (2000).

[23] P. G. Savvidis, J. J. Baumberg, R. M. Stevenson, M. S. Skolnick, D. M. Whittaker, and J. S. Roberts, *Phys. Rev. Lett.* **84**, 1547 (2000).

[24] C. Ciuti, P. Schwendimann, and A. Quattropani, *Semicond. Sci. Technol.* **18**, S279 (2003).

[25] H. Deng, G. Weihs, C. Santori, J. Bloch, and Y. Yamamoto, *Science* **298**, 199 (2002).

[26] A. Imamoğlu, R. J. Ram, S. Pau, and Y. Yamamoto, *Phys. Rev. A* **53**, 4250 (1996).

[27] S. Tsintzos, N. P. amd G. Konstantinidis, Z. Hatzopoulos, and P. G. Savvidis, *Nature* **453**, 372 (2008).

[28] A. A. Khalifa, A. P. D. Love, D. N. Krizhanovskii, M. S. Skolnick, and J. S. Roberts, *Appl. Phys. Lett.* **92**, 061107 (2008).

[29] D. Bajoni, E. Semenova, A. Lemaître, S. Bouchoule, et al., *Phys. Rev. B* **77**, 113303 (2008).

[30] P. Bhattacharya, B. Xiao, A. Das, S. Bhowmick, and J. Heo, *Phys. Rev. Lett.* **110**, 206403 (2013).

[31] C. Schneider, A. Rahimi-Iman, N. Y. Kim, J. Fischer, et al., *Nature* **497**, 348 (2013).

[32] P. Bhattacharya, T. Frost, S. Deshpande, M. Z. Baten, A. Hazari, and A. Das, *Phys. Rev. Lett.* **112**, 236802 (2014).

[33] M. Zamfirescu, A. Kavokin, B. Gil, G. Malpuech, and M. Kaliteevski, *Phys. Rev. B* **65**, 161205 (2002).

[34] T.-C. Lu, Y.-Y. Lai, Y.-P. Lan, S.-W. Huang, et al., *Opt. Express* **20**, 5530 (2012).

[35] Y.-Y. Lai, Y.-P. Lan, and T.-C. Lu, *Light: Sci. Appl.* **2**, e76 (2013).

[36] R. Butté, G. Christmann, E. Feltin, J.-F. Carlin, et al., *Phys. Rev. B* **73**, 033315 (2006).

[37] R. Shimada, J. Xie, V. Avrutin, Ü. Özgür, and H. Morkoč, *Appl. Phys. Lett.* **92**, 011127 (2008).

[38] S. Christopoulos, G. B. H. von Högersthal, A. J. D. Grundy, P. G. Lagoudakis, et al., *Phys. Rev. Lett.* **98**, 126405 (2007).

[39] G. Christmann, R. Butté, E. Feltin, J.-F. Carlin, and N. Grandjean, *Appl. Phys. Lett.* **93**, 051102 (2008).

[40] D. Lidzey, D. Bradley, M. Skolnick, T. Virgili, S. Walker, and D. M. Whittaker, *Nature* **395**, 53 (1998).

[41] D. G. Lidzey, D. D. C. Bradley, T. Virgili, A. Armitage, M. S. Skolnick, and S. Walker, *Phys. Rev. Lett.* **82**, 3316 (1999).

[42] R. J. Holmes and S. R. Forrest, *Phys. Rev. Lett.* **93**, 186404 (2004).

[43] L. Mazza, L. Fontanesi, and G. C. La Rocca, *Phys. Rev. B* **80**, 235314 (2009).

[44] S. Kéna-Cohen and S. R. Forrest, *Nat. Photonics* **4**, 371 (2010).

[45] K. Daskalakis, S. Maier, and R. M. and S. Kéna-Cohen, *Nat. Mater.* **13**, 271 (2014).

[46] J. D. Plumhof, T. Stöferle, L. Mai, and U. S. and R. F. Mahrt, *Nat. Mater.* **13**, 247 (2014).

[47] L. Mazza, S. Kéna-Cohen, P. Michetti, and G. C. La Rocca, *Phys. Rev. B* **88**, 075321 (2013).

[48] J. Wainstain, C. Delalande, D. Gendt, M. Voos, et al., *Phys. Rev. B* **58**, 7269 (1998).

[49] D. G. Lidzey, D. D. C. Bradley, A. Armitage, S. Walker, and M. S. Skolnick, *Science* **288**, 1620 (2000).

[50] D. M. Coles, N. Somaschi, P. Michetti, C. Clark, et al., *Nat. Mater.* **13**, 712 (2014).

[51] V. Agranovich, H. Benisty, and C. Weisbuch, *Solid State Commun.* **102**, 631 (1997).

[52] V. Agranovich, R. Atanasov, and F. Bassani, *Solid State Commun.* **92**, 295 (1994).

[53] V. Agranovich, G. La Rocca, F. Bassani, H. Benisty, and C. Weisbuch, *Opt. Mater.* **9**, 430 (1998).

[54] V. M. Agranovich, D. M. Basko, G. C. L. Rocca, and F. Bassani, *J. Phys.: Condens. Matter* **10**, 9369 (1998).

[55] V. M. Agranovich, Y. N. Gartstein, and M. Litinskaya, *Chem. Rev.* **111**, 5179 (2011).

[56] R. J. Holmes, S. Kéna-Cohen, V. M. Menon, and S. R. Forrest, *Phys. Rev. B* **74**, 235211 (2006).

[57] J. Wenus, R. Parashkov, S. Ceccarelli, A. Brehier, et al., *Phys. Rev. B* **74**, 235212 (2006).

[58] G. Lanty, S. Zhang, J. S. Lauret, E. Deleporte, et al., *Phys. Rev. B* **84**, 195449 (2011).

CHAPTER VIII

Temperature dependence of polariton lasing in a crystalline anthracene microcavity

8.1 Introduction

Strong coupling between excitons and cavity photon modes results in new eigenstates of the system: the microcavity polaritons. Due to its photonic contribution, the effective mass of the polariton is greatly reduced from that of the bare exciton, and the integer-spin polaritons can undergo BEC at higher temperatures than cold atoms or excitons [1, 2]. In the last decade, this has led to extensive work on polariton lasing in both inorganic [3, 4] and organic semiconductors [5], exhibiting a non-equilibrium form of a BEC [2]. In contrast to conventional lasers where coherent emission occurs by stimulated emission of light, polariton lasers operate by stimulated scattering (condensation) into the bosonic ground state. Lasing action is then the result of *coherent* spontaneous emission from the condensed polaritons [2].

Most polariton lasers to date have consisted of optically-pumped, planar, 2D cavities with an active medium (either a series of quantum wells or bulk semiconductor) positioned at the antinode of the cavity field. Although for infinite 2D systems a BEC is not possible, condensation can nevertheless occur in the presence of particle interactions or in a finite-sized system. All practical polariton lasers are subject to one or both of these conditions, and following the treatment of Malpuech, et al. [6], the critical density (N_c) above which condensation occurs in the thermodynamic limit can be derived directly

from Bose statistics and the energy-momentum dispersion of the polaritons. Typically, this yields a critical density that monotonically increases with temperature, producing additional challenges for room-temperature operation.

A different situation emerges if the polariton relaxation is too slow compared to polariton decay pathways and the condensing polaritons cannot reach quasi-equilibrium below or above threshold [7]. In this instance, the system is in a kinetic limit and cannot be described by a BEC critical density and any temperature dependence will be due to the kinetic processes. An intermediate regime can occur, where the dynamics of the system are governed by kinetic processes below threshold, yet a thermalized state is achieved above threshold [7]. A number of works have investigated this phase diagram in inorganic microcavities [7–11] by varying the detuning, finding that that the temperature dependence in the kinetic regime can oppose that in the thermodynamic limit. These competing trends produced an optimal detuning that balanced the kinetic and thermodynamic processes to minimize the lasing threshold.

Recently Kéna-Cohen and Forrest [5] demonstrated that the large exciton binding energy and oscillator strength characteristic of crystalline organic semiconductors makes them particularly advantageous for polariton lasing at room temperature. Unlike their inorganic counterparts, conventional OSLs are known to be relatively unaffected by thermal effects due to the localized nature of the molecular excited state [12, 13]. On the other hand, if the polariton lasing threshold is related to the critical density for Bose-Einstein (BE) condensation, one expects a dependence on temperature for organic polariton lasers even in the absence of temperature-dependent kinetic processes. In this chapter, we investigate the polariton lasing threshold in the 12–300 K temperature range and its relation to the critical density for condensation. We find that the threshold pump density is six orders of magnitude higher than that needed to reach the N_c in the thermodynamic limit, implying that radiative and non-radiative losses during the relaxation from the exciton reservoir to the polariton ground state play a significant

role but are largely independent of temperature. When the efficiency of populating the polariton ground state is taken into account, we find that the critical density formulation adequately describes the lasing threshold temperature dependence.

8.2 Experimental Methods

As in prior work [5], the test structure is a FP cavity consisting of two closely spaced DBR mirrors whose gap is filled with crystalline anthracene (Fig. 7.7a). The DBR mirrors consist of 12 alternating pairs of Si_3N_4 and SiO_2 that were deposited by PECVD onto 0.5-mm-thick sapphire substrates. The refractive index of the individual layers (n_i) was measured using variable-angle spectroscopic ellipsometry and the layer thicknesses (d_i) were adjusted to satisfy $d_i = \frac{\lambda}{4n_i}$ where $\lambda = 422$ nm is the desired resonance wavelength. Next, 60-nm-thick gold stripes were deposited onto the DBR-coated sapphire by e-beam evaporation. Two identical substrates were pressed together at 75 MPa to cold-weld the gold stripes [14], forming 120-nm-thick by 2-mm-wide empty channels that were subsequently infiltrated with molten anthracene by capillary action at 240 °C in a nitrogen atmosphere. The samples were cooled at 1 °C/min to allow the molten anthracene to crystallize in the channel. "Bare" anthracene samples were fabricated using the same technique without depositing DBRs. For comparison, a conventional distributed feedback (DFB) OSL was made by interference lithography and chemical etching [15] of a SiO_2-on-Si substrate to form the Bragg grating with a period of 430 nm and a depth of 50 nm. The active medium consisted of a 300-nm-thick layer of 2 % (by volume) DCM2 doped Alq_3 that was deposited onto the grating by VTE.

Anthracene samples were non-resonantly optically pumped at $\lambda = 360$ nm using the 4th harmonic of the signal from an optical parametric amplifier (TOPAS-C) pumped by a Clark-MXR CPA-series Ti:Sapphire regenerative amplifier producing 150 fs pulses at a 1 kHz repetition rate, focused to a $\sim$200 μm diameter spot at 7.5° from normal incidence. The pumping intensity was controlled using a metallic variable neutral density filter

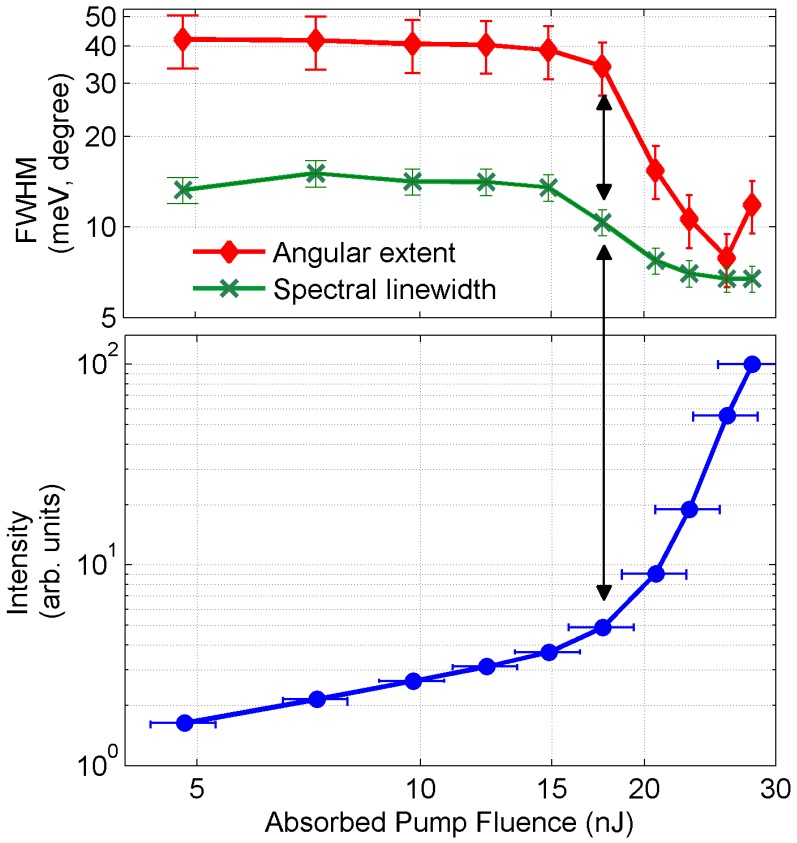

Figure 8.1: Normal incidence integrated intensity (circles), spectral linewidth (crosses) and angular extent (diamonds) of polariton emission as a function of absorbed pump fluence. All three exhibit a clear transition at the lasing threshold, indicated by the arrows.

and measured with a high-sensitivity calibrated Si photodetector (Coherent J-10Si-LE). Angle-resolved photoluminescence (PL) of anthracene was collected in the transmission geometry with angular resolution and step size of 2.5° by a fiber bundle located on a rotating arm of a goniometer and connected to a CCD spectrometer (Acton SP-2300i). A $\lambda = 400\,\text{nm}$ long-pass filter was used to eliminate stray pump light. All measurements were performed inside a closed-cycle He cryostat with a PID-controlled heater to vary the temperature.

8.3 Results

The three molecular vibronics of anthracene couple to the cavity photon mode, producing four polariton eigenstates as shown in Fig. 7.7(c) [16], the lowest of which emits significant photoluminescence. Additionally, the anthracene crystal has two molecules per unit cell, producing two excitonic components that further split the lower polariton branch into Davydov components polarized along the **a** and **b** crystal axes [16]. When the photonic component of the polariton escapes the cavity, the in-plane momentum ($k_{||}$) is conserved, with a one-to-one correspondence between the angle of emission and $k_{||}$, allowing for a mapping of the cavity-polariton energy-momentum dispersion through ARPL.

Figure 8.1 shows integrated PL intensity of the lowest **b**-polariton (LP_b) measured at $\theta = 0°$. The same data is also plotted for a range of temperatures in Fig. 8.2. Below the threshold pump fluence, the polariton luminescence is sublinear and largely unaffected by temperature. Above threshold, a superlinear increase in output intensity is observed, accompanied by spectral narrowing that indicates the onset of coherence. Simultaneously, the angular extent of emission sharply decreases (Fig. 8.1), suggesting that polaritons collect at the bottom of the LP_b branch, as is evident in Fig. 8.3. Previously, a Hermite-Gaussian TEM_{01} modal structure of the lasing spot has been observed above threshold [5]. All three transitions occur simultaneously for the entire range of temperatures between 12 K and 300 K, providing self-consistent evidence for lasing.

The ARPL dispersion is plotted in Fig. 8.3 at room temperature and at temperature $T = 70$ K, both below and above the lasing threshold. The energy-momentum dispersion in all four graphs is fit to the coupled-oscillator model [16] using an effective index, $n_{eff} = 1.78 \pm 0.03$, a cavity resonance, $E_{ph}(k_{||} = 0) = 3.1$ eV, and a lowest-vibronic exciton-photon coupling strength, $V_1 = 190$ meV. The detuning between the photon mode and lowest excitonic level ($\delta \approx -60$ meV), determined by the cavity length and penetration into the DBRs, is slightly smaller than in Ref. [5], while the coupling

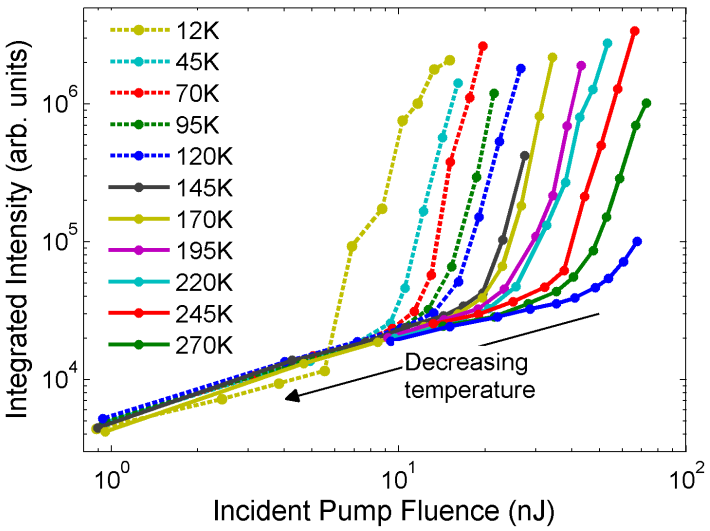

Figure 8.2: Integrated emission intensity of the lower polariton taken at $= 0°$ vs. incident pump fluence for a range of temperatures. Below threshold the curves coincide indicating that the polariton PL efficiency is not temperature dependent.

strength is higher. The population distribution along the LP_b branch, $N(\theta)$ is roughly proportional to the ARPL intensity:

$$N(\theta) \sim \frac{I_{LP}(\theta)}{|\alpha(\theta)|^2} \tag{8.1}$$

with I_{LP} the integrated intensity at collection angle θ and $|\alpha|^2$ the photon fraction from the coupled-oscillator model [16]. This can be divided into three regions above threshold: the ground state population, the Boltzmann-like distribution < 70 meV above the ground state, and the tail > 70 meV above ground state. Below threshold, the ground state population is indistinguishable from the Boltzmann-like region. As in prior work, the experimental spot is chosen such that the energy minimum of the LP_b branch is near 2.94 eV. This creates a resonance between the branch minimum and the 1-0 vibronic emission of anthracene and helps to populate the ground state directly from the exciton reservoir by optical pumping [5]. Conversely, the tail region is likely populated through relatively slow phonon-assisted relaxation from the reservoir. The shape of the

dispersion curve is independent of temperature and pump fluence, indicating that the system remains in the strongly coupled regime with polariton lasing occurring from the $k_{||} = 0$ minimum. However, limitations in the instrumental apparatus prevent us from producing a meaningful fit of the true population distribution and extracting an effective temperature for the uncondensed polaritons in the middle region of the LP_b branch. On the other hand, PL from a "bare" anthracene sample is clearly not polaritonic as it lacks the characteristic energy dispersion; instead, we observe a flat exciton-like dispersion with a typical vibronic progression of emission peaks near 2.8 eV, 2.94 eV and 3.08 eV at all angles (Fig. 8.4).

The threshold pump fluence for polariton lasing is linearly reduced with decreasing temperature, as shown in Fig. 8.5, while the spectral linewidths below and above threshold remain relatively constant with temperature at 13 ± 2meV and 6 ± 2meV, respectively. It should be noted that the linewidths are broadened due to averaging over the variations in the sample covered by the pump spot. Judging by the change in detuning near the probed spot, the intrinsic linewidth above threshold is likely at least 2–3 times narrower than observed. From the linewidth, a lower bound estimate of $Q \approx 600$ can be made for our cavity, which is one order of magnitude lower than the value for a cavity with perfectly flat DBRs predicted by transfer matrix calculations. Unlike in the case of inorganic semiconductors [8, 11], no blue-shift of the emission due to polariton-polariton or polariton-exciton interactions above threshold is observed with increasing power possibly due to the dominance of radiative pumping of the LP_b minimum by the 1-0 vibronic of anthracene over polariton-polariton mediated relaxation, though further investigation of the kinetics is necessary to determine this definitively. Likewise, no linewidth broadening is observed above threshold, however this may be masked by spatial averaging over sample inhomogeneity.

As in previous work [12], we observe practically no lasing threshold dependence on temperature in the conventional organic DFB laser over the same range, in sharp con-

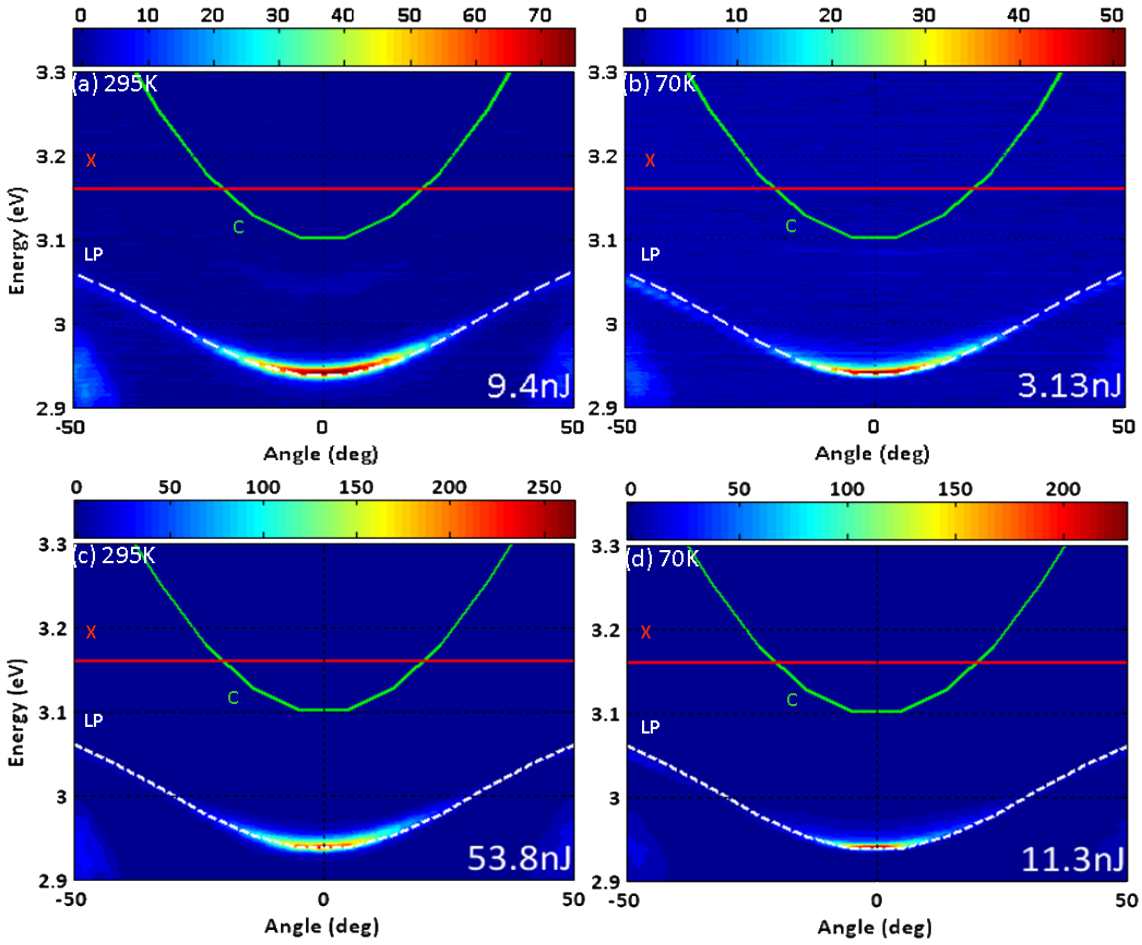

Figure 8.3: Angle-resolved polariton photoluminescence showing the characteristic polariton dispersion below (a) and (b), and above (c) and (d) the lasing threshold at room temperature and 70 K. Here, lasing threshold is determined by the transitions in linewidth and emission intensity as defined in Fig. 8.1. The dispersion fit to a coupled-oscillator model (dashed white line) remains unchanged, indicating strong coupling at both temperatures below and above lasing threshold. The cavity photon (green line) and the position of the uncoupled lowest anthracene vibronic (red line) are indicated; the detuning between them is $\delta \approx -60$ meV.

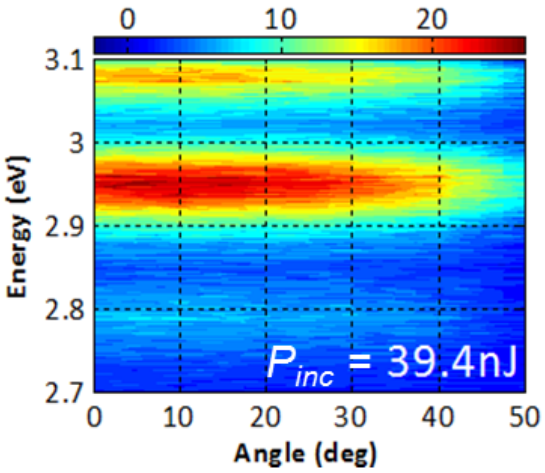

Figure 8.4: Angle-resolved photoluminescence of anthracene showing a flat, exciton-like dispersion.

trast to the polariton laser. Previously, temperature-dependent amplified spontaneous emission (ASE) has been observed in conjugated polymers and attributed to a change in the Stokes shift between emission and absorption spectra [17]. Since anthracene also has significant self-absorption, a Stokes shift change could reduce optical losses, thereby producing a lower threshold at low temperatures. In the polariton case, this could affect the strength of the photon-exciton coupling, producing slightly different dispersion curves at each temperature, but this is not observed. Instead, we see a slight narrowing of "bare" anthracene emission and absorption peaks at lower temperature but no relative energy shift. More recently, Coles, et al. found that the vibrationally-assisted scattering of excitons to lower branch polaritons in a strongly-coupled cavity containing a J-aggregate of an organic cyanine dye is weakly inhibited at reduced temperature [18]. This trend, due to kinetic processes, would counteract the threshold reduction due to thermodynamic effects as the temperature is decreased. Depending on the precise balance between kinetics and thermodynamics, the threshold dependence on temperature may be weakened or even entirely reversed compared to that of the critical density for 2D BEC [7–11].

8.4 Lasing threshold vs. critical density for condensation

To estimate the critical density for BEC, the parameters of the coupled-oscillator model fit are used to construct the dispersion $E(k_{||})$ out to the edge of the spherical Brillouin zone ($k_{||} = 2\pi/a$), where a is the average of the anthracene **a** and **b** unit cell dimensions). Assuming a finite 2D system approximately equal to the pump spot size, we express the critical density using [6]:

$$N_c = \frac{1}{\pi R^2} \sum_{k_{||}, k_{||} \geq \frac{2\pi}{R}} f_B(k_{||}, \mu), \tag{8.2}$$

where R is the size of the system, and f_B is the Bose-Einstein distribution function:

$$f_B(k_{||}, T, \mu) = \left[\exp\left(\frac{E(k_{||}) - E(0) - \mu}{k_B T} \right) - 1 \right]^{-1}. \tag{8.3}$$

The chemical potential, μ, approaches 0, allowing for an unlimited number of bosons in excess of the critical density to populate the ground state. Substituting the LP_b dispersion and evaluating the sum in Eq. 8.2 gives N_c as a function of temperature, as shown in Fig. 8.5 (line). The calculated linear regime extends above room temperature to nearly 400 K for anthracene due to a stronger light-matter interaction compared to that of commonly employed inorganic systems [19].

If we assume a polariton PL quantum efficiency, η, that accounts for various radiative and non-radiative loss mechanisms and an estimated 50 % absorption of incident light by the active medium, then the polariton density is given by $N = \eta \times N_{inc}(2V)^{-1}$, where N_{inc} is the number of incident photons and V is the active volume. Comparing the experimental threshold pump fluence with the critical BEC density in the thermodynamic limit yields a quantum efficiency $\eta \approx 10^{-6}$. This is consistent with the lasing efficiency of approximately 1.7×10^{-6} estimated by comparing output versus pump fluence measured in Ref. [5]. The discrepancy between the thermodynamic limit critical

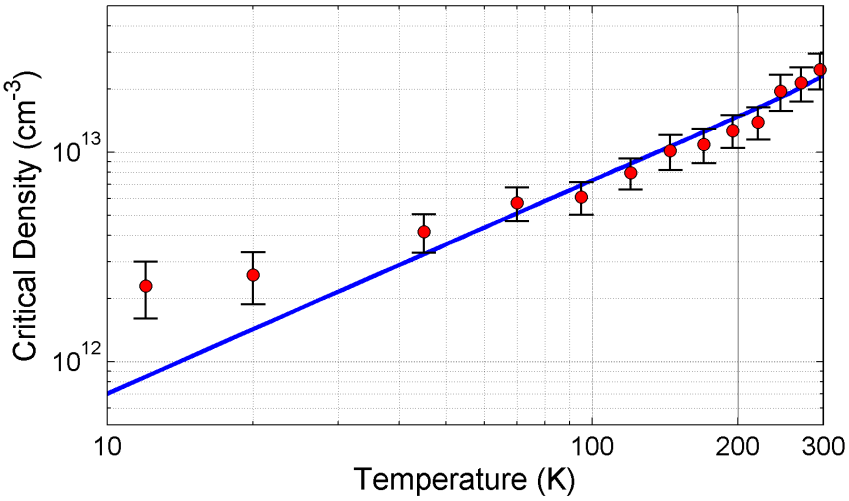

Figure 8.5: Estimated polariton population density at threshold (circles) assuming 50 % absorption of incident light and a polariton lasing quantum efficiency $\eta = 10^{-6}$. The solid line indicates the calculated critical density for condensation, N_c, in the thermodynamic limit. The low efficiency for Bose-Einstein condensation indicates considerable temperature-independent losses in the anthracene cavity. The theoretical 3D density in the cavity is calculated by dividing the 2D density by the cavity thickness.

density (which assumes infinite particle lifetime) and the pump fluence required for lasing most likely arises from a combination of loss pathways during the relaxation of excitons from the reservoir to the bottom of the polariton branch. The fluorescence quantum yield for crystalline anthracene has been reported to be 0.64, with structural defects and impurities diminishing this value even further [20]. Additionally, radiative coupling of reservoir excitons and polaritons to leaky DBR modes is expected to significantly compete with relaxation to the branch minimum. Furthermore, bimolecular interactions such as singlet-singlet and singlet-triplet quenching may become significant at high pumping intensities. However, as evident in Fig. 8.2 the polariton PL efficiency below threshold is unchanged at different temperatures, indicating that these processes are *not* strongly temperature dependent, and that η is fairly constant across the temperature range studied. Thus, the correspondence between the observed temperature dependence of the lasing threshold and that of the critical density for BEC does not

appear to be due to temperature dependent kinetic relaxation into the polariton ground state from the exciton reservoir.

8.5 Conclusion

In summary, a linear temperature dependence of the polariton lasing threshold on temperature in a crystalline organic Fabry-Pérot microcavity is measured. The trend is consistent with that of a finite 2D BEC critical density, and is in sharp contrast to the behavior of a conventional organic laser, pointing to the clear differences in physical origin of these two phenomena. By reducing the temperature from 300 K to 12 K, an order of magnitude reduction in the polariton lasing threshold is achieved. However, to take full advantage of the low thresholds possible in a polariton laser, significant radiative and non-radiative losses must be reduced. Due to these losses, the experimental density necessary for lasing is six orders higher than the thermodynamic limit, suggesting that materials other than anthracene are likely more advantageous for use in polariton lasers. Although several unresolved questions remain as to the effect of kinetic processes and particle interactions, as well as the exact mechanism of stimulated scattering above threshold, this treatment is nonetheless a useful step in exploring the connection between polariton lasing and Bose-Einstein condensation in a strongly-coupled anthracene microcavity.

CHAPTER VIII

Bibliography

[1] J. Kasprzak, M. Richard, S. Kundermann, A. Baas, et al., *Nature* **443**, 409 (2006).

[2] A. Imamoğlu, R. J. Ram, S. Pau, and Y. Yamamoto, *Phys. Rev. A* **53**, 4250 (1996).

[3] H. Deng, G. Weihs, D. Snoke, J. Bloch, and Y. Yamamoto, *P. Natl. Acad. Sci.* **100**, 15318 (2003).

[4] S. Christopoulos, G. B. H. von Högersthal, A. J. D. Grundy, P. G. Lagoudakis, et al., *Phys. Rev. Lett.* **98**, 126405 (2007).

[5] S. Kéna-Cohen and S. R. Forrest, *Nat. Photonics* **4**, 371 (2010).

[6] G. Malpuech, A. Kavokin, and F. P. Laussy, *Phys. Status. Solidi A* **195**, 568 (2003).

[7] J. Kasprzak, D. D. Solnyshkov, R. André, L. S. Dang, and G. Malpuech, *Phys. Rev. Lett.* **101**, 146404 (2008).

[8] E. Wertz, L. Ferrier, D. D. Solnyshkov, P. Senellart, et al., *Appl. Phys. Lett.* **95**, 051108 (2009).

[9] R. Butté, J. Levrat, G. Christmann, E. Feltin, J.-F. Carlin, and N. Grandjean, *Phys. Rev. B* **80**, 233301 (2009).

[10] J. Levrat, R. Butté, E. Feltin, J.-F. Carlin, et al., *Phys. Rev. B* **81**, 125305 (2010).

[11] H. Franke, C. Sturm, R. Schmidt-Grund, G. Wagner, and M. Grundmann, *New J. Phys.* **14**, 013037 (2012).

[12] V. G. Kozlov, V. Bulović, and S. R. Forrest, *Appl. Phys. Lett.* **71**, 2575 (1997).

[13] G. Ramos-Ortiz, C. Spiegelberg, N. Peyghambarian, and B. Kippelen, *Appl. Phys. Lett.* **77**, 2783 (2000).

[14] C. Kim, P. E. Burrows, and S. R. Forrest, *Science* **288**, 831 (2000).

[15] Y. Zhang and S. R. Forrest, *Phys. Rev. B* **84**, 241301 (2011).

[16] S. Kéna-Cohen, M. Davanço, and S. R. Forrest, *Phys. Rev. Lett.* **101**, 116401 (2008).

[17] R. Gupta, J. Park, V. Srdanov, and A. Heeger, *Synth. Met.* **132**, 105 (2002).

[18] D. M. Coles, P. Michetti, C. Clark, W. C. Tsoi, et al., *Adv. Func. Mater.* **21**, 3691 (2011).

[19] G. Malpuech, Y. G. Rubo, F. P. Laussy, P. Bigenwald, and A. V. Kavokin, *Semicond. Sci. Tech.* **18**, S395 (2003).

[20] R. Katoh, K. Suzuki, A. Furube, M. Kotani, and K. Tokumaru, *J. Phys. Chem. C* **113**, 2961 (2009).

CHAPTER IX

Room temperature Frenkel-Wannier-Mott hybridization of degenerate excitons in a strongly coupled microcavity

9.1 Introduction

For a number of years, combining organic and inorganic semiconductor systems has been of interest as a means to precisely engineer optoelectronic properties to meet the requirements of particular applications [1–3]. Hybrid structures using direct Coulomb coupling of tightly bound and stable organic Frenkel, and more delocalized and unstable (at room temperature) inorganic WM excitons have been sought to produce efficient non-radiative energy transfer, enhanced oscillator strength, and optical non-linearities [4–13]. Due to the limited range of the dipole-dipole interaction, however, a more convenient approach to hybridization of these dissimilar excited states is photon-mediated coupling in a microcavity [14]. In the limit of strong light-matter coupling (i.e. when the interaction strength exceeds the excitonic and cavity linewidths), formation of new quasiparticle eigenstates, known as polaritons, has been demonstrated by mixing multiple excitons with a cavity photon [15–19]. In the case of non-resonant excitons, the contribution of each component (and thus the excitonic hybridization) varies with angle [20]. Here, we demonstrate uniform Frenkel-Wannier-Mott hybridization of degenerate excitons in spatially separate nanoparticle ZnO and NTCDA layers within a strongly-coupled microcavity. Remarkably, these hybrid states are stable at room temperature, which differs from previous reports of organic/inorganic polaritons that were only observed

well below 300 K. Their stability and angle independence opens up new possibilities for the use of hybrid systems in practical optoelectronic and nonlinear optical applications.

In the strong-coupling regime, the new normal modes of the system possess both excitonic and photonic character. The intersecting energy-momentum dispersions of the uncoupled photon and exciton(s) split into anticrossing polariton branches. The number of branches is equal to the number of interacting photonic and excitonic states. The energy separation between the branches around each excitonic resonance, known as the Rabi splitting, is proportional to the strength of the light-matter interaction, which in turn depends on the oscillator strength of the materials. Due to conservation of the in-plane momentum associated with the photonic component of the polariton, the dispersion can be observed in angle-resolved reflectivity or (when present) photoluminescence with a one-to-one mapping between angle and polariton in-plane momentum. In general, the proportion of the photon and exciton contributions to the polariton varies along each branch. In previously reported hybrid organic/inorganic polariton systems [17–19], the Rabi splitting was smaller than the energy difference between Frenkel and WM excitons resulting in three branches, the middle branch consisting of both excitons and the photon. Thus, the ratio of the organic to the inorganic exciton contribution varied with angle for the hybrid middle polariton. A theoretical treatment of such resonant (but non-degenerate) hybrid systems was developed by Agranovich et al. in Ref. [20]. In this work, we focus on degenerate Frenkel and WM excitons that simultaneously couple to the cavity mode, thereby behaving as a single, angle-independent hybridized excitonic component of the resulting polaritons.

9.2 Cavity fabrication

Three microcavities, shown schematically in Fig. 9.1, were prepared for this study employing (a) inorganic semiconductor ZnO nanoparticles, (b) small-molecular weight organic NTCDA and (c) both as active materials. The bottom mirror, a DBR consisting of

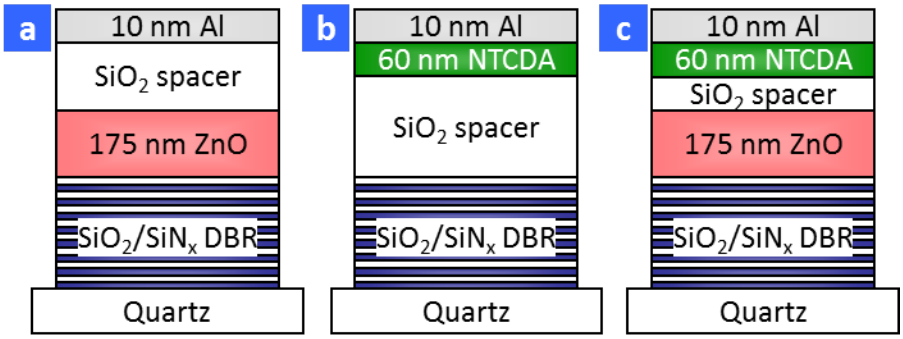

Figure 9.1: Structure of (a) ZnO, (b) NTCDA and (c) hybrid cavities. The thickness of the transparent SiO_2 spacer was adjusted to maintain similar overall detuning and electric field overlap with the active layers in the different cavities. The spacer also prevents direct transfer of excitons between the active layers in the hybrid cavity.

8.5 pairs of SiO_2/Si_3N_4, was deposited directly onto pre-cleaned quartz by PECVD. Optical constants were measured using variable-angle spectroscopic ellipsometry (VASE), and DBR layer thicknesses were adjusted to produce mirrors with a center wavelength around $\lambda = 380 - 390$ nm. Approximately 175-nm-thick ZnO films were spin-coated onto the DBR from a ZnO nanoparticle (< 35 nm average diameter) dispersion (Sigma-Aldrich SKU#721085) diluted by ethanol to ∼9.6% wt. The films were subsequently baked in air at 300 °C for 10 min to drive off the solvent. The SiO_2 spacer was deposited using an e-beam evaporator at a rate of 2–4 Å/s. The 60-nm-thick NTCDA films were deposited in high vacuum (base pressure $< 5 \times 10^{-7}$ Torr) by sublimation from a resistive source at 2 Å/s. The active layers were capped by a partially transparent, 10-nm-thick e-beam evaporated Al mirror at 1 Å/s. It was found that excessive heating of the substrate during top mirror deposition can cause NTCDA to crystalize and roughen destroying the mirror when the substrate temperature exceeded 70–90 °C and this prevented the use of a top DBR.

The optical constants of the spincoated ZnO nanoparticle film and NTCDA measured on Si by VASE and fit by a generalized oscillator model are shown in Fig. 9.2. NTCDA has two pronounced absorption peaks corresponding to the lowest-energy ex-

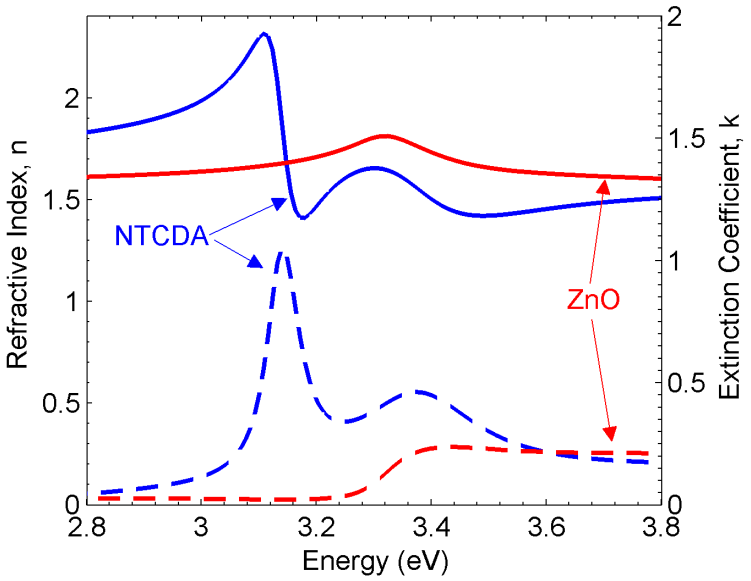

Figure 9.2: Refractive indices (solid) and extinction coefficients (dashed) of ZnO nanoparticle film and NTCDA on Si measured by ellipsometry. Two vibronic excitons are apparent for NTCDA at $E_{00} \approx 3.18\,\text{eV}$ and $E_{01} \approx 3.38\,\text{eV}$). The ZnO exciton is near the absorption band edge.

citon ($E_{00} \approx 3.18\,\text{eV}$) and its vibronic 0-1 exciton replica ($E_{01} \approx 3.38\,\text{eV}$). The higher-energy vibronic is approximately resonant with the ZnO exciton ($E_{ZnO} \approx E_{01}$) which is partly obscured by the band-edge absorption but is stable at room temperature due to its high binding energy of roughly 60 meV. For convenience, exciton energies will hence-forth be referred to as $E_1 = E_{00}$ and $E_2 = E_{01} = E_{ZnO}$ for the lower- and higher-energy excitons, respectively. Compared to reported values for bulk ZnO, the nanoparticle film has a slightly reduced refractive index and optical absorption, likely owing to reduced density of the spin-coated layer. Nonetheless, the film is optically homogeneous and, as can be seen in Fig. 9.2, has an absorption peak intensity roughly half that of the higher-energy exciton in NTCDA. To compensate for its lower oscillator strength, the cavity structure was designed such that two electric field antinodes are located in the ZnO layer and one in NTCDA. The thickness of the silica spacer was optimized for a negative detuning i.e. the energy of the photon mode at normal incidence, $E_0 \equiv E_{ph}(\theta = 0°)$, is

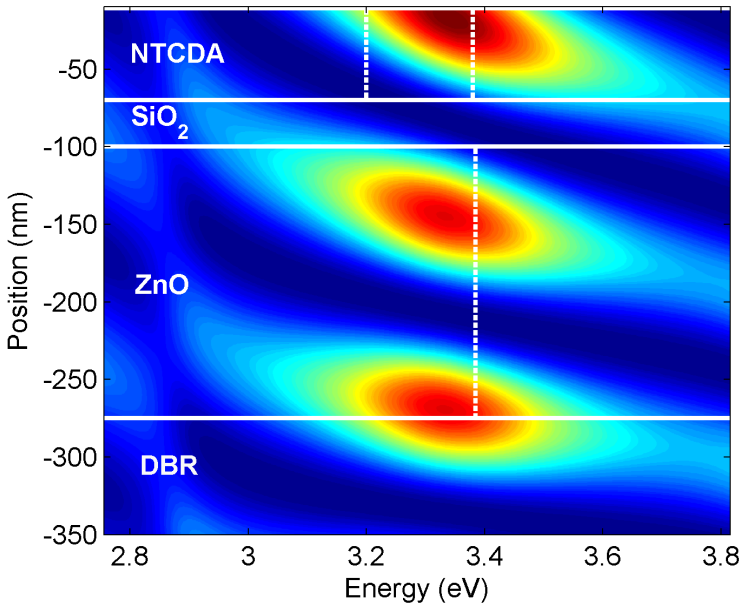

Figure 9.3: Optical field distribution in the hybrid optical microcavity simulated using the transfer matrix method at $\theta = 35°$ incidence. At this angle, the three field antinodes of the cavity mode are nearly resonant with the NTCDA 0-1 and ZnO excitons. Solid horizontal lines indicate layer boundaries, dashed vertical lines indicate approximate energetic position of the excitons. Note that although the 10-nm Al layer is too thin to see in the figure, it is included in the simulation.

below the higher-energy excitons ($E_0 < E_2$). The optical field intensity in the hybrid cavity is shown in Fig. 9.3 for $\theta = 35°$, approximately where the uncoupled cavity dispersion crosses E_2. In the ZnO-only and NTCDA-only cavities, the spacer thickness was increased to compensate for the optical length of the missing active layer, thereby maintaining comparable detunings and field distributions in all samples.

9.3 Angle-resolved reflectivity

To probe the energy-momentum dispersion of the cavities, angle- and spectrally-resolved cavity reflectivity was measured at room temperature from the Al side using TE-polarized light with 2.5 nm and 2.5° resolution (Fig. 9.4). Two reflectivity minima are observed above and below the uncoupled exciton energy in the ZnO cavity. The

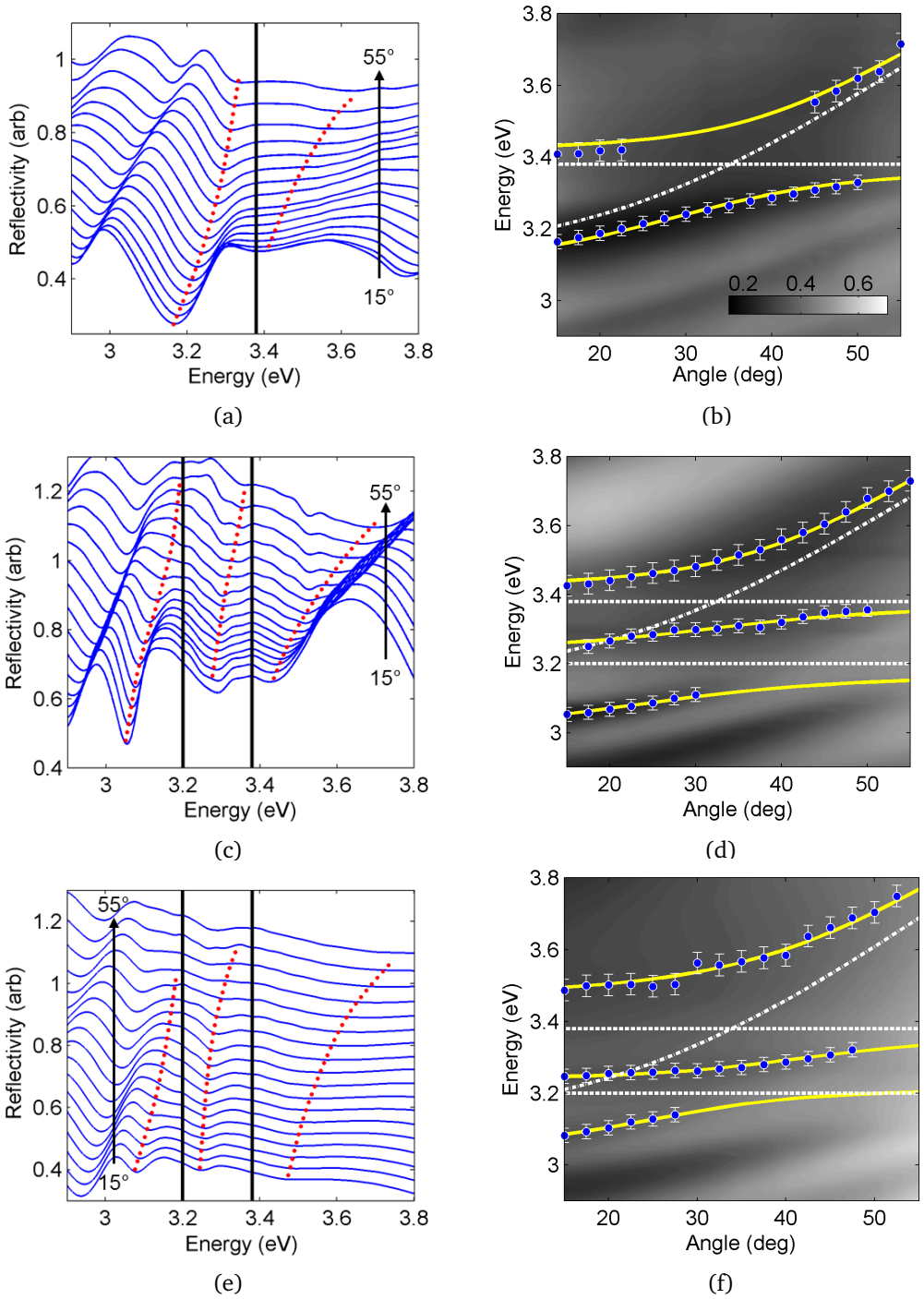

Figure 9.4: Room-temperature angle-resolved TE-polarized reflectivity of (a),(b) ZnO, (c),(d) NTCDA and (e),(f) hybrid cavities. On the left, exciton energy (vertical lines) and approximate reflectivity minima (dotted) are shown. Two minima are observed in the single-exciton ZnO cavity, three – in the NTCDA and hybrid cavities. On the right, the dispersion is extracted (circles) and fit (solid lines) using Eq. 9.1. Here, reflectivity (gradient), uncoupled excitons (dashed), and bare cavity dispersion (dash-dotted) are indicated for reference.

Table 9.1: Parameters of the Hamiltonian fit of the energy-momentum dispersion extracted from measured minima in angle-resolved reflectivity.

Cavity Structure	E_0(eV)	n_{eff}	V_1(meV)	V_2(meV)
175 nm ZnO/90 nm SiO_2	3.17 ± 0.01	1.65 ± 0.04		109 ± 4
115 nm SiO_2/60 nm NTCDA	3.15 ± 0.03	1.6 ± 0.08	111 ± 4	112 ± 11
ZnO/35 nmSiO_2/NTCDA	3.17 ± 0.02	1.6 ± 0.04	75 ± 8	161 ± 4

lower polariton is clearly resolved while the upper appears as a wide shallow dip due to the band absorption (see Fig. 9.2). Three minima are observed in both the NTCDA and hybrid cavities, suggesting that in both cases two oscillators are coupled to the photon. Again, in the hybrid case the highest energy polariton is difficult to resolve due to ZnO absorption, but is nonetheless apparent as a shoulder at low incidence angles, turning into a shallow and rather broad feature at higher angles.

The polariton dispersion extracted from the reflectivity minima can be fit by a coupled three-oscillator Hamiltonian [15, 20, 21] given by:

$$\begin{pmatrix} E_{ph} & V_1 & V_2 \\ V_1 & E_1 & 0 \\ V_2 & 0 & E_2 \end{pmatrix} \begin{pmatrix} \alpha \\ \beta \\ \gamma \end{pmatrix} = \varepsilon \begin{pmatrix} \alpha \\ \beta \\ \gamma \end{pmatrix}, \tag{9.1}$$

where E_{ph} is the cavity mode dispersion, V_1 and V_2 are interaction potentials between the photon and excitons, α^2, β^2 and γ^2 are the Hopfield mixing coefficients representing the fractional contribution of each component, and ε are angle-dependent polariton eigenenergies. For the ZnO cavity, V_1 and E_1 are omitted and the Hamiltonian is reduced to two coupled oscillators. The cavity dispersion is approximated by $E_{ph}(\theta) = E_0/\sqrt{1-\sin^2\theta/n_{eff}^2}$ where E_0 is the cavity cutoff energy as before, and n_{eff} is the effective refractive index of the cavity that takes into account field penetration into the bottom DBR and index differences between the active and spacer layers. The magnitude of the Rabi splitting is proportional to twice the interaction energy, i.e.

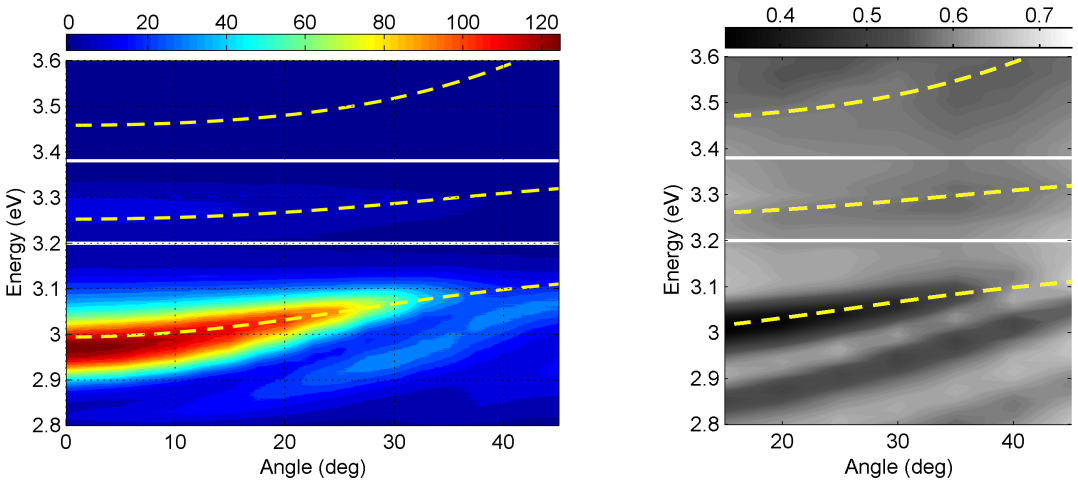

Figure 9.5: (a) Angle-resolved PL intensity of the hybrid cavity. The lower polariton branch is clearly observed due to fast relaxation via the NTCDA component. Weak uncoupled ZnO PL is also present around 3.26 eV. (b) Angle-resolved reflectivity from the same cavity. Lower and middle polaritons are easily distinguishable, while the upper branch is only seen at high angles. The reflectivity data is fit using Eq. 9.1 and the resulting dispersions (dashed lines) are plotted over both PL and reflectivity data for comparison. Solid lines indicate uncoupled exciton energies.

$\Omega_i = 2V_i$. Using V_i, E_0, n_{eff} as fitting parameters, we extract Rabi splittings of (322 ± 8), (224 ± 22) and (218 ± 8)meV between the upper two branches in the hybrid, NTCDA and ZnO cavities, respectively. The values of all parameters are listed in Table 9.1 and the resulting fits for the three cavities are shown in Fig. 9.4(b),(d),(f). The Rabi splitting around E_2 in the hybrid cavity significantly exceeds that of ZnO and NTCDA suggesting that both Frenkel excitons in the organic and Wannier-Mott excitons in the inorganic are strongly-coupled and jointly contribute to the E_2 oscillator strength.

9.4 Angle-resolved photoluminescence

Angle-resolved PL was measured for the hybrid cavity with the structure: quartz 12.5p SiO_2/Si_3N_4 DBR/ 95 nm ZnO/ 40 nm MgF_2/ 50 nm NTCDA/ 10 nm Al and is shown in Fig. 9.5(a). The sample was pumped non-resonantly using a pulsed N_2 laser

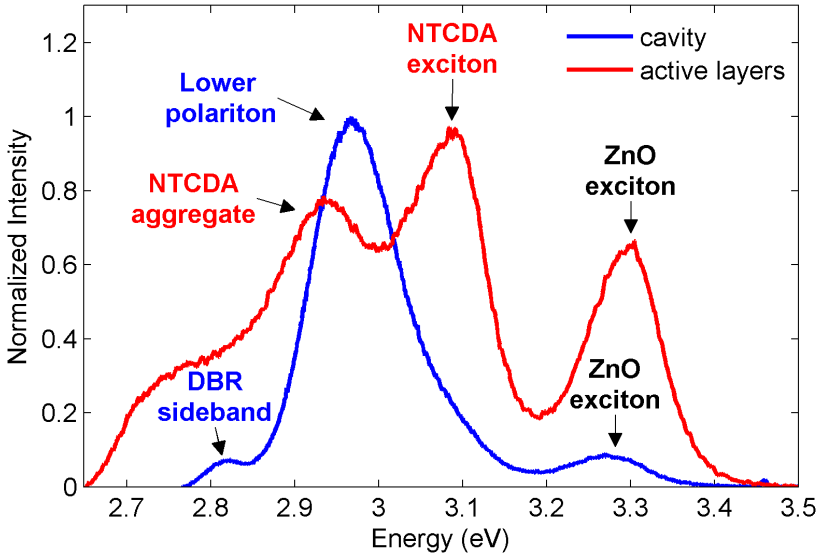

Figure 9.6: Comparison of cavity and active film PL. Without mirrors, relatively strong emission is observed from the ZnO exciton, NTCDA 0-0 exciton and NTCDA aggregates. The cavity PL is dominated by the lower polariton branch with only weak uncoupled emission from ZnO.

($\lambda = 337$ nm). The reflectivity of the same cavity (though not at the exact same spot) was measured for reference (Fig. 9.5(b)). The three polariton features observed in reflectivity were fit with Eq. 9.1, and the resulting dispersions are overlaid on both reflectivity and PL data. It is evident that aside from small differences related to variations across the sample, the dispersion is the same for the lower polariton branch. The middle and upper polaritons are not observed in PL for the hybrid (or pure NTCDA) cavities. Above the middle polariton branch energy, weak dispersionless PL is seen and is attributed to uncoupled ZnO exciton emission. Below the lower polariton, DBR sidebands can be clearly resolved in both emission at higher angles and reflection.

For comparison, PL from the active layers and spacer (95 nm ZnO/ 40 nm MgF_2/ 50 nm NTCDA) deposited onto quartz without mirrors was measured. As expected for excitonic emission, no spectral shift is observed as a function of angle. Figure 9.6 shows the emission of the active layers compared to that of the strong-coupled cavity at $\theta = 0°$. Since the spacer prevents direct transfer of excitons between ZnO and NTCDA, in the

absence of mirrors, strong emission is observed from both layers. For NTCDA, PL is mainly from the 0-0 exciton (due to Kasha's rule); below this peak, broad emission from aggregates is present. The ZnO peak intensity near 3.3 eV is roughly 70 % that of the NTCDA exciton. On the other hand, the cavity PL is dominated by the lower polariton, and only a small fraction of ZnO excitons is *not* strongly coupled to the photon mode. Given that there is no emission from the middle polariton (unlike in the case of a pure ZnO cavity), it is likely that the hybrid cavity opens an efficient nonradiative relaxation pathway from the ZnO reservoir to the lowest branch.

9.5 Discussion

The greatly enhanced interaction potential, V_2, in the hybrid cavity indicates stronger photon-exciton coupling compared to that in 'pure' cavities. This enhancement, in contrast to previous reports [15, 18, 19] on hybrid polaritons, can result from improved electric field overlap with the active layers, increased cavity quality and/or greater total oscillator strength. Since the detuning and overall optical length is kept roughly equal in all three cavities, the field distribution has only negligible variation. Likewise, because the structures all share the same mirrors, only minor differences in cavity quality are expected. Therefore, the hybrid cavity dispersion is consistent with increased oscillator strength of the E_2 exciton which in the present case is a hybrid excitonic state of Wannier-Mott and Frenkel exciton. The observed enhancement in the Rabi splitting of the hybrid cavity of (1.44 ± 0.15) compared to that of pure NTCDA cavity conclusively shows that indeed both the Frenkel excitons in NTCDA and Wannier-Mott excitons in ZnO simultaneously strongly couple to the photon mode, and together contribute to the strength of the E_2 transition.

In previous work, hybridization of two non-resonant excitons and a photon occurred predominantly in the middle polariton branch [15, 18, 19]. Since the excitonic fractions in the middle polariton must vary with wavevector [20] (as in Fig. 9.7), equal and

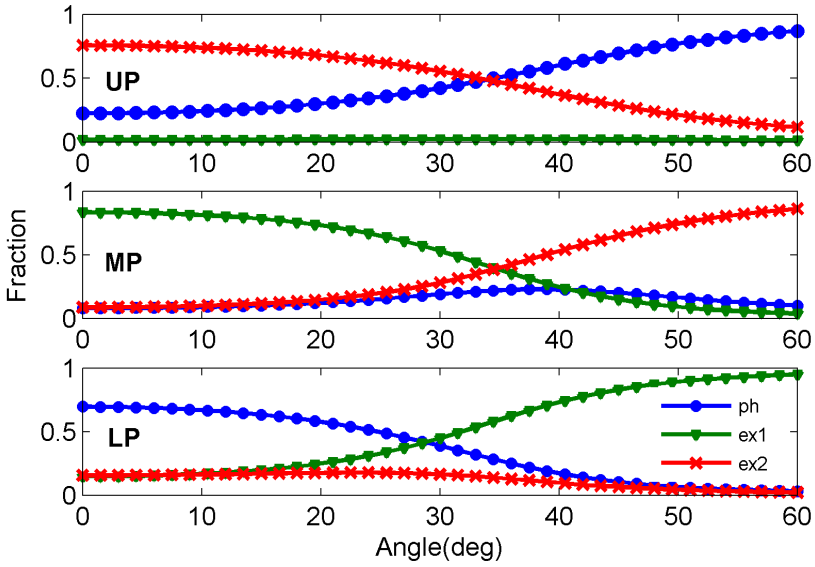

Figure 9.7: Hopfield coefficients showing the composition of the upper, middle, and lower polaritons in the hybrid cavity extracted from the Hamiltonian fit. The upper branch is composed largely of the uniformly hybridized (ZnO/NTCDA 0-1) exciton ('ex2,' crosses) and photon (circles). The lower branch is mostly NTCDA 0-0 exciton ('ex1,' triangles) mixed with the photon. The middle branch contains all three components.

maximum mixing of the excitons occurs at only a single incidence angle. Moreover, the photon contribution at this maximum is also significant. In the hybrid cavity reported here, the degenerate ZnO and NTCDA excitons are indistinguishably strongly-coupled at all angles, acting as a single hybrid exciton ('ex2' in Fig. 9.7) with the combined oscillator strengths of the two active layers. Therefore, the hybridization of NTCDA 0-1 and ZnO excitons is independent of the Hopfield mixing coefficients, instead resulting from the field overlap with the active layers which can be tailored by adjusting their thicknesses. Indeed, it is not possible to extract the individual contribution of the degenerate excitons using this formalism. The properties of the upper branch (which consists almost exclusively of the Frenkel-Wannier-Mott hybrid exciton mixed with the cavity photon) and the middle branch (which also adds the NTCDA 0-0 vibronic into the mix) are expected to be significantly different from either semiconductor. Unfortunately, the presence of the 0-0 exciton also means that upon excitation, the polariton population

quickly relaxes to the lower branch via emission of a molecular phonon. For this reason, no photoluminescence is observed from the middle or upper branches (see §9.4). The lower polariton photoluminescence generally follows the dispersion observed in reflectivity, but due to only minor contribution from the hybrid exciton yields little insight into the hybridization. A more convenient system would consist of an organic-inorganic microcavity where participation is limited to only degenerate excitons. Alternatively, a system with degeneracy between the hybrid polariton and the emission from the lowest molecular vibronic could be used to achieve fast population transfer to the bottom of the lower polariton branch, bypassing the bottleneck that often impedes polariton lasing in inorganic systems.

9.6 Conclusion

In summary, degenerate Frenkel and Wannier-Mott excitons are hybridized within an optical microcavity in the strong-coupling regime. The hybrid polariton states are stable at room temperature. A characteristic polariton dispersion and an increased Rabi splitting of (322 ± 8) eV is observed in angle-resolved reflectivity of a cavity containing NTCDA and ZnO as active materials confirming strong coupling of both species. The splitting is larger than that of comparably detuned cavities containing only NTCDA or ZnO, and suggests that the two semiconductors are acting as a single, uniformly-hybridized excitonic component of the resulting polariton eigenstate. The upper polariton consists of a mixture of the hybrid exciton and cavity photon, while for the middle polariton, these states are further hybridized with the non-degenerate NTCDA 0-0 exciton. In contrast to previous work, the Frenkel-Wannier-Mott hybridization does not vary as a function of in-plane momentum for the upper branch, and only varies in the middle branch due to the presence of a second non-resonant Frenkel state. Due to significant contributions from the hybrid exciton, both the upper and middle polariton branches are expected to have novel optical properties (e.g. pronounced third-order nonlinear optical

susceptibility [3]) that warrant further investigation. Although the population dynamics of the NTCDA/ZnO polariton system are dominated by fast relaxation to the lowest branch via emission of an intermolecular phonon in NTCDA, such hybrid degenerate systems nonetheless offer a promising pathway to nonlinear devices with engineered optical properties.

CHAPTER IX

Bibliography

[1] S. R. Forrest, M. L. Kaplan, P. H. Schmidt, W. L. Feldmann, and E. Yanowski, *Appl. Phys. Lett.* **41**, 90 (1982).

[2] N. Li, K. Lee, C. K. Renshaw, X. Xiao, and S. R. Forrest, *Appl. Phys. Lett.* **98**, 053504 (2011).

[3] V. M. Agranovich, Y. N. Gartstein, and M. Litinskaya, *Chem. Rev.* **111**, 5179 (2011).

[4] G. C. L. Rocca, F. Bassani, and V. M. Agranovich, *Il Nuovo Cimento D* **17**, 1555 (1995).

[5] A. Engelmann, V. I. Yudson, and P. Reineker, *Phys. Rev. B* **57**, 1784 (1998).

[6] Y. Gao, N. Q. Huong, J. L. Birman, and M. J. Potasek, *J. Appl. Phys.* **96**, 4839 (2004).

[7] S. Blumstengel, S. Sadofev, C. Xu, J. Puls, and F. Henneberger, *Phys. Rev. Lett.* **97**, 237401 (2006).

[8] G. Heliotis, G. Itskos, R. Murray, M. D. Dawson, I. M. Watson, and D. D. C. Bradley, *Adv. Mater.* **18**, 334 (2006).

[9] G. Itskos, G. Heliotis, P. G. Lagoudakis, J. Lupton, et al., *Phys. Rev. B* **76**, 035344 (2007).

[10] Q. Zhang, T. Atay, J. R. Tischler, M. S. Bradley, V. Bulović, and A. V. Nurmikko, *Nat. Nanotechnol.* **2**, 555 (2007).

[11] Y. Gao, A. Tonizzo, A. Walser, M. Potasek, and R. Dorsinville, *Appl. Phys. Lett.* **92**, 033106 (2008).

[12] K. Ema, M. Inomata, Y. Kato, H. Kunugita, and M. Era, *Phys. Rev. Lett.* **100**, 257401 (2008).

[13] N. Kawano, M. Koshimizu, and K. Asai, *J. Phys. Chem. C* **116**, 22992 (2012).

[14] H. Abassi, S. Jaziri, and R. Bennaceur, *Physica E* **7**, 686 (2000).

[15] R. J. Holmes and S. R. Forrest, *Phys. Rev. Lett.* **93**, 186404 (2004).

[16] D. Lidzey, J. Wenus, D. Whittaker, G. Itskos, et al., *J. Lumin.* **110**, 347 (2004).

[17] R. J. Holmes, S. Kéna-Cohen, V. M. Menon, and S. R. Forrest, *Phys. Rev. B* **74**, 235211 (2006).

[18] J. Wenus, R. Parashkov, S. Ceccarelli, A. Brehier, et al., *Phys. Rev. B* **74**, 235212 (2006).

[19] G. Lanty, S. Zhang, J. S. Lauret, E. Deleporte, et al., *Phys. Rev. B* **84**, 195449 (2011).

[20] V. Agranovich, H. Benisty, and C. Weisbuch, *Solid State Commun.* **102**, 631 (1997).

[21] J. Wainstain, C. Delalande, D. Gendt, M. Voos, et al., *Phys. Rev. B* **58**, 7269 (1998).

CHAPTER X

Conclusion and outlook

10.1 Prospects for OLEDs

In Part I, we pursued approaches to boosting OLED efficiency by extracting light trapped in the device. In addition to their impact on efficiency, outcoupling improvements can aid in tackling two other weaknesses of organic emitters, namely device lifetime and output intensity. Since both degradation and efficiency roll-off are worse at higher current densities, purely optical techniques which allow enhanced performance at equivalent or even reduced driving current can be hugely beneficial. As discussed in Chapter II, there are three primary sources of light-trapping: substrate modes due to TIR, waveguide modes in organics and ITO, and surface plasmons in the metal cathode. The focus in this thesis was the angle- and spectrally-independent outcoupling of the waveguide modes.

To this end, in Chapter III, we used numerical simulations to analyze and understand the dependence of light extraction by a dielectric grid embedded in the active layers. Guided by the modeling results, we demonstrated in Chapter IV that nearly threefold outcoupling enhancement is possible in an OLED with an embedded ultra-low-index grid made out of highly-porous silica. In addition, we studied waveguide-adjacent planar scattering structures in Chapters V and VI, finding that high degree of refractive index contrast and intimate contact between the waveguide core and the nearby scatterer are particularly essential to effective performance. Based on these findings, we developed two parallel approaches to fabricating planarized grids placed between the

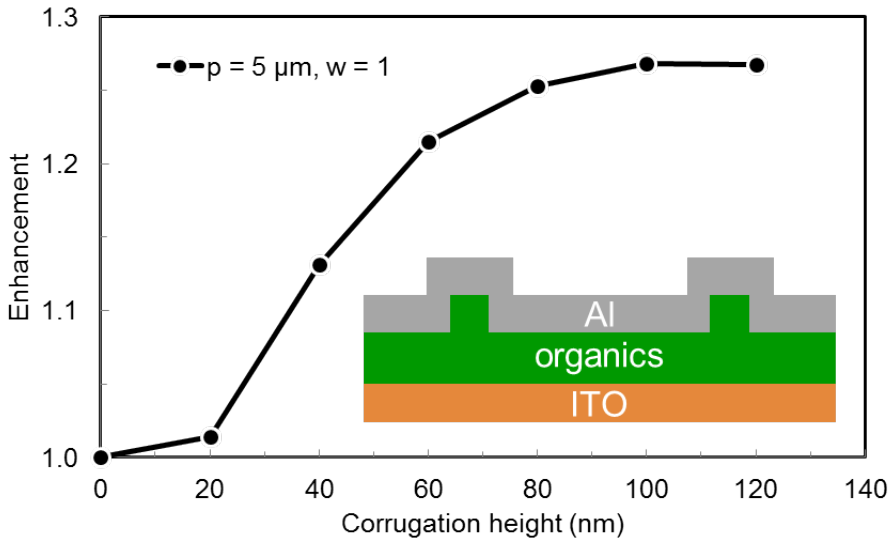

Figure 10.1: Simulated outcoupling enhancement as a function of metal corrugation height. As shown in the inset, the corrugation is formed around an index-matched grid with dimensions $w = 1\,\mu\text{m}$ and $p = 5\,\mu\text{m}$. All other layer thicknesses are 100 nm.

substrate and transparent anode of the device, and demonstrated preliminary device performance enhancement of nearly 2.5 times that of a conventional OLED (provided efficient substrate light extraction is also employed).

Given the typical distribution of power in the various layers of a bottom-emitting OLED (Fig. 2.5), these results approach the theoretical maximum outcoupling efficiency given full extraction of light confined in the substrate and waveguide regions. One open question is the contribution of the embedded LIG in Chapter IV to scattering of plasmon modes. In our simulations, we focused on refractive index contrast and neglected the considerable non-uniformity that is introduced by the dielectric grid. However, our experimental results suggest that the corrugation produced by depositing the organic and metal layers over the grid may play a significant role in outcoupling. Full-wave simulations of outcoupling with a corrugated electrode, but without any refractive index contrast, shown in Fig. 10.1, confirm that such structures scatter light analogously to the LIG. The exact interplay between the effects of the structured metal surface and refractive index contrast of an underlying grid is at this point not clear.

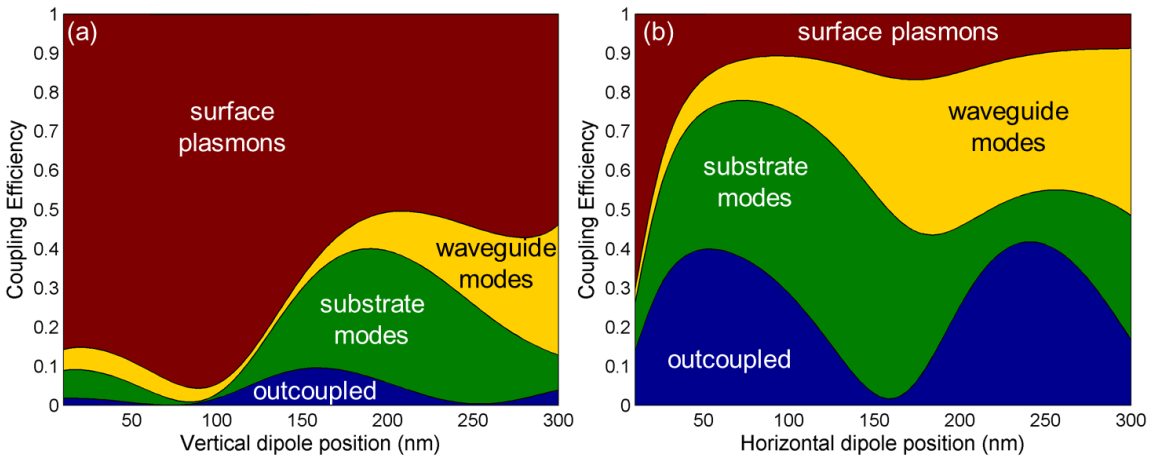

Figure 10.2: Coupling of emitted light to various modes as a function of emitter distance from the metal cathode in a 300 nm-thick organic layer for (a) a vertically and (b) horizontally oriented dipole.

Recently a new class of emitting materials with preferentially in-plane (horizontal) orientation of the dipole has been pursued as a means of enhancing OLED performance [1–3]. Since the vertical dipole emission is largely in the plane of the device and purely TM-polarized, its coupling to both waveguide and surface plasmon modes is much larger than for the horizontally oriented dipole (Fig. 10.2). Unlike OLEDs with isotropic emitter orientations, in these devices, the coupling to substrate and air is maximized when the EML is positioned near the cathode. For thicker or stacked devices, the light trapped in waveguide and plasmon modes makes up nearly half of the emitted power, but as can be seen in Fig. 10.2(b), the primary coupling is now to the waveguide rather than the metal. Thus, not only are outcoupling techniques such as the ones developed in this thesis still necessary, they should indeed be even more effective for oriented emitters positioned far from the cathode.

To date, only devices with partial in-plane dipole orientation have been produced through careful choice of guest-host systems. In order to achieve the full potential, deterministic control of the molecular emitter orientation needs to be developed through a combination of molecular engineering, device architecture and deposition techniques. Previously, preferential molecular orientation through the use of templating layers has

been demonstrated [4]. Using electromagnetic fields and directional deposition may be another means of controlling molecular orientation [5]. Finally, organic vapor-phase deposition with carrier gas flow directed along the plane of the substrate may prove advantageous. When combined with waveguide and substrate outcoupling, external quantum efficiencies approaching 90 % could be attained in oriented-dipole OLEDs, far surpassing any current device.

The application of outcoupling techniques presented in this dissertation to top-emitting OLEDs is another area of interest. Top-emitting devices are commercially important due to their straightforward integration with non-transparent transistor backplanes. In these devices, no substrate modes exist, but light confinement in waveguide modes is increased due to higher refractive index contrast between the active layers and air. Embedded grid structures should be effective at enhancing the performance by scattering analogous to the LIG. Moreover, the position of the metal cathode below the organic layers allows fabricating complex structures directly in the electrode prior to OLED fabrication, allowing scatter of both surface plasmons and waveguide modes. These techniques must be balanced against the need to have good conformal coverage of surface roughness or features.

One particular advantage of organic optoelectronics is the ability to produce devices on flexible substrates. In addition to the challenge of adapting light extraction methods to be compatible with bendable substrates, there remains an open question as to a suitable alternative to the rigid and brittle ITO anode. Several approaches to replicating ITO's high transparency while maintaining good electrical conductivity have been proposed including using highly conductive polymers [6], nanowire mesh [7], and thin metal films [8]. In particular, Wang et al. showed a remarkably high *EQE* of around 40 % for a flexible green device using a thin Au anode instead of ITO. Likely the enhancement is due to the suppression of waveguide modes by the weak metal-dielectric-metal waveguide. It remains to be seen whether this technique can be effectively realized for

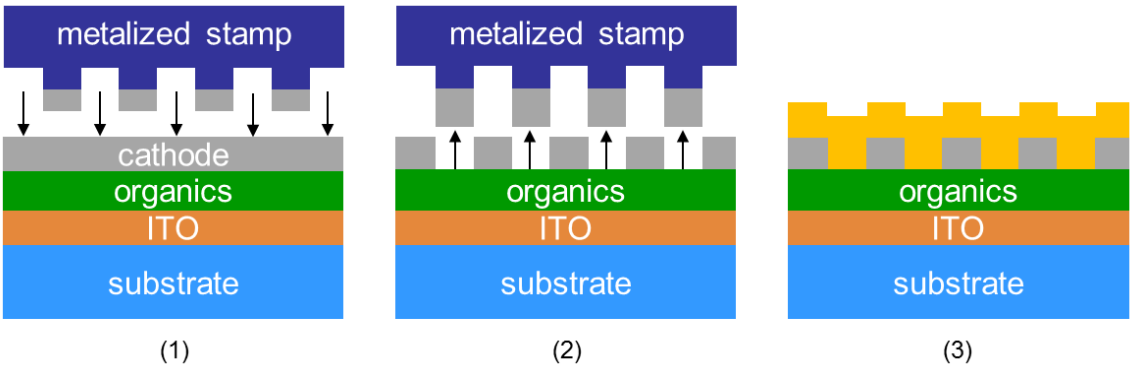

Figure 10.3: Schematic of patterning planar structures in the metal cathode by using nano-imprint liftoff. (1) A metalized patterned stamp is used to cold-weld to the metal film; (2) regions of the cathode are lifted off when the stamp is removed due to weak adhesion of metal to the underlying organic films; (3) the gaps are subsequently refilled using a different metal, conductive oxide, or dielectric while maintaining a smooth metal/organic interface.

broadband and angle-independent emission. Moreover, thin metal films are likely to have pronounced plasmonic resonances.

In many respects, the metal-dielectric interface is the final frontier of light extraction in OLEDs. Short of making fully metal-free devices [9], plasmonic losses can be reduced by creating diffractive gratings [10] or pseudo-random corrugated structures [11]. Bragg gratings are necessarily wavelength and angle-sensitive, and therefore, despite their efficiency, are not directly compatible with the constraints of both displays and solid-state lighting. On the other hand, as discussed in Chapter V, there is need for outcoupling methods that avoid introducing non-uniformity into the OLED. In Chapter VI, we explored large-period in-plane modification of the waveguide essentially in the cladding on the anode side. Similar approaches may be possible on the cathode side as well. By introducing in-plane optical non-uniformity in the cathode (e.g. by inserting regions of different metal or dielectric), one may be able to scatter light from surface plasmon or waveguide modes. This could be accomplished by lifting-off regions of the cathode using cold-welding to a metal-coated master stamp [12], followed by refilling with a second material as shown schematically in Fig. 10.3. The same technique could

also be used for creating pseudo-random high-contrast 2D photonic crystal lattices in the metal while maintaining a smooth cathode/organic interface.

10.2 Future of organic strong-coupling regime

In Chapter IX, we demonstrated photon-mediated uniform hybridization of excited states in organic and inorganic semiconductors. Due to the presence of a second organic resonance below the degenerate exciton energies, the population dynamics were dominated by relaxation out of the hybrid state. In order to study the hybrid state dynamics, it would be beneficial to create microcavities where only the lowest or single excitations of each material are hybridized.

A candidate system for such experiments is a cavity combining a large bandgap semiconductor like $Al_xGa_{1-x}N$ with the organic TDAF used recently for polariton lasing [13] and polariton electroluminescence [14]. At $x = 5\,\%$, AlGaN has a bandgap energy approximately equal to that of the Frenkel exciton in TDAF ($E_{AlGaN} \approx E_{TDAF} \approx 3.5\,\mathrm{eV}$) [15]. Alternatively, ZnO QWs could be used allowing the WM exciton energy to be conveniently tuned using the well width [16]. Detailed studies of emission under optical and electrical stimulation of such systems could be performed and are sure to reveal rich new physics in the interplay of the excited states. For example, Coles et al. have recently shown that long-range energy transfer between two simultaneously strong-coupled dyes is enhanced via the hybrid state [17]. This is a promising result for electrically stimulating one excitonic component of a hybrid system to achieve polariton lasing.

Another particular interest is the effect of new relaxation mechanisms available for the composite system (e.g. the enhanced polariton-polariton interaction due to the extended WM excitons or scattering with energetic intramolecular phonons in organics) on the population dynamics and the implications for reducing polariton lasing threshold. In anthracene, for example, it is likely that the low lasing efficiency is partly due to the lack of nonlinear interactions which compete with other decay pathways and

serve to thermalize the polariton population near the bottom of the branch. Parametric amplification (which has yet to be demonstrated in an organic system) may be possible in the hybrid microcavity given these nonlinearities. Furthermore, the combination of huge oscillator strength in TDAF with the low saturation density in the inorganic is also expected to enhance nonlinear two-photon absorption [18].

In our experiments, the strong-coupled cavities consisted of one or two DBRs; however, all metal cavities afford certain advantages and are worth investigating further. For one, there is no field penetration into the mirror or coupling to DBR sidebands; the optical mode is significantly more confined providing higher interaction with the active material [19]. Indeed, such cavities have been used to reach the ultra-strong-coupling regime where the Rabi splitting reaches a significant fraction of the uncoupled exciton resonance [14, 20, 21]. Additionally, metal mirrors can provide a broad stopband that can accommodate such large energy separation between the upper and lower polaritons. Finally, metal mirrors allow for straightforward electrical injection [14, 21, 22].

Finally, quite recently Akselrod et al. demonstrated a ten-fold reduction in lasing threshold in a conventional DCM:Alq_3 vertical microcavity laser when optically pumped by sub-picosecond pulses. The results were understood as an instance of Dicke superradiance – cooperative emission of a coherent ensemble of excitons [23]. The phase coherence evolves spontaneously due to the high population density generated by the ultrafast pump. In all organic polariton lasing demonstrations to date, the optical excitation was extremely short as well: $\sim$200 fs in Refs. [24, 25], 250 fs in Ref. [13], and $\sim$8 ps in Ref. [26]. The connection between polariton lasing, stimulated emission and superradiant seeding needs clarification. If indeed ultrafast stimulation is necessary to reach the lasing threshold in the strong-coupling regime, then achieving electrically excited organic polariton lasing may be a difficult prospect.

10.3 Conclusion

In conclusion, the work presented in this dissertation is of consequence for both practical applications of light generating devices, and for advancement of understanding of light interaction with organic semiconductors. Specifically, the advances in outcoupling described in the first part of this thesis allow significant efficiency improvements for OLED displays and lighting. The work regarding the strong-coupling regime described in the second part adds to the rather young field of organic polariton lasing and enables further investigations of hybrid organic-inorganic polaritonic devices. Overall, the field of organic optoelectronics continues to be rich in opportunity for both technological applications and fundamental research.

CHAPTER X

Bibliography

[1] M. Flämmich, J. Frischeisen, D. S. Setz, D. Michaelis, et al., *Org. Electron.* **12**, 1663 (2011).

[2] J. Frischeisen, D. Yokoyama, A. Endo, C. Adachi, and W. Brütting, *Org. Electron.* **12**, 809 (2011).

[3] C. Mayr, S. Y. Lee, T. D. Schmidt, T. Yasuda, C. Adachi, and W. Brfffdfffdtting, *Adv. Func. Mater.* **24**, 5232 (2014).

[4] B. E. Lassiter, R. R. Lunt, C. K. Renshaw, and S. R. Forrest, *Opt. Express* **18**, A444 (2010).

[5] B. Ayupov and S. Prokhorova, *Opt. Spectrosc.* **90**, 446 (2001).

[6] S.-I. Na, S.-S. Kim, J. Jo, and D.-Y. Kim, *Adv. Mater.* **20**, 4061 (2008).

[7] A. R. Madaria, A. Kumar, F. N. Ishikawa, and C. Zhou, *Nano Research* **3**, 564 (2010).

[8] Z. Wang, M. Helander, J. Qiu, D. Puzzo, et al., *Nat. Photonics* **5**, 753 (2011).

[9] J.-B. Kim, J.-H. Lee, C.-K. Moon, S.-Y. Kim, and J.-J. Kim, *Adv. Mater.* **25**, 3571 (2013).

[10] J. Frischeisen, Q. Niu, A. Abdellah, J. B. Kinzel, et al., *Opt. Express* **19**, A7 (2011).

[11] W. H. Koo, S. M. Jeong, F. Araoka, K. Ishikawa, et al., *Nat. Photonics* **4**, 222 (2010).

[12] X. Xu, M. Davanço, X. Qi, and S. R. Forrest, *Org. Electron.* **9**, 1122.

[13] K. Daskalakis, S. Maier, and R. M. and S. Kéna-Cohen, *Nat. Mater.* **13**, 271 (2014).

[14] C. R. Gubbin, S. A. Maier, and S. Kéna-Cohen, *Appl. Phys. Lett.* **104**, 233302 (2014).

[15] E. F. Schubert, *Light-Emitting Diodes* (Cambridge University Press, 2006), 431 pp.

[16] T. Makino, Y. Segawa, M. Kawasaki, and H. Koinuma, *Semicond. Sci. Tech.* **20**, S78 (2005).

[17] D. M. Coles, N. Somaschi, P. Michetti, C. Clark, et al., *Nat. Mater.* **13**, 712 (2014).

[18] V. M. Agranovich, Y. N. Gartstein, and M. Litinskaya, *Chem. Rev.* **111**, 5179 (2011).

[19] P. A. Hobson, W. L. Barnes, D. G. Lidzey, G. A. Gehring, et al., *Appl. Phys. Lett.* **81**, 3519 (2002).

[20] S. Kéna-Cohen, S. A. Maier, and D. D. C. Bradley, *Adv. Opt. Mater.* **1**, 827 (2013).

[21] M. Mazzeo, A. Genco, S. Gambino, D. Ballarini, et al., *Appl. Phys. Lett.* **104**, 233303 (2014).

[22] J. R. Tischler, M. S. Bradley, V. Bulović, J. H. Song, and A. Nurmikko, *Phys. Rev. Lett.* **95**, 036401 (2005).

[23] R. H. Dicke, *Phys. Rev.* **93**, 99 (1954).

[24] S. Kéna-Cohen and S. R. Forrest, *Nat. Photonics* **4**, 371 (2010).

[25] M. Slootsky, Y. Zhang, and S. R. Forrest, *Phys. Rev. B* **86**, 045312 (2012).

[26] J. D. Plumhof, T. Stöferle, L. Mai, and U. S. and R. F. Mahrt, *Nat. Mater.* **13**, 247 (2014).

APPENDIX

APPENDIX A

List of publications

Journal publications

M. Slootsky, X. Liu, V. M. Menon, and S. R. Forrest, "Room temperature Frenkel-Wannier-Mott hybridization of degenerate excitons in a strongly coupled microcavity," *Phys. Rev. Lett.* **112**, 076401 (2014).

Q. C. Burlingame, X. Tong, J. Hankett, P. Su, M. Slootsky, and S. R. Forrest, "Photochemical origins of burn-in degradation in small molecular weight organic photovoltaic cells," (2014), in preparation.

J. Lee, M. Slootsky, K. Lee, Y. Zhang, and S. R. Forrest, "An electrophosphorescent organic light emitting concentrator," *Light: Sci. Appl.* **3**, e181 (2014).

X. Tong, N. Wang, M. Slootsky, J. Yu, and S. R. Forrest, "Intrinsic burn-in efficiency loss of small-molecule organic photovoltaic cells due to exciton-induced trap formation," *Sol. Energ. Mat. Sol. C.* **118**, 116 (2013).

M. Slootsky, Y. Zhang, and S. R. Forrest, "Temperature dependence of polariton lasing in a crystalline anthracene microcavity," *Phys. Rev. B* **86**, 045312 (2012).

Y. Zhang, M. Slootsky, and S. R. Forrest, "Enhanced efficiency in high-brightness fluorescent organic light emitting diodes through triplet management," *Appl. Phys. Lett.* **99**, 223303 (2011).

M. Slootsky and S. R. Forrest, "Enhancing waveguided light extraction in organic LEDs using an ultra-low-index grid," *Opt. Lett.* **35**, 1052 (2010).

M. Slootsky and S. R. Forrest, "Full-wave simulation of enhanced outcoupling of organic light-emitting devices with an embedded low-index grid," *Appl. Phys. Lett.* **94**, 163302 (2009).

X. Qi, M. Slootsky, and S. Forrest, "Stacked white organic light emitting devices consisting of separate red, green, and blue elements," *Appl. Phys. Lett.* **93**, 193306 (2008).

Conference contributions

M. Slootsky, X. Liu, S. R. Forrest, and V. M. Menon, "Formation of hybrid polaritons in an organic-inorganic microcavity at room temperature," in CLEO (San Jose, CA, 2013).

X. Liu, M. Slootsky, S. R. Forrest, and V. M. Menon, "Enhancing optical nonlinearity through engineered exciton coupling in organic-inorganic nanocomposites," in CLEO (San Jose, CA, 2013).

M. Slootsky, Y. Zhang, and S. R. Forrest, "Temperature dependence of polariton lasing in a crystalline anthracene microcavity," in ICSCE-6 (Stanford, CA, 2012).

X. Tong, N. Wang, M. Slootsky, and S. R. Forrest, "Exciton-induced degradation of photocurrent in small-molecule organic solar cells," in APS March Meeting (Baltimore, MD, 2013).

Y. Zhang, M. Slootsky, and S. R. Forrest, "Triplet management in organic light emitting diodes and lasers," in CLEO (San Jose, CA, 2012).

M. Slootsky and S. R. Forrest, "Enhancing waveguided light extraction in organic light-emitting devices via an ultra-low-index grid fabricated by oblique deposition," in MRS Fall Meeting (Boston, MA, 2009).

M. Slootsky, Y. Sun, and S. R. Forrest, "Full-wave simulation of enhanced outcoupling of organic light emitting devices with an embedded low-index grid," in MRS Fall Meeting (Boston, MA, 2008).

X. Qi, M. Slootsky, and S. R. Forrest, "Stacked white organic light emitting devices consisting of separate red, green and blue subelements," in MRS Fall Meeting (Boston, MA, 2008).

Patents

S. R. Forrest, X. Qi, and M. Slootsky, "Stacked white OLED having separate red, green and blue sub-elements," U.S. pat. 8,766,291 (July 2014).

S. R. Forrest, M. Slootsky, and R. Lunt, "Concave-hemisphere-patterned organic top-light emitting device," U.S. pat. 8,633,497 (Jan. 2014).

S. R. Forrest and M. Slootsky, "OLED device with integrated reflector," U.S. pat. req. 20130200781 (Feb. 2013).

S. R. Forrest, C. K. Renshaw, and M. Slootsky, "Integrated solar collectors using epitaxial lift off and cold weld bonded semiconductor solar cells," U.S. pat. req. 20130037095 (July 2012).

S. R. Forrest, R. R. Lunt, and M. Slootsky, "Light trapping architecture for photovoltaic and photodector applications," U.S. pat. req. 20120261558 (May 2011).